Fluid-rock interaction and H_2S and CO_2 mineralization in geothermal systems: experiments and geochemical modeling

Jan Přikryl

Faculty of Earth Sciences
University of Iceland
2018

Fluid-rock interaction and H_2S and CO_2 mineralization in geothermal systems: experiments and geochemical modeling

Jan Přikryl

Dissertation submitted to the Faculty of Earth Sciences for a *Philosophiae Doctor* degree in Geology

Advisor
Dr. Andri Stefánsson
Institute of Earth Sciences, University of Iceland

PhD Committee
Dr. Sigurður R. Gíslason
Institute of Earth Sciences, University of Iceland

Dr. Bergur Sigfússon
Reykjavík Energy

Opponents
Dr. Alasdair Skelton
Department of Geological Sciences, Stockholm University

Dr. Orlando Vaselli
Department of Earth Sciences, University of Florence

Faculty of Earth Sciences
School of Engineering and Natural Sciences
University of Iceland
Reykjavik, 30th May 2018

Fluid-rock interaction and H_2S and CO_2 mineralization in geothermal systems: experiments and geochemical modeling
Dissertation submitted to the Faculty of Earth Sciences for a *Philosophiae Doctor* degree in Geology

Faculty of Earth Sciences
School of Engineering and Natural Sciences
University of Iceland
Askja, Sturlugata 7
101, Reykjavik
Iceland

Bibliographic information:
Jan Přikryl, 2018, *Fluid-rock interaction and H_2S and CO_2 mineralization in geothermal systems: experiments and geochemical modeling*, PhD dissertation, Faculty of Earth Sciences, University of Iceland.

ISBN 978-9935-9412-0-6

Printing: Háskolaprentun
Reykjavik, Iceland, May 2018

Abstract

Fluid-rock interaction is an important process in nature, and in many industrial fields. Fluid-rock interaction can be utilized to sequester industrial gases like CO_2 and H_2S in porous rocks of geothermal systems. The gases are re-injected, together with condensed steam or wastewater, or both into a geothermal reservoir where they dissolve the host rocks, releasing cations, and forming permanent mineralization of carbonates and sulfides. The rate of the reactions and reaction progress depends on many parameters including temperature, pH and the concentrations of injected solutes and gases. In addition, intensive mineralization may lead to changes in porosity of the porous rocks and influence the available surfaces for primary rock leaching.

In order to study these factors of fluid-rock interaction and mineralization of CO_2 and H_2S under geothermal conditions, a number of laboratory experiments and reaction calculations were conducted. Three scenarios were studied: (1) dissolution of primary minerals and glasses under flow-through conditions using solution chemistry and solid imaging; (2) incongruent alteration of mafic minerals in CO_2-rich solutions using solution chemistry, mineralogy and isotopes; (3) mineralization of CO_2 and H_2S under flow-through conditions using solution chemistry and mineralogy. In all cases, the work involved an experimental and a modeling part.

The first part of this thesis centers on the dissolution of crystalline and amorphous rocks at acidic pH and 25°C. Solution composition, particle surface area, and porosity were determined as a function of travel distance within the reactor and time, using in-situ X-ray computed tomography (XMT) and chemical analysis. In all cases the porosity and the specific surface area of grains were observed to increase. However, these changes were not uniformly distributed along the fluid flow path nor over time. These observations matched the predictions from reactive transport modeling. Some of the materials were observed to dissolve non-stoichiometrically; which is not commonly taken into account in reactive transport modeling. Based on the experimental and modeling results it is concluded that accurate prediction capabilities of modeling at continuum scale may be limited when calculating pore volume and material surface area changes with time and along flow.

The second part of this study was on the alteration of olivine in CO_2-rich solutions using solution chemistry, mineralogy and isotope systematics. Upon progressive olivine dissolution and carbonate mineral formation, the dissolved inorganic carbon concentrations were observed to decrease, followed by a pH increase and formation of secondary minerals like chrysotile and brucite. The reactions were further constrained by $\delta^{26}Mg$ systematics. The secondary minerals formed preferentially incorporated isotopically light Mg from the dissolving primary phase. The application of a geochemical model was able to reproduce the principal experimental trends in solution chemistry, mineralogy and isotope ratios, suggesting that kinetic modeling of water-rock interaction from mineral dissolution and precipitation rates can work for relatively simple systems.

The third part of the study was on the sequestration and mineralization of CO_2 and H_2S in geothermal systems. A series of flow-through experiments were conducted where CO_2 and H_2S-rich solutions were reacted with various types of rocks (basalt, dacite and rhyolite) and at various temperatures (100-250°C). Intensive H_2S and CO_2 mineralization into sulfides and carbonates was observed. The limiting factor of sulfide mineralization was observed to be the Fe leaching rates from the rocks. Uptake of other Fe-containing minerals like epidote also decreased the H_2S sequestration efficiency. Currently, the only geothermal reservoirs being considered for the re-injection and mineralization of CO_2 and H_2S are located in basalts in Iceland. Other rock types like dacitic and rhyolitic rocks were also found to be effective media for H_2S and CO_2 sequestration. Based on the measured sequestration rates, ~0.2-0.5 t of CO_2 and ~0.03-0.05 t of H_2S are sequestered annually per cubic meter, depending on reservoir lithology and surface area. This suggests that the re-injection of CO_2 and H_2S into geothermal reservoirs is a potential solution for making geothermal energy production close to zero greenhouse gas emission.

Útdráttur

Efnaskipti vatns og bergs eru mikilvæg ferli í náttúrunni, sem og í margs konar iðnaði. Slíkum efnahvörfum má beita til þess að binda útblástursgös frá iðnaði, svo sem CO_2 og H_2S, varanlega í holrými bergs í jarðhitakerfum. Gösin eru leyst í þéttivatni eða affallsvatni, eða blöndu beggja, og þeim dælt niður í jarðhitageymi, þar sem þau leysa upp bergið, losa katjónir, og steinrennast svo til frambúðar sem karbónöt og súlfíð. Hraði og framgangur hvarfanna er háður mörgum þáttum, svo sem hita, pH-gildi, og styrk uppleystra steinefna og gasa í niðurdælingarvökvanum. Mikil steinrenning getur auk þess breytt poruhluta bergs, svo og yfirborði því sem aðgengilegt er fyrir uppleysingu frumsteinda.

Til þess að rannsaka áhrif og eðli þessara þátta við aðstæður eins og þær sem ríkja í jarðhitakerfum voru tilraunir gerðar á rannsóknarstofu og framgangur efnahvarfa reiknaður. Rannsóknin var í þremur liðum: (1) leysing frumsteinda og glers við gegnumflæði vökva, og voru þá lausnir efnagreindar og föst efni myndgreind; (2) óhlutfallsbundin ummyndun frumstæðra steinda í CO_2-ríkum lausnum, og voru þá lausnir efnagreindar, steindir greindar til tegundar og magns, og samsætuhlutföll mæld; (3) steinrenning CO_2 og H_2S við gegnumflæði vökva, og voru þá lausnir efnagreindar og steindir greindar til tegundar og magns. Einn þáttur sérhvers liðar rannsóknarinnar var unninn með tilraunum á rannsóknarstofu en annar með hermireikningum.

Fyrsti hluti ritgerðar þessarar fjallar um leysingu kristallaðs og myndlauss bergs í súrri lausn við 25°C. Upplausnin var efnagreind, yfirborð agna mælt, og poruhluti ákvarðaður, allt sem fall af tíma og lengd rennslisleiðar í hvarfakút. Til þessa var beitt bæði hefðbundnum efnagreiningum og reikningum á röntgensneiðmyndum. Í ljós kom, að bæði poruhluti bergs og eðlisyfirborð korna jukust í öllum tilvikum, en aukningin dreifðist ekki jafnt, hvorki eftir flæðileiðinni né í tíma. Þessar athuganir koma heim við forsögn hermireikninga á efnahvörfum og -flutningi í vökvaflæði. Sum efnanna leystust ekki upp í réttum frumefnahlutföllum, en sjaldan er tekið tillit til þessa atriðis í hermireikningum efnahvarfa við gegnumflæði. Niðurstöður tilrauna og reikninga gefa til kynna, að gildi samfelldra hermilíkana til nákvæmrar forsagnar á breytingum á poruhluta og efnisyfirborði, sem falli af tíma og lengd rennslisleiðar, sé takmarkað.

Annar hluti þessarar rannsóknar beindist að ummyndun ólivíns í CO_2-ríkum lausnum, en í rannsókninni voru lausnir efnagreindar, steindir ákvarðaðar og samsætuhlutföll mæld. Eftir því sem leysingu ólivíns og myndun karbónatsteinda vatt fram, minnkaði styrkur ólífrænna kolefnissambanda í lausn, pH-gildi hækkaði, og þá mynduðust síðsteindir á borð við krýsótíl og brúsít. Efnahvörfin voru ákvörðuð enn frekar af δ^{26}Mg hlutfalli, en síðsteindirnar sem mynduðust tóku upp hlutfallslega mikið af hinum léttari magnesíumsamsætum sem leystust upp úr frumsteindunum. Helstu drættir í efnasamsetningu lausna, steindaskipan og samsætuhlutföllum komu fram í niðurstöðum jarðefnafræðilegra líkanreikninga. Þetta bendir til þess, að reikningar á tímaháðum líkönum af efnaskiptum vatns og bergs, sem byggjast á mældum hraðaföstum leysingar og útfellingar steinda, kunni að duga til að lýsa hinum einfaldari kerfum.

Þriðji hluti rannsóknarinnar sneri að bindingu og steinrenningu CO_2 og H_2S í jarðhitakerfum. Gerðar voru allmargar gegnumstreymistilraunir með lausnir af CO_2 og H_2S í miklum styrk, en lausnirnar voru látnar hvarfast við ýmsar bergtegundir, basalt, dasít og ríólít, við misháan hita (100-250°C). Reyndist CO_2 steinrenna í karbónöt en H_2S í súlfíð, og hvort tveggja í miklum mæli. Í ljós kom, að steinrenning brennisteins í súlfíð takmarkaðist af hraða leysingar járns úr bergi. Upptaka járns í aðrar steindir, svo sem epídót, dró einnig úr steinrenningu súlfíðs. Sem stendur er einu jarðhitageymana, sem til skoðunar eru fyrir niðurdælingu og steinrenningu CO_2 og H_2S, að finna á íslenskum basaltsvæðum. Aðrar bergtegundir, svo sem dasít og ríólít, reyndust einnig duga vel til að binda H_2S og CO_2. Miðað við mældu bindingarhraðana, bindast ~0.2-0.5 t af CO_2 og ~0.03-0.05 t af H_2S árlega á rúmmeter, háð berggerð og yfirborðflatarmáli jarðhitageymis.. Þetta bendir til þess, að dæling CO_2 og H_2S niður í jarðhitakerfi kunni að vera fær leið til að gera orkuvinnslu með jarðvarma kolefnishlutlausa.

Scientia Potestas Est.

Table of Contents

List of Appendices

Appendix I
(Paper I)

Přikryl, J., Jha, D., Stefánsson, A., Stipp, S. L. S., 2017. Mineral dissolution in porous media: An experimental and modeling study on kinetics, porosity and surface area evolution. *Applied Geochemistry*, *87*, 57-70. doi.org/10.1016/j.apgeochem.2017.05.004

Appendix II
(Paper II)

Přikryl, J., Marieni, C., Gudbrandsson, S., Aradóttir, E.S., Gunnarsson, I., Stefánsson, A., 2018. H_2S sequestration process and sustainability in geothermal systems. *Geothermics*, *71*, 156-166. https://doi.org/10.1016/j.geothermics.2017.09.010

Appendix III
(Manuscript III)

Marieni, C., Přikryl, J., Aradóttir, E.S., Gunnarsson, I., Stefánsson, A., 2018. Towards green energy: Co-mineralization of carbon and sulfur in geothermal reservoirs. (submitted to *International Journal of Greenhouse Gas Control*)

Appendix IV
(Manuscript IV)

Přikryl, J., Stefánsson, A., Pearce, C.R., 2018. Tracing olivine carbonation and serpentinization in CO_2-rich fluids via magnesium exchange and isotopic fractionation. (submitted to *Geochimica et Cosmochimica Acta*)

Appendix V
Přikryl, J. and Stefánsson, A., 2014. CO_2 mineralization by olivine at hydrothermal conditions. *Mineralogical Magazine, 78(6),* 1473-1478. doi: 10.1180/minmag.2014.078.6.14

Acknowledgement

First of all, I have to thank my wife Margrét Rán Kjærnested for her patience. The lab work took countless weekends, evenings, nights, holidays that I spent sampling, fixing reactors, trying to model the experiments and general trouble-shooting instead of spending time with her or family. She was my moral support in many bad times and it was not easy as only about half of the laboratory projects worked out at the end. I also have to thank my son, Kristian Mímir, for teaching me what is truly important in life and also my parents for being great support no matter what I was doing in my life.

Next, I would like to acknowledge Andri Stefánsson for supervising my doctoral studies. I also want to thank many others, who without their help this project would not have been possible: Jón Örn Bjarnason, for the great atmosphere in the office and answering my many questions concerning thermodynamics or Linux. Snorri Gudbrandsson, for showing me that the simplest experimental design is often the best, and other philosophical concepts. Chiara Marieni, for being Chiara Marieni. Diwaker Jha, for improving the quality of my tomography data and constantly pushing the limits on my sense of humor. Gissur Örlygsson, for helping me setup the most suitable method for my tomography measurements. Gylfi Sigurðsson, for fixing the electrical circuits on the heating units at anytime. Níels Óskarson, for tips to elegantly grind rocks, coat samples and use a scanning electron miscroscope. Juan Diego Rodríguez-Blanco, for assistance with the XRD measurements. Maria Bjørn, for assistance with the BET measurements. Nicole Keller, for ordering anything I needed for the lab at anytime. Eydís Salome Eiríksdóttir, and Iwona Monika Galeczka, for the best 24/7 support with the ion chromatography systems. Petr Přikryl, for transferring my PhreeqC code to C++. Bergur Sigfússon, for discussing my PhreeqC code. Barbara Kleine, for debating isotope modeling. Eric H. Oelkers, for discussing Mg isotope systematics. Christopher Pearce, for running isotope samples. Birgir Jóhannesson, for his detailed introduction to scanning electron microscopy. Milan Novák, for teaching me a positive attitude and about how science works. Lukáš Zahradníček, for finding inspiration. Prathap Moola, Hanna Kaasalainen, Sunna Ólafsdóttir Wallevik, Deirdre Clark, Becca Neely, Giulia Sgattoni, Matylda Heřmanská, Sandra Ósk Snæbjörnsdóttir, Léa Lévy, Jacky Mallett and many others for nice company and their encouragement to keep going.

My studies were possible thanks to Marie-Curie PhD scholarship funded from European Union, Landsvirkjun research grant in geothermal energy, travel grants from University of Iceland and GEORG Geothermal Research Group. I was pleasured to regularly meet people involved in MINSC and CO_2 React, EU Initial Training Networks and create new strong bonds. I had the privilege to work or collaborate with some of the colleges at University of Copenhagen and Reykjavík Energy. Equally helpful were weekend "meetings" after meetings or conferences with this great group of the fellows. And last but not least, thanks to friends involved in floorball university sessions, rescue team and to yoga for helping me to stay sane.

1 Introduction

1.1 Fluid-rock interaction

Fluid interaction with the surrounding rocks is one of the fundamental processes occurring in the geosphere and hydrosphere. Fluid-rock interaction is, amongst other things, responsible for shaping various landscapes, is a part of chemical weathering and the formation of soils and plays a key role in the formation of ore deposits and geothermal alteration.

The alteration of rocks by fluid-rock interaction involves the dissolution of primary minerals or glasses and the formation of secondary minerals. In a closed system of fixed composition, the overall reaction is incongruent and affected by factors like temperature, rock and fluid composition, and the extent of the reaction or its reaction time. Moreover, for systems containing more than one phase, the extent of the reaction will further result in changes in mass between the various phases and changes in fluid composition (e.g. Gysi and Stefánsson, 2012a; 2012b; Johnson et al., 2014).

The rate and mechanism of rock alteration depends on the kinetics of the mineral dissolution and formation (precipitation and crystal growth), which in turn is influenced by factors like mineral surface areas (e.g., Gouze et al., 2003; Noiriel et al., 2009; 2012; Pokrovsky and Schott, 2000; Oelkers and Gíslason, 2001), properties of the mineral-solution interface (e.g., Hövelmann et al., 2011; Brown and Calas, 2012; Putnis, 2014), solution composition (e.g., Saldi et al., 2009; 2013) and temperature (e.g., Pearce et al. 2012; Gíslason and Oelkers 2003). The rate and mechanism of reactions can further be altered by various catalysts/inhibitors (e.g., Pokrovsky and Schott, 1999; Techer et al., 2001; Nielsen et al., 2016). Fluid-rock interaction results in changes in rock porosity and permeability with time, which in turn influences fluid flow and elemental transport (e.g., Steefel and Maher, 2009; Luquout and Gouze, 2009; Gouze and Luquot, 2011; Noiriel et al., 2015). All systems have a tendency to approach the most stable thermodynamic state, and the rate of these changes is controlled by kinetics (e.g., Aagaard and Helgeson, 1982; Helgeson et al., 1984; Marini, 2006; Schott et al., 2009). The above described relations may change considerably with the extent of the reaction.

Fluid-rock interaction is associated with geothermal systems, where the thermal fluid and steam react with the surrounding host rocks and secondary mineral forms (Figures 1.1 and 1.2). The type of geothermal secondary minerals formed depend mainly on temperature but fluid and rock composition also matter. The alteration minerals typically follow a temperature-related distribution with calcite, sulfides and sulfates, zeolites, various clays and oxides and hydroxides present at low temperature (<150°C) whereas oxides, feldspars, epidote, chlorite, amphiboles and garnets are common at higher temperatures (>200°C) (e.g., Tómasson and Kristmannsdóttir, 1972; Kristmannsdóttir, 1976; Browne, 1978; Gunnlaugsson and Arnórsson, 1982). The fluids interacting with the primary rocks and forming the secondary minerals are typically of meteoric or seawater origin. Reservoir fluids have typically mildly acid to neutral pH and Na, Cl, SO_4 and Si as the dominant dissolved solids with CO_2, H_2S and H_2 being the most important gases (e.g., Arnórsson et

al., 2006). The major element composition is characteristically controlled by close approach to equilibria with secondary minerals, except for elements like Cl and B that are essentially incompatible (e.g., Giggenbach 1980, 1981; Arnórsson et al., 1983).

Figure. 1.1*. Product of fluid-rock interaction, silica scaling, is taking place in a geothermal hot pool when silica concentration exceeds the solubility value and is supersaturated, Geysir geothermal area, Iceland.*

Figure 1.2. *Hikers observing a spectacular natural playground; interaction of water, rhyolitic rock, geothermal fluid and steam at Kerlingarfjöll mountain range, Iceland.*

Hydrogen sulfide (H_2S) and carbon dioxide (CO_2) are among the major components in geothermal fluids, with concentrations ranging from a few ppb to hundreds of ppm (e.g.,

Stefánsson, 2017). Hydrogen sulfide and CO_2 are volatile elements that are often emitted into the atmosphere from geothermal power plants, causing potential environmental problems (e.g., Arnórsson, 2004). Several methods have been used to reduce H_2S emissions including oxidation to form elemental sulfur or sulfuric acid (Sanopoulos and Karabelas, 1997); however CO_2 emissions from geothermal power plants are less commonly controlled. Reykjavík Energy is currently running a pilot project where CO_2 and H_2S is re-injected into the geothermal system where it is predicted that the gases mineralize into carbonates and sulfides. Previous work on volatile gas disposal has mainly focused on reaction modeling and experiments regarding CO_2 (e.g. Xu et al., 2003; Zerai et al., 2006; McPherson and Lichtner, 2001; Knauss et al., 2005; Palandri and Kharaka, 2005; Gaus et al., 2008; Gysi and Stefánsson, 2012b). However, less is known about H_2S disposal, and mixed CO_2 and H_2S sequestration under geothermal conditions. There are considerable geochemical uncertainties related to the injection and sequestration of H_2S and mixtures of CO_2 and H_2S, including the effects of injection on the fluid-rock interaction, rate and mechanism of H_2S and CO_2 mineralization, long term sustainability of such injection within the geothermal system, the effects of porosity and permeability associated with the sulfide and carbonate mineralization, and methods to assess the quantity of gas sequestration.

1.2 Aim and philosophy of the present work

The goal of this work was to study various aspects of fluid-rock interaction including: (1) dissolution of primary rock and changes in rock porosity and mineral surface areas; (2) tracing progressive fluid-rock interaction using solution chemistry, mineralogy and isotope systematics; (3) assessing the mechanism, rate and the effects of rock porosity related to H_2S and CO_2 mineralization under geothermal conditions, and long term sustainability of H_2S and CO_2 sequestration in geothermal systems. These processes and thematic questions were addressed using two methods, laboratory fluid-rock interaction experiments and reactive transport modeling. In addition, by combining the two, the aim was to evaluate the reliability of reaction and reactive transport.

The first question of interest that was addressed was: can bulk mineral dissolution and precipitation kinetic rates be applied to accurately predict mineral and solution chemistry, mass changes and variations in rock porosity as a function of time in a flow-through or an open system? The simplest case was tested, when various primary phases were dissolved in a flow-through reactor as a function of time, and the solution chemistry and in-situ rock properties measured as a function of time. Reaction front consisting of dissolution pattern, distribution of surface area, porosity and reactivity of various material were explored as a function of time and distance into the reaction column. The reactive transport modeling was designed as full-kinetic simulation and the results compared with experimental observations.

The second question was aimed at examining if kinetic reaction path modeling of a closed system is capable of accurately predicting incongruent fluid-rock interaction. Here, the interaction that involves fluid, CO_2 and forsterite was studied, a relatively simple chemical system to minimize problems associated with multicomponent systems. Batch type experiments were conducted, the solution chemistry, isotope systematics and mineralogy studied as a function of extent of reaction or reaction time and the trends simulated using kinetic reaction path modeling. The modeling included solution chemistry, mineralogy and magnesium isotope systematics.

The final question addressed the mechanisms, rate and long-term sustainability of H_2S and CO_2 sequestration into geothermal systems. Similar methods were applied as before, flow-through experiments and reactive transport modeling. Several rock types were tested ranging in mafic to silicic composition. Selected geochemical scenarios were further tested at field scales, and for long time injection and sequestration in geothermal systems, to assess the feasibility and sustainability of H_2S and CO_2 sequestration into geothermal systems in various geological environments.

1.3 Methods

Material preparation, experimental design, analyses of experimental solutions and solids, reaction path, transport and isotope geochemical modeling methodology are described in detail in the following Appendices (I-IV). This chapter is a brief summary of the experimental setups and the geochemical modeling, in order to provide an overview.

Photographs of the experimental apparatuses are shown in Figure 1.3. In total, three different experimental setups were used. The first setup used flow-through column reactors for dissolution experiments of rocks at low temperatures and pressures. The reactors were made of Teflon, 112 mm long and 5 mm in diameter with an internal volume of ~8800 mm^3. The height/diameter ratio of 22.4 maintains laminar and steady one dimensional (1D) flow in the system. The second setup involved Inconel flow-through reactors for experiments at elevated pressures and temperatures. The reactors were 300 mm long and had an internal diameter of 5.5 mm. This results in a similar height/diameter ratio (27.3) to the Teflon reactors. Temperature is maintained using an aluminum heating mantle and a temperature controlling unit. Both flow-through reactor designs were custom built. The third setup involved a modified Parr stirred reactor with volumes of 600 cm^3. All wetted parts of the reactor were made of inert titanium.

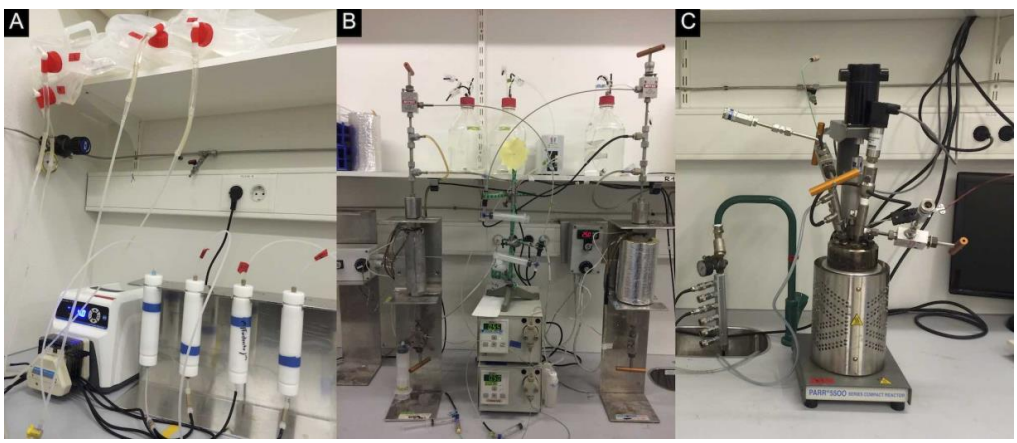

Figure 1.3. *Experimental design of A) flow-through reactors for low temperature and pressure; B) flow-through setups for elevated temperature, pressure conditions and C) batch stirred reactor for high temperature and pressure runs.*

Aqueous speciation, mineral saturation indices and reaction path and reactive transport simulations were carried out using the PhreeqC geochemical program (Parkhurst and Appelo, 2013). The PhreeqcRM reaction module for transport models was used for field-scale reactive transport simulations, with parallel processing implemented in C++ using the MPI multiprocessing library (Parkhust and Wissmeier, 2015). Larger scale simulations were calculated by computer cluster Garpur, a joint project of the University of Iceland and the University of Reykjavík. All modeling presented here was designed at continuum scale, meaning not every single grain, its morphology, surface nor space relation is considered, but instead is accounted as a summary and approximation of all associated parameters. Those simplifications are essential when reflecting composite systems of for example

millions of grains, forming a porous medium in the presented experiments. The kinetic rate (r) of mineral dissolution (+) and precipitation (-) was considered with generally employed transition state theory (Lasaga, 1998). One dimensional transport calculations for open systems can be imagined by dividing the reactor into several reactive cells to track reaction progress as a function of column distance (Fig. 1.4.), with total transport calculation steps per cell depending on the initial pore volume and corresponding solutions refilling rate. This also defined as the time step of transport in each cell. One dimensional advective-dispersive and reactive transport of solution was computed with forward flow direction to the cell with higher number to mimic experimental behavior (Appelo and Postma, 2005). Dispersivity (with 10% of travelled distance) in each cell was fixed for the total length of cell and no diffusion was defined.

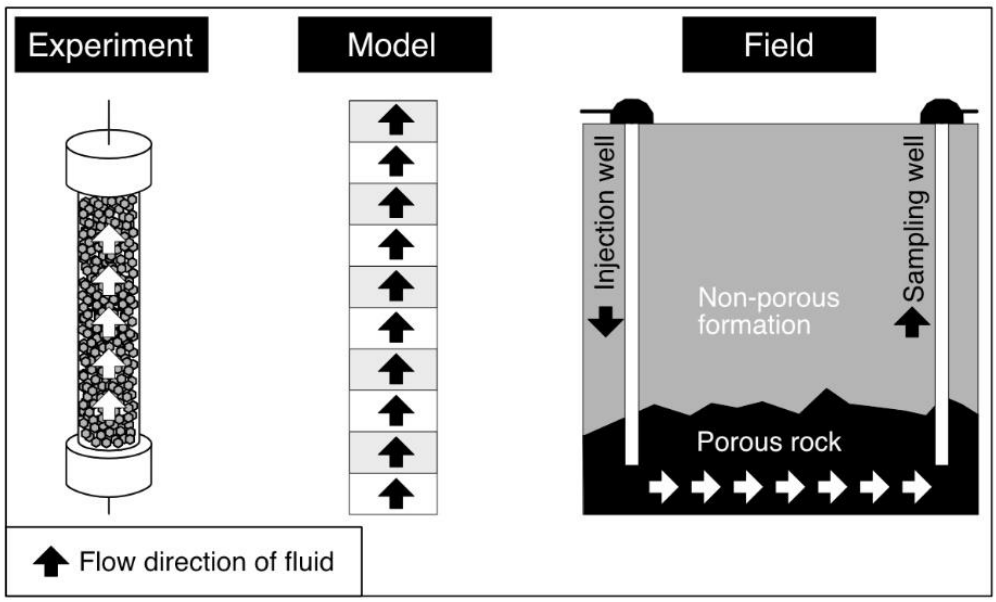

Figure 1.4. *Conceptual drawing of reactive transport simulation compared to experimental reactor and field situation. The reactor is divided into independent calculation cells with incremental reactions where potential geochemical processes take place in each cell.*

2 Summary

The research conducted in this dissertation thesis consists of four original research articles, prepared for publication or already published in peer-reviewed international journals. Paper I, II were published in *Applied Geochemistry* and *Geothermics*, respectively. Both papers are reprinted with permission from Elsevier. Manuscript III and IV are submitted to *International Journal of Greenhouse Gas Control* and to *Geochimica et Cosmochimica Acta*, respectively.

Paper I (Appendix I)

Přikryl, J., Jha, D., Stefánsson, A., Stipp, S. L. S., 2017. Mineral dissolution in porous media: An experimental and modeling study on kinetics, porosity and surface area evolution. *Applied Geochemistry, 81-86*, 1-14. doi.org/10.1016/j.apgeochem.2017.05.004

The paper describes the mineral and rock dissolution behavior of various rock types (basaltic glass, crystalline basalt and forsterite) in acidic solution (pH ~2.1-2.9, 8.1-8.7 mmol/kg HCl) at 25°C. Concentrations of the dissolved elements for crystalline basalt and forsterite reached a steady-state after ~10-15 days whereas basaltic glass retained almost the same concentrations after a month from the start. The reaction stoichiometry was studied by comparing elemental ratios in outlet solutions with ratios in the fresh minerals and rocks. In the case of basaltic glass and crystalline, the elemental mole ratios suggest non-stoichiometric dissolution under acidic conditions whereas forsterite dissolved stoichiometrically.

Two distinctive dissolution features were observed in the surface of the materials. Firstly, as time elapsed the dissolution became more apparent. This was the case for all the experiments. Secondly, the dissolution was observed to be unevenly distributed within the column. More intense dissolution features on the grains were observed in the inlet part of the reaction column than at the outlet part, including deep etch pits and troughs. These trends are considered to have been caused by mineral dissolution at the inlet side of reactors where fresh solution encounters the solid surfaces, followed by a slight increase in pH and corresponding slower dissolution with increasing reactor's distance. This is consistent with grain-size distribution showing solids to decrease with increasing experimental duration and the size of grains increasing from the inlet towards the outlet of the flow-through reactors.

Mineral and glass surface areas and porosities were observed to increase with experimental duration. These changes were minor for crystalline basalts and forsterite but significant for basaltic glass. Moreover, the variations in porosity were not uniformly distributed, they were greater on the inlet side than the outlet side. These observations demonstrate that dissolution of minerals and glasses resulted in progressive changes in solid grain size, that lead to changes in surface area and pore volume. Comparison of the experimental results with reactive transport modeling show that dissolution rates far from equilibrium obtained in this study using a complex flow-through system are comparable to those obtained from

mixed flow reactor experiments, where transport along the dissolving material does not occur. Some of the minerals and rocks were not observed to dissolve stoichiometrically, such non-stoichiometric dissolution is not commonly taken into account in reactive transport modeling. Similar results were obtained independently of the method applied for the calculations of mineral surface areas, i.e. whether geometric or tomographic normalized surface area was used or whether the simple spherical model or more complicated sugar lump model was implemented. Experimental mineral and rock dissolution of porous media resulted in increased porosity and specific surface area of the solids. Similar trends were predicted by reactive transport modeling. However, accurate values were difficult to predict. It follows that accurate prediction of the capabilities of simple reactive transport modeling may be limited for calculating pore volume and mineral and rock surface area changes with time and along flow paths that in turn are key parameters in determining dissolution rates, overall chemical mass movement in the system, and solution flow paths and velocities.

Paper II (Appendix II)

Přikryl, J., Marieni, C., Gudbrandsson, S., Aradóttir, E.S., Gunnarsson, I., Stefánsson, A., 2017. H_2S sequestration process and sustainability in geothermal systems. *Geothermics, 71*, 156-166. https://doi.org/10.1016/j.geothermics.2017.09.010

This manuscript is dedicated to the basalt alteration in hydrogen sulfide (H_2S) of rich solutions at 100-250°C, using an experimental and modeling approach. The conditions were selected to imitate the H_2S-injection conditions associated with the Sulfix project taking place at Hellisheiði power plant (SW Iceland).

The experimental outlet solution pH had in all cases neutral to mildly alkaline pH values: 6.6-7.3 at 100 °C, 7.7-8.2 at 200 °C, 6.0-9.4 at 240 °C and 8.9-9.7 at 250 °C. The solution concentration of elements showed narrow variation with time at given temperature. The outlet solution showed non-stoichiometric concentration with respect to basaltic glass in all samples. The H_2S concentrations rapidly attained an approximately constant value at each temperature, independently from the initial H_2S concentration in solution. The inlet side of the system had the biggest mass of precipitated secondary phases, decreasing with distance from the reactor inlet. Among the sulfur containing secondary minerals, pyrrhotite formed exclusively at 200 °C, whereas pyrite at 100, 240 and 250 °C. Saturation of sulfides in the solution at 200, 240 and 250 °C caused precipitation of many euhedral crystals of pyrite and pyrrhotite. However, minor pyrite with prevailing secondary iron oxides was observed at 100°C. Other phases observed were clay minerals at 100 °C, prehnite at 200 °C, and the solid solution of clinozoisite-epidote at 250 °C. Crystals, up to 5 μm, of subhedral clinozoisite formed predominantly in the upper parts of the reactor compared to sulfides.

The decrease in H_2S between the inlet and outlet solution, together with the observed formation of sulfide minerals like pyrite and pyrrhotite, indicate that H_2S mineralization occurred with a fluid-rock reaction of H_2S-rich solutions and basaltic rocks under geothermal conditions. The process of mineralization of H_2S from solution was summarized from the percentage difference between the H_2S concentration in the inlet and outlet solution. The difference at 100 °C corresponds to up to ~22% of the injected H_2S converted into sulfur containing minerals, like pyrite and possibly also into elemental

sulfur (e.g. Meyer, 1976; Stefánsson et al., 2011) whereas at 200, 240 and 250 °C the difference indicates ~62% of H_2S mineralized into pyrite and pyrrhotite at acidic pH and up to ~30% at neutral pH.

At each temperature, relatively steady state rates were observed within 1-2 days of the experiments, with rates increasing with decreasing pH of solution. The precipitation rates of H_2S are affected by the fluid's pH rather than by temperature and concentration. However, at 100 °C the precipitation rates of Fe did not correspond to the H_2S mineralization rate into sulfides completely, as elemental sulfur was also formed. In contrast, the H_2S mineralization rates at 250 °C closely correspond to the modeled Fe dissolution rates of basalt, based on mass balance. This suggests the limiting factor in H_2S mineralization on re-injection of H_2S-rich fluids into geothermal systems was the leaching rate and availability of Fe. The results of reactive transport calculations demonstrate that the H_2S mineralization depends on the secondary mineral paragenesis. Assuming that pyrite-clinozoisite-clinochlore (model I) dominate the alteration mineralogy, the greater part of the Fe released from basaltic glass was consumed by pyrite. In contrast, assuming that pyrite, pyrrhotite, prehnite and epidote dominate the alteration mineralogy (model II), less H_2S mineralization into pyrite was observed due to significant uptake of Fe by epidote. However, independent of modeled alteration mineralogy, pyrite was observed to preferentially form at the inlet side of the reactor, where Fe leaching rates are rapid.

Reactive transport simulations were extended to cover a duration of H_2S-rich fluid re-injection over 100 years at 250 °C with conditions similar to those observed at Hellisheiði and associated with the Sulfix project (Gunnarsson et al., 2013). The reactor dimensions were scaled up. The porosity close to the re-injection well was observed to increase with time due to vigorous dissolution of the basaltic glass and formation of secondary minerals dominated by pyrite and some chlorite and clinozoisite-epidote. A few meters into the geothermal reservoir, away from the outlet of the re-injection well, the fluid-rock interaction had reached fluid chemistry and alteration mineralogy patterns observed within natural geothermal systems. The system maintained a similar rate over whole duration, dissolving 26% of 2600 tonnes of initial basalt, and precipitating 114 tonnes of pyrite in 120 years, sequestrated 32 tonnes of H_2S (16% of injected H_2S within the modeled volume) without clogging the system. This means 32 000 tonne/year emissions at Hellisheði would be safely captured within volume of 0.001 km^3 of rock.

The findings are in favour of H_2S fluid injection into rocks as a sustainable method for reduction H_2S emissions from geothermal power plants. The method is also considerably cheaper than currently used procedures which also make it an economically feasible option.

Manuscript III (Appendix III)

Marieni, C., Přikryl, J., Aradóttir, E.S., Gunnarsson, I., Stefánsson, A., 2018. Towards green energy: Co-mineralization of carbon and sulfur in geothermal reservoirs. (submitted to *International Journal of Greenhouse Gas Control*)

The third manuscript aims at assessing the process of CO_2 and H_2S mineralization in geothermal systems in relation to the gas sequestrations. Interactions with basaltic, dacitic and rhyolitic glass was studied at 250°C.

The successful sequestration of CO_2 and H_2S through re-injection was demonstrated by the difference between inlet and outlet solutions in all cases, for mafic, intermediate, and felsic rock types. The CO_2 mineralization rates normalized to geometric surface for experimental series of basalt, dacite and rhyolite were on average -7.2 ± 0.1, -7.4 ± 0.3, and -7.5 ± 0.2 (log mol/m^2/s), respectively. The corresponding H_2S rates were -8.2 ± 0.4, -8.2 ± 0.2, and -8.0 ± 0.2 (log mol/m^2/s). The secondary minerals found within all the post-experiment solids were mainly carbonates, sulfides, plagioclase, and epidote, in agreement with the natural mineral assemblages described for high-temperature geothermal fields (Browne, 1978; Gunnlaugsson and Arnórsson, 1982; Stefánsson and Arnórsson, 2002; Wiese et al., 2008). The inlet reactor side was characterized by the most abundant proportion of secondary minerals, whose mass decreases with distance. Also this side was enriched in carbonate and sulfide, indicating a rapid disequilibrium and saturation of carbon- and sulfur-rich minerals respectively, in the initial stage of fluid-rock interactions.

To date, only geothermal reservoir characterized by basalt as a host rock have been considered suitable for the co-injection and mineralization of CO_2 and H_2S (Matter et al., 2016; Gunnarsson et al., 2015). However most of the geothermal fields spread across the world are characterized by andesitic to acidic magmatic rocks. The current experimental findings extend and broaden the application of CO_2 and H_2S sequestration into geothermal system. To scale up the laboratory mineralization rates obtained to field conditions, the equivalent steady-state sequestration rates of CO_2 and H_2S for natural systems were calculated. Laboratory mineralization rates were multiplied with surface area of the rocks in the natural geothermal system and respective rock density. The current world total emissions from geothermal activity, before any abatement system, have been calculated to be ~10 Mt (megaton) of CO_2 per year, and ~0.2 Mt/yr of H_2S. The CO_2 emissions are on average 134 g/KWh, which is in agreement with the previously proposed 122 g/KWh (Fridriksson et al., 2016) based on a survey involving emissions from only the ~50% installed capacity. The H_2S emissions proposed here for the first time are on average 1.83 g/kWh. Both the averages were calculated for 97% of the geothermal capacity installed worldwide (Bertani, 2016). Using the field sequestration CO_2 and H_2S precipitation rates, and the gas emissions the sequestration capacity was calculated. The measured mineralization rates indicate that ~0.2-0.5 t of CO_2, and ~0.03-0.05 t of H_2S can be sequestrated annually per cubic meter, depending on reservoir lithology and surface area. No particular increment in gaseous emissions has been observed to be associated with a specific lithology. However, the nature of host rocks is a key parameter in the estimation of required volume to sequester CO_2 and H_2S.

From an economic perspective, the low-cost H_2S removal involved with the proposed method of gas re-injection could play a key role in the case of geothermal activities characterized by H_2S-rich fluids. The in-situ simultaneous re-injection of CO_2 and H_2S for geological storage could then act as an incentive to drastically decrease the greenhouse gas emissions while adopting an economically convenient H_2S abatement system, which would otherwise be very expensive. Also, the coupling of CO_2 and H_2S would optimize the space used by geothermal fields, the number of required facilities, and the capital invested for waste water disposal. The production of energy from renewable sources, such as geothermal fluids can be freed from polluting atmospheric emissions by their permanent mineralization underground, addressing one of the major environmental concerns on a global scale.

Manuscript IV (Appendix IV)

Přikryl, J., Stefánsson, A., Pearce, C.R., 2018. Tracing olivine carbonation and serpentinization in CO_2-rich fluids via magnesium exchange and isotopic fractionation (submitted to *Geochimica et Cosmochimica Acta*)

This manuscript is focused on fluid-rock interaction of simple geochemical closed system where forsterite was reacted with CO_2-rich aqueous solutions at 150°C and the solution chemistry, mineral alteration and magnesium isotope systematic were studied. The experimental work was accompanied by reaction modeling.

Two types of experiments were carried out with: (1) low initial CO_2 concentrations and (2) elevated initial CO_2 concentrations. The initial pH of the solutions in both cases was ~6.5 and was observed to increase to ~6.7 - ~7.5 with reaction time accompanied with a decrease in the CO_2 concentration. The concentrations of dissolved Si and Mg rose rapidly during the first hour followed by steady concentrations with time. Identified secondary phases were magnesite, chrysotile/lizardite, amorphous silica and halite. The altered olivine surfaces showed conical or funnel-shaped etch pits that formed along the mineral edges and within the previously smoothed surfaces. The effect of reaction time at constant initial CO_2 concentration can be summarized as following. Initially, small crystals of magnesite formed, up to 1 μm, on the olivine grains. Following this randomly distributed needle shaped formations of chrysotile/lizardite up to 0.5 μm in length formed. With time, the magnesite crystals were observed to grow in size. No major differences in mineralogy were observed depending on initial CO_2 concentration. At low CO_2 concentration, magnesite crystals formed along the olivine edges and within surface cleavages, small chrysotile/lizardite needles formed randomly over the whole olivine surface. At elevated CO_2 concentration, magnesite resulted in crystals larger, up to 10 μm. Some of the olivine grains were completely coated with such conglomerates of magnesite. Honeycomb structures and mesh texture of chrysotile/lizardite typically coated the olivine surface and occasionally shaped conglomerates around the magnesite crystals.

The reaction modeling was observed to imitate the experimental observations, both with respect to the solution chemistry and secondary mineralogy. The exact solution composition and mass of secondary minerals, as well as the effects of element transfer with time, was found to largely depend on the fraction of the total olivine surface area reacting. The effects of the choice of the nucleation surface area values (A_n) for the secondary mineral phases was found to have a limited effect on the mass of secondary minerals formed in the model runs. Comparison of the experimental and modeling results demonstrated that although kinetic reaction path modeling is unable to reproduce all of the observed chemical changes, it does provide an accurate representation of the relative trends in secondary mineralogy, solution composition and element transfer as a function of time, at least for the relatively simple systems such as that investigated here.

The reaction progress was further studied using δ^{26}Mg ratios of water samples and fresh and reacted forsterite. Upon olivine-water reaction the δ^{26}Mg solution ratio decreased initially from -0.14 to -0.27 ‰ followed by an increase to 0.35 ‰. This is considered to be related to Mg-containing secondary minerals formation enriched by ^{24}Mg relative to olivine and the aqueous solution upon fluid-rock interaction. Similar results were obtained using reaction and isotope modeling, further indicating that magnesite is significantly ^{24}Mg enriched compared to chrysotile and brucite. The results of our study are consistent with

the relatively positive δ^{26}Mg ratios (0.23 ‰ to 0.85 ‰) of ground- and geothermal waters in basaltic terrains (Pogge von Strandmann et al., 2008) and altered oceanic basalts with the most negative values being associated with the carbonation of the basalts, and less negative values associated with serpentinization. Revealing mechanism of Mg isotope distribution within reaction progress in nature indicates also application as a tracer during CO_2 sequestration.

Contribution of JP to the presented research

Paper I

JP carried out all experimental work, including designing the experimental apparatus, JP conducted analytical measurements according the instruction of the managing technical staff and written and ran geochemical numerical simulations. Writing was done by JP, AS, SS, DJ.

Paper II

JP carried out preparation of the material together with SG, helped partly with the experimental work and with analytical measurements. JP conducted reactive transport simulations. Paper was written by JP, CM, AS.

Manuscript III

JP and CM contributed equally to the experimental work and analytical measurements. CM analyzed the economic implications and world emissions. Manuscript was prepared by CM, JP, AS.

Manuscript IV

All experimental work was managed by JP. Analytical measurements were done by JP according the guidance of the managing technical staff, except isotope samples analyzed by CP. JP ran all geochemical modeling. Manuscript was written by JP, AS, CP.

3 Concluding remarks

The aim of this work was to study fluid-rock interaction under hydrothermal conditions including: (1) dissolution of primary rock and changes in rock porosity and mineral surface areas upon reaction time; (2) tracing progressive fluid-rock interaction using solution chemistry, mineralogy and isotope systematics and (3) assessing the mechanism, rate and the effects of rock porosity upon H_2S and CO_2 mineralization under geothermal conditions, and long term sustainability of H_2S and CO_2 sequestration in geothermal systems. Two methods were applied, laboratory fluid-rock interaction experiments and reactive transport modeling. Comparison of the two also made it possible to assess the reliability of reaction and reactive transport modeling for a real system.

The study demonstrated that mineral and rock dissolution in the absence of secondary phases results in increased porosity and specific surface area of the solids. Such changes may not be evenly distributed along the fluid transport path and over time. Reactive transport modeling of the same systems indicated that bulk changes in solution chemistry and dissolution rates could be accurately simulated. In contrast, changes in pore volume distribution and mineral surface areas are more difficult to accurately model. In the case of closed system fluid-rock interaction whereas primary minerals are dissolved and secondary minerals are formed, experimental mineralogy with solution chemistry and isotope ratio may be mimicked by geochemical modeling, at least for simple systems.

Applying similar experimental and modeling approach to CO_2 and H_2S sequestration by mineralization in geothermal systems results in the rate of mineralization and long-term sustainability of such sequestration. The re-injection of CO_2 and H_2S into geothermal systems were found to result in primary rock dissolution and calcite solid solution and pyrite formation. The overall process resulted in limited effects of long-term porosity changes. For various rock types the co-sequestered H_2S and CO_2 reached 52% and 36% for basalt, 17% and 12% for intermediate rocks, and 15% and 40% for felsic rocks respectively, for the injected gases during limited transport length of tested systems at 250°C. Single injection of H_2S mineralized up to 62%, faster in acidic pH and higher H_2S concentration >10 mmol/kg. Stable H_2S mineralization is also achieved at 200-250°C. The measured mineralization rates indicate that ~0.2-0.5 t of CO_2, and ~0.03-0.05 t of H_2S can be sequestrated annually per cubic meter. Field calculations show that a total rock sequestration capacity of 0.03 km^3 would be sufficient to store the annual world CO_2 and H_2S geothermal emissions. Annual sequestration volumes indicate efficient abatement of CO_2 and H_2S emissions at field conditions, suggesting the strategy sustainability for lifetime of geothermal power plants, also in different lithologies.

References

Aagaard, P., Helgeson, H. C., 1982. Thermodynamic and kinetic constraints on reaction rates among minerals and aqueous solutions: I. Theoretical considerations. *American Journal of Science, 282(3)*, pp.237–285.

Arnórsson, S., 2004. Environmental impact of geothermal energy utilization. Geological Society, London, Special Publications, 236(1), pp.297-336.

Arnórsson, S.; Bjarnason, J. Ö.; Giroud, N.; Gunnarsson, I.; Stefánsson, A., 2006. Sampling and analysis of geothermal fluids. *Geofluids*, *6*, (3), 203-216.

Arnórsson, S., Gunnlaugsson, E. and Svavarsson, H., 1983. The chemistry of geothermal waters in Iceland. II. Mineral equilibria and independent variables controlling water compositions. *Geochimica et Cosmochimica Acta*, *47*(3), pp.547-566.

Appelo, C.A.J., Postma, D., 2005. Geochemistry, groundwater and pollution, *Balkema, Roterdam*.

Bertani, R., 2016. Geothermal power generation in the world 2010–2014 update report. *Geothermics, 60*, pp.31-43.

Brown, G.E. and Calas, G., 2012. Mineral-aqueous solution interfaces and their impact on the environment. *Geochemical Perspectives*, *1*(4-5), pp.483-484.

Browne, P. R. L., 1978 Hydrothermal alteration in active geothermal fields. *Annual Review of Earth and Planetary Sciences*, *6* (1), pp.229-248.

Fridriksson, T.; Mateos, A.; Audinet, P.; Orucu, Y., 2016. Greenhouse gases from geothermal power production. World Bank, Washington, DC. © World Bank. https://openknowledge.worldbank.org/handle/10986/24691 License: CC BY 3.0 IGO 2016.

Gaus, I., Audigane, P., Andre, L., Lions, J., Jacquemet, N., Durst, P., Czernichowski-Lauriol, I. and Azaroual, M., 2008. Geochemical and solute transport modelling for CO_2 storage, what to expect from it? *International Journal of Greenhouse Gas Control, 2*(4), pp.605-625.

Giggenbach, W.F., 1980. Geothermal gas equilibria. *Geochimica et cosmochimica acta*, *44*(12), pp.2021-2032.

Giggenbach, W.F., 1981. Geothermal mineral equilibria. *Geochimica et Cosmochimica Acta*, *45*(3), pp.393-410.

Gislason, S.R. and Oelkers, E.H., 2003. Mechanism, rates, and consequences of basaltic glass dissolution: II. An experimental study of the dissolution rates of basaltic glass

as a function of pH and temperature. *Geochimica et Cosmochimica Acta*, *67*(20), pp.3817-3832.

Gouze, P., Luquot, L., 2011. X-ray microtomography characterization of porosity, permeability and reactive surface changes during dissolution. *Journal of Contaminant Hydrology, 120-121*, pp.45–55.

Gouze, P., Noiriel, C., Bruderer, C., Loggia, D., Leprovost, R., 2003. X-ray tomography characterization of fracture surfaces during dissolution. *Geophysical Research Letters, 30*(5).

Gysi, A.P. and Stefánsson, A., 2012a. Mineralogical aspects of CO_2 sequestration during hydrothermal basalt alteration—An experimental study at 75 to 250 C and elevated pCO 2. *Chemical Geology*, *306*, pp.146-159.

Gysi, A.P., Stefánsson, A., 2012b. Experiments and geochemical modeling of CO_2 sequestration during hydrothermal basalt alteration. *Chemical Geology, 306-307*, pp. 10–28.

Gunnarsson, I., Aradóttir, E.S., Sigfússon, B., Gunnlaugsson, E., Júlíusson, B.M., 2013. Geothermal gas emission from Hellisheiði and Nesjavellir power plants, Iceland. Reykjavík Energy. *GRC Transactions, 37*, pp.785-789.

Gunnarsson, I., Júlíusson, B. M., Aradóttir, E., Arnarson, M. T., 2015. In Pilot Scale Geothermal Gas Separation, Hellisheiði Power Plant, Iceland, *World Geothermal Congress 2015, Melbourne, Australia*.

Gunnlaugsson, E., Arnòrsson, S., 1982 The chemistry of iron in geothermal systems in iceland. *Journal of Volcanology and Geothermal Research, 14* (3), pp.281-299.

Hövelmann, J., Austrheim, H., Beinlich, A. and Munz, I.A., 2011. Experimental study of the carbonation of partially serpentinized and weathered peridotites. *Geochimica et cosmochimica Acta, 75(22)*, pp.6760-6779.

Helgeson, H. C., Murphy W. M., Aagaard, P., 1984. Thermodynamic and kinetic constraints on reaction rates among minerals and aqueous solutions. II. Rate constants, effective surface area, and the hydrolysis of feldspar. *Geochimica et Cosmochimica Acta, 48*, pp.2405–2432.

Johnson, N.C., Thomas, B., Maher, K., Rosenbauer, R.J., Bird, D. and Brown, G.E., 2014. Olivine dissolution and carbonation under conditions relevant for in situ carbon storage. *Chemical Geology*, *373*, pp.93-105.

Knauss, K.G., Johnson, J.W. and Steefel, C.I., 2005. Evaluation of the impact of CO_2, co-contaminant gas, aqueous fluid and reservoir rock interactions on the geologic sequestration of CO_2. *Chemical geology, 217*(3), pp.339-350.

Kristmannsdóttir, H., 1976. Types of clay minerals in hydrothermally altered basaltic rocks, Reykjanes, Iceland. *Jökull* 26, pp.30-39.

Lasaga, A., 1998. Kinetic Theory in the Earth Sciences. *Princeton University Press, New Jersey*.

Luquot, L., Gouze, P., 2009. Experimental determination of porosity and permeability changes induced by injection of CO_2 into carbonate rocks. *Chemical Geology, 265*, pp. 148-159.

Marini, L., 2006. Geological sequestration of carbon dioxide: thermodynamics, kinetics, and reaction path modeling (Vol. 11). *Elsevier*.

McPherson, B.J.O.L. and Lichtner, P.C., 2001, May. CO_2 sequestration in deep aquifers. *In Proceedings: first national conference on carbon sequestration, Washington, DC*.

Meyer, B., 1976. Elemental sulfur. *Chemical Reviews*, 76, pp.367-388.

Nielsen, M.R., Sand, K.K., Rodriguez-Blanco, J.D., Bovet, N., Generosi, J., Dalby, K.N. and Stipp, S.L.S., 2016. Inhibition of Calcite Growth: Combined Effects of Mg2+ and SO42–. *Crystal Growth & Design*, *16*(11), pp.6199-6207.

Noiriel, C., Luquot, L., Madé, B., Raimbault, L., Gouze, P., van der Lee, J., 2009. Changes in reactive surface area during limestone dissolution: An experimental and modelling study. *Chemical Geoogy, 265*, pp.160–170.

Noiriel, C., Steefel, C.I., Yang, L., Ajo-Franklin, J., 2012. Upscaling calcium carbonate precipitation rates from pore to continuum scale. *Chemical Geology, 318*, pp.60–74.

Noiriel, C., Steefel, C.I., Yang, L., Bernard, D., 2015. Effects of pore-scale precipitation on permeability and flow. *Advances in Water Resources, 95*, pp.125-137.

Oelkers, E.H., Gíslason, S.R., 2001. The mechanism, rates and consequences of basaltic glass dissolution: I. An experimental study of the dissolution rates of basaltic glass as a function of aqueous Al, Si and oxalic acid concentration at 25°C and pH = 3 and 11. *Geochimica et Cosmochimica Acta, 65,* pp.3671–3681.

Palandri, J.L. and Kharaka, Y.K., 2005. Ferric iron-bearing sediments as a mineral trap for CO_2 sequestration: iron reduction using sulfur-bearing waste gas. *Chemical Geology, 217*(3), pp.351-364.

Parkhurst, D.L., Appelo, C.A.J., 2013. Description of input and examples for PHREEQC version 3—a computer program for speciation, batch-reaction, one-dimensional transport, and inverse geochemical calculations. *US geological survey techniques and methods, book 6,* p.497.

Parkhurst, D.L., Wissmeier, L., 2015. PhreeqcRM: A reaction module for transport simulators based on the geochemical model PHREEQC. *Advances in Water Resources,* 83, pp.176-189.

Pearce, C. R., Saldi, G. D., Schott, J., Oelkers, E. H., 2012. Isotopic fractionation during congruent dissolution, precipitation and at equilibrium: evidence from Mg isotopes. Geochim. Cosmochim. Ac., 92, 170-183. doi.org/10.1016/j.gca.2012.05.045

Pokrovsky, O.S. and Schott, J., 1999. Processes at the magnesium-bearing carbonates/solution interface. II. kinetics and mechanism of magnesite dissolution. *Geochimica et cosmochimica acta*, *63*(6), pp.881-897.

Pokrovsky, O.S., Schott, J., 2000. Kinetics and mechanism of forsterite dissolution at 25°C and pH from 1 to 12. *Geochimica et Cosmochimica Acta 64*, pp.3313-3325.

Pogge von Strandmann, P.A.E., Burton, K.W., James, R.H., van Calsteren, P., Gislason, S.R., Sigfusson, B., 2008. The influence of weathering processes on riverine magnesium isotopes in a basaltic terrain. *Earth and Planetary Science Letters*, 276, pp.187–197.

Putnis, A., 2014. Why mineral interfaces matter. *Science*, *343*(6178), pp.1441-1442.

Saldi, G.D., Jordan, G., Schott, J., Oelkers, E.H., 2009. Magnesite growth rates as a function of temperature and saturation state. *Geochimica et Cosmochimica Acta, 73*(19), pp. 5646-5657.

Saldi, G.D., Daval, D., Morvan, G., Knauss, K.G., 2013. The role of Fe and redox conditions in olivine carbonation rates: an experimental study of the rate limiting reactions at 90 and 150 C in open and closed systems. *Geochimica et Cosmochimica Acta, 118*, pp. 157-183.

Sanopoulos, D. and Karabelas, A., 1997. H_2S Abatement in Geothermal Plants: Evaluation of Process Alternatives. *Energy sources*, *19*(1), pp.63-77.

Schott, J., Pokrovsky, O.S., Oelkers, E.H., 2009. The link between mineral dissolution/precipitation kinetics and solution chemistry. *Reviews in mineralogy and geochemistry, 70*(1), pp.207-258.

Steefel, C.I, Maher, K., 2009. Fluid-rock interaction: A reactive transport approach. *Reviews in mineralogy and geochemistry*, *70*(1), pp.485-532.

Stefánsson, A., 2017. Gas chemistry of Icelandic thermal fluids. *Journal of Volcanology and Geothermal Research*. https://doi.org/10.1016/j.jvolgeores.2017.04.002

Stefánsson, A., Arnórsson, S., 2002. Gas pressures and redox reactions in geothermal fluids in Iceland. *Chemical Geology*, *190* (1–4), pp.251-271.

Stefánsson, A., Arnórsson, S., Gunnarsson, I., Kaasalainen, H., Gunnlaugsson, E., 2011. The geochemistry and sequestration of H2S into the geothermal system at Hellisheidi, Iceland. *Journal of Volcanology and Geothermal Research,* 202, pp. 179-188.

Techer, I., Advocat, T., Lancelot, J. and Liotard, J.M., 2001. Dissolution kinetics of basaltic glasses: control by solution chemistry and protective effect of the alteration film. *Chemical Geology*, *176*(1), pp.235-263.

Tómasson, J. and Kristmannsdóttir, H., 1972. High temperature alteration minerals and thermal brines, Reykjanes, Iceland. *Contributions to Mineralogy and Petrology*, *36*, 123-134.

Xu, T., Apps, J.A. and Pruess, K., 2003. Reactive geochemical transport simulation to study mineral trapping for CO_2 disposal in deep arenaceous formations. *Journal of Geophysical Research: Solid Earth*, *108*(B2).

Zerai, B., Saylor, B.Z. and Matisoff, G., 2006. Computer simulation of CO_2 trapped through mineral precipitation in the Rose Run Sandstone, Ohio. *Applied Geochemistry*, *21*(2), pp.223-240.

Appendix I

Appendix I

Mineral dissolution in porous media: An experimental and modeling study on kinetics, porosity and surface area evolution

Jan Přikryl[1], Diwaker Jha[2], Andri Stefánsson[1], Susan Stipp[2]

[1]Institute of Earth Sciences, University of Iceland, Sturlugata 7, 101 Reykjavik, Iceland

[2]Nano-Science Center, Department of Chemistry, University of Copenhagen, Denmark

Applied Geochemistry, 2017

Highlights:

- Bulk dissolution rates from flow-through and mixed-flow reactors are similar.
- Increased porosity and surface area affected dissolution rates and fluid composition.
- Modeling does not accurately predict porosity and surface area in time and distance.
- Non-stoichiometric dissolution is observed, commonly missing in reactive modeling.

Keywords: Dissolution; Flow-through experiment; Surface area; Porosity; Porous medium; Tomography; Kinetic model

Applied Geochemistry 87 (2017) 57–70

Contents lists available at ScienceDirect

Applied Geochemistry

journal homepage: www.elsevier.com/locate/apgeochem

Mineral dissolution in porous media: An experimental and modeling study on kinetics, porosity and surface area evolution

Jan Přikryl [a, *], Diwaker Jha [b], Andri Stefánsson [a], Susan Stipp [b]

[a] Institute of Earth Sciences, University of Iceland, Sturlugata 7, 101 Reykjavík, Iceland
[b] Nano-Science Center, Department of Chemistry, University of Copenhagen, Denmark

ARTICLE INFO

Article history:
Received 26 January 2017
Received in revised form
20 April 2017
Accepted 1 May 2017
Available online 4 May 2017

Editorial handling by Prof. M. Kersten

Keywords:
Dissolution
Flow-through experiment
Surface area
Porosity
Porous medium
Tomography
Kinetic model

ABSTRACT

Mineral and rock dissolution was studied experimentally using flow-through reactors and reactive transport modeling. The porous media were forsterite, crystalline basalt, and amorphous basalt, dissolved in HCl solutions at pH ~2.5 and 25 °C. Solution composition, particle surface area, and porosity were determined as a function of travel distance within the reactor and time, using in situ X-ray computed tomography (XMT) and solution chemical composition. The obtained bulk dissolution rates, normalized to the initial geometric surface area, were: log $r_{+,Si}$ −7.59 ± 0.05 for forsterite, −7.64 ± 0.12 for basaltic glass and −8.12 ± 0.24 (mol/m^2/s) for crystalline basalt, at 25 °C and pH ~2.5, similar to those previously obtained using mixed flow reactors and for conditions far from equilibrium. Mineral and rock dissolution resulted in increased porosity and specific surface area of the solids; these changes were not uniformly distributed along the fluid flow path or with time. Similar trends were predicted by reactive transport modeling, however, the exact values of pore volume and surface area were difficult to predict. The results were found to be independent of the method applied in the surface area calculations: either the simple spherical model or the sugar lump model. Also, in the models, stoichiometric mineral dissolution is commonly assumed, but was not observed to occur for either glassy or crystalline basalt. It shows that accurate prediction capabilities of simple reactive transport modeling may be limited for calculating pore volume, mineral and rock surface area changes, and pore fluid chemistry with time and along flow paths. These, in turn, are key parameters in determining dissolution rates, overall chemical mass movement in the system, and fluid flow paths and velocities.

1. Introduction

Weathering and alteration of rocks by water-rock interaction play a key role in many geochemical cycles, for example in forming landscapes and soils (Brantley et al., 2008), in the effectiveness of carbon capture and storage (e.g., McGrail et al., 2006; Gíslason and Oelkers, 2014), in acid mine drainage, and in the transport of toxic elements (e.g. Akcil and Koldas, 2006; Gandy et al., 2007).

The initial step of water-rock interaction in porous media is dissolution of primary minerals by fluid, usually water, resulting in dissolved solutes and formation of secondary minerals. Commonly, the rate of the overall water-rock interaction is quantified by change in solution composition as a function of time. Most common are dissolution experiments (e.g., Pokrovsky and Schott, 2000; Oelkers and Gíslason, 2001) but rates of secondary mineral formation have also been determined (e.g., Nagy et al., 1991; Saldi et al., 2009). In porous rocks, mineral dissolution and formation of secondary minerals may also cause changes in pore volume, permeability and mineral surface area, however, these effects have received less attention (e.g., Kieffer et al., 1999; Colón et al., 2004).

Dissolution rates determined from experiments are commonly higher than those determined from field studies (e.g. White and Brantley, 2003). The causes can be many. Dissolution rates are influenced by available mineral surface area and the availability and transport of water to and from those surfaces. The surfaces of natural minerals may be previously weathered compared with those used in experiments, this affecting the measured dissolution rates. Moreover, mineral surface area may vary and change during progressive water-rock interaction and weathering and water transport are influenced by the porosity and permeability of the rocks. In recent years, advances in computed tomography (CT) have provided new insight into water-rock interaction in porous media,

* Corresponding author.
E-mail address: jap5@hi.is (J. Přikryl).

http://dx.doi.org/10.1016/j.apgeochem.2017.05.004
0883-2927/

particularly the changes in porosity and particle surface area (e.g., Noiriel et al., 2004, 2009; 2012; Noiriel, 2015; Luquot and Gouze, 2009; Gouze and Luquot, 2011; Cnudde and Boone, 2013; Molins et al., 2014). These studies have demonstrated that dissolution and precipitation kinetics can be influenced by fluid transport and availability of surface area and that surface area and porosity usually change as a function of flow path and progressive water-rock interaction.

This study focused on water-rock interaction and mineral dissolution in porous media. Flow-through experiments were conducted where the dissolution of single and multiphase, unconsolidated porous media, with crystalline or amorphous material, was investigated. The progress of the reaction was followed by in situ imaging and by chemical analysis, which allowed changes in local porosity and surface area to be determined along the flow path, as a function of time. The chemical composition data were used to determine dissolution rates. The experimental data were compared with results from reactive transport modeling, to validate prediction capabilities of such model calculations for solution composition and changes in porosity and mineral surface area.

2. Methods

2.1. Experimental details

Three materials were used for the experiments: basaltic glass (BG) as an amorphous single phase, crystalline basalt (XB) as a crystalline multiphase and forsterite (FO) representing a crystalline single phase system. The composition of the basaltic glass was close to that of mid-ocean ridge basalt (MORB) and was collected from Stapafell, SW Iceland. The material has been described previously (e.g., Oelkers and Gíslason, 2001; Gíslason and Oelkers, 2003; Gysi and Stefánsson, 2012a,b,c; Stockmann et al., 2011; Galeczka et al., 2014). The bulk composition of the crystalline basalt was similar to the basaltic glass and was collected at the same locality. The mineralogy and petrology of the material have previously been reported by Gudbrandsson et al. (2011). The forsterite ($Mg_{1.86}Fe_{0.14}SiO_4$) used in this study was collected in Gusdal quarry, in the Almklovdalen peridotite massif, situated in the Western Gneiss Region, Norway (Brueckner et al., 2010).

The solid materials were broken in a jaw crusher, then ground in an automatic agate mortar and dry sieved to obtain the 125–250 μm size fraction. We used gravitational settling in deionized ultrapure water and the water further served to remove the ultrafine particles. The material was rinsed with deionized water and acetone in an ultrasonic bath and dried in an oven at 40 °C. A summary of the chemical and physical properties of the starting material is given in Table 1 and SEM images of the fresh material are shown in Fig. 1. The specific geometric surface area of the starting materials was determined as (Tester et al., 1994),

$$A_{geo} = \frac{6}{de * \rho} \quad (1)$$

the constant, 6, is a shape factor, used for grains that are spherical and smooth. The effective particle diameter is denoted *de*, and ρ stands for the density of the material. The BET specific surface area of cleaned and dried starting materials was determined by six point nitrogen adsorption, using a Quantachrome Gas Sorption system.

The dissolution experiments were conducted at 25 °C using a flow-through reactor system, consisting of an inlet solution, a peristaltic pump, a vertically placed reaction vessel and an outlet tube. The cylindrical Teflon reactor had a volume of 8.80 cm^3, length (l) of 11.2 cm and internal diameter (Ø) of 0.5 cm. The reactors had thin walls (3 mm) for in situ X-ray microtomography (XMT) measurements as a function of reaction time and distance along the flow path within the reactor. Prior to the experiments, the reactor was loaded with one of the solid materials, in suspension, to optimize homogeneous particle distribution and to avoid preferential channeling.

The inlet solutions were made from HCl (37% Sigma-Aldrich) and deionized water to form 8.44–8.68 mmol/kg HCl with pH of 2.10–2.11. The solutions were pumped at a constant flow rate (0.5 ml/min) through the columns. The solid material and the inlet and outlet solution compositions were determined during the experimental runs. A schematic figure of the experimental setup is presented in Fig. 2, together with an example of 3D XMT images of the material before and after dissolution, taken in situ. The experimental conditions are summarized in Table 2.

2.2. Solid material analysis

The solid materials were analyzed at the beginning and at the end of the experiments. Scanning electron microscopy (SEM, HITACHI TM-3000) showed the morphology of the grains. Images of gold coated samples were taken at an accelerating voltage of 15 kV, at a range of magnifications. The chemical composition of the fresh material was determined using an electron microprobe (JEOL JXA-8200 Superprobe), at an accelerating voltage of 15 kV, a beam current of 15 nA, and a beam size of 1–5 μm.

2.3. Solution composition and dissolution rates

Solution samples for chemical analysis were collected at the

Table 1
Physical and chemical properties of the starting solid material used in the experiments.

	Basaltic glass (BG)	Crystalline basalt (XB)	Forsterite (FO)
Chemical composition	$Na_{0.081}K_{0.008}Mg_{0.282}Ca_{0.263}Fe_{0.171}Al_{0.358}SiO_{3.297}$ [a]	18% fo 37% cpx 45% plag [b] fo - $Mg_{1.68}Fe_{0.32}SiO_4$ [b] cpx - $Ca_{0.4175}Mg_{0.399}Fe_{0.209}Si_{0.973}O_3$ [b] plag - $Ca_{0.67}Na_{0.33}Al_{1.55}Si_{2.416}O_8$ [b]	$Mg_{1.86}Fe_{0.14}SiO_4$
Grain size	125–250 μm	125–250 μm	125–250 μm
Material (g)	12.96	13.61	17.41
Geometric surface area (A_{geo}) (m^2/g)	0.0303	0.0284	0.0263
BET surface area (A_{BET}) (m^2/g) literature	1.533 [c]	0.812 [b]	0.088 [d]
BET surface area (A_{BET}) (m^2/g) this study (N_2)	5.274	0.924	0.079
X-ray microtomography surface area (A_{XMT}) (m^2/g)	0.0118	0.0127	0.0137
X-ray microtomography porosity (ϕ_{XMT}) (%)	49.53	51.74	41.90

[a] Oelkers and Gíslason (2001).
[b] Gudbrandsson et al. (2011). The composition of cpx has been simplified to exclude Al and to be consistent with the mineral solubilities.
[c] Aradóttir et al. (2013).
[d] Giammar et al. (2005).

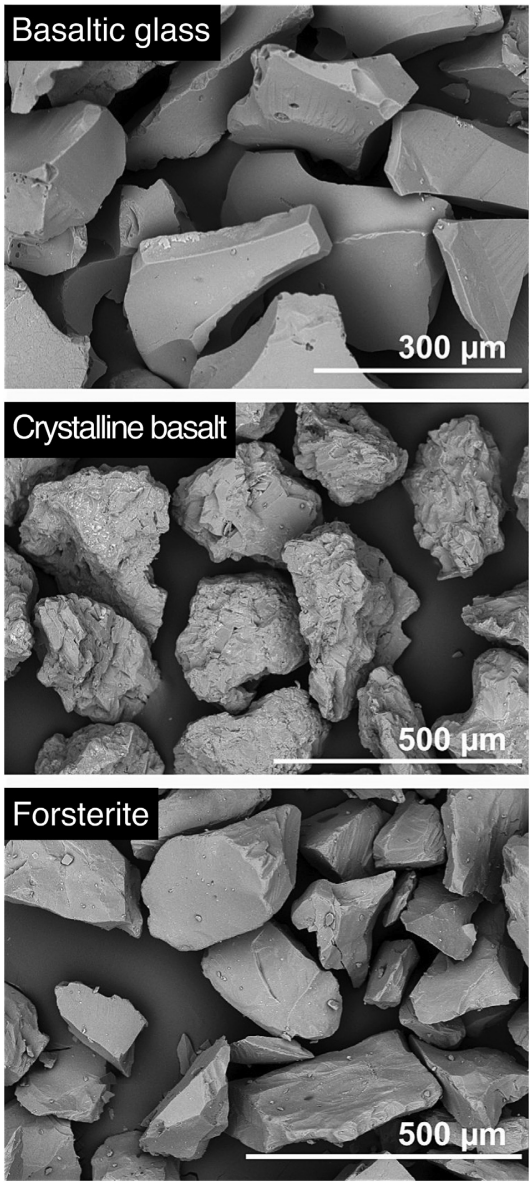

Fig. 1. SEM images of unreacted starting materials.

inlet and outlet of the flow-through reactor. The solutions were filtered through 0.2 μm cellulose acetate filters. Two aliquots were collected, one for pH determination with a glass electrode (Cole-Parmer), that was calibrated against NBS standard buffers, and another that was acidified with 1% HNO_3 (Merck Suprapur®) for major element analysis (Si, Na, K, Ca, Mg, Fe, Al, B and Cl) by ICP-OES (Spectro Ciros Vision). The analytical uncertainty, based on repeated analysis of an internal standard (GYG13) at the 95% confidence level, ranged from 0.3 to 4.8% for the various elements. The absolute error of the pH measurements was estimated to be ±0.05 pH units. The results were obtained by comparing the measured pH of several solutions using an electrode calibrated against the standard buffers as well as with a more rigorous standard addition calibration with acid-base titration and determination of standard potential, Nernstian slope, and acid and alkaline liquid junction potentials.

Based on the difference in chemical composition of the inlet and outlet solutions, the forward dissolution rate (r_{+i}) was calculated from the expression,

$$r_{+i} = \frac{\Delta m_i q}{A} \tag{2}$$

where Δm_i represents the concentration difference between the inlet and outlet solutions for the i-th element, Δm_i was divided by stoichiometric coefficient of the i-th element in the case of Mg, and q denotes flow rate. The surface area, A, was assumed to be the initial geometric surface area of the material inside the reactor or the surface area determined from the 3D XMT images as a function of time. The dissolution rates were derived using the Si and Mg concentrations.

Exact mass of residual material in the reactor for XMT normalized dissolution rate was obtained from the mass of dissolved material ($\Delta M(t)$) calculated from the following equation:

$$\Delta M(t) = \sum_{i=1}^{n} m_i(t) \text{ where } m_i(t) = \int_0^t (c_{i,\,in} - c_{i,\,out}(t))q(t)\ dt \tag{3}$$

with $c_{i,\,in}$ and $c_{i,\,out}$ as the concentrations of the i-th cation (mmol/kg) in the inlet and outlet fluids respectively, q the flow-rate (L/s) and m_i the total moles of cation released from the sample at time t. The total mass of cations was converted to mass of respective oxides (SiO_2, Al_2O_3, CaO, MgO, FeO).

2.4. X-ray microtomography, calculation of porosity and specific surface area

Tomography measurements were made using a Phoenix Nanotom S X-ray microCT system (General Electric Measurement and Control) situated at Innovation Center Iceland, Reykjavík, at a source current of 140 μA, a source voltage of 120 kV and a sampling distance of 7.83–8.83 μm. Measurements were made on the original material, prior to the experiments, and after 2 and 4 weeks of dissolution, for the inlet (z = 20–27 ± 2 mm) and outlet portions of the reactor (z = 100–107 ± 2 mm). Two phase (solid and fluid) reconstructed 3D tomography data was processed as follows: 1) Each voxel, $I_{(x,y,z)}$ with intensity value greater than $(\mu_{(I)} + 3\sigma_{(I)})$ was replaced by $(\mu_{(I)} + 3\sigma_{(I)})$. Here, $\mu_{(I)}$ is the mean intensity value and $\sigma_{(I)}$, the standard deviation of the tomogram's voxel values. This removed any outlier patch of pixels. 2) Noise level was estimated following Liu et al. (2013). 3) Bilateral filtering was performed using the noise level parameter obtained in Step 2 (Tomasi and Manduchi, 1998). 4) At this point, voxels representing solid and fluid were segmented by setting a threshold level obtained by Otsu method (Otsu, 1979). These steps improved the segmentation by minimizing false pore matrix indicators (Jha et al., 2014). The intensity histograms show a clear bimodal distribution after the processing steps, which allows a reliable and automatic selection of threshold levels (Fig. 3). We calculated the digital surface area (pixel^2) of the segmented binary data by counting marching cube surface values in it. Total digital surface area was converted to physical surface area (in m^2) by multiplying it with the area of a voxel's face. The porosity, ϕ, was given by $\frac{V-V_s}{V}$, where V is the total volume of voxels in the tomogram and V_s is the total solid phase

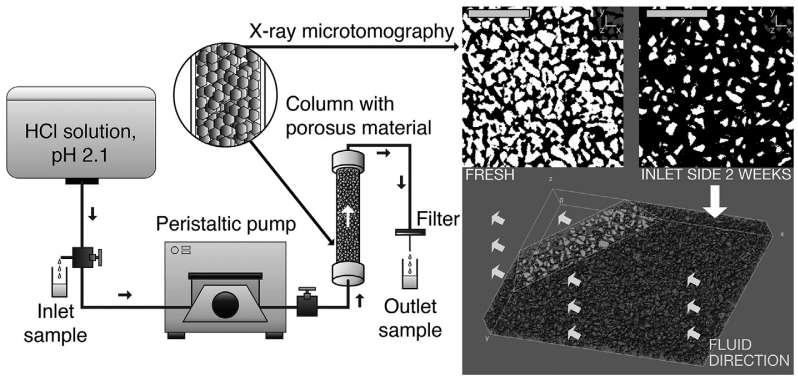

Fig. 2. A schematic diagram for the X-ray microtomography setup, consisting of inlet solution, peristaltic pump, flow-through reactor and outlet sampling port. The reactor was made of Teflon with a wall thickness of 3 mm to allow in situ X-ray scanning. Examples of raw, binarized data are presented, with a 3 dimensional reconstruction of the porous media. The scale bar on the tomogram slices is 600 μm.

Table 2
Summary of the parameters for the experiments.

	Basaltic glass (BG)	Crystalline basalt (XB)	Forsterite (FO)
Exp. #	BG 0-9	XB 0-11	FO 0-10
Temperature (°C)	25	25	25
Duration (days)	29	30	30
Flow rate (ml/min)	0.48–0.53	0.41–0.54	0.40–0.54
Solution compostion HCl (mmol/kg)	8.40–8.60	8.25–8.74	8.11–8.74
Solution pH at 25 °C	2.11–2.85	2.10–2.34	2.10–2.86
Solid material SEM analysis Exp. #	0, 9	0, 11	0, 10
Porosity analysis Exp. #	0, 5, 9	0, 6, 11	0, 7, 10
Surface area analysis Exp.#	0, 5, 9	0, 6, 11	0, 7, 10

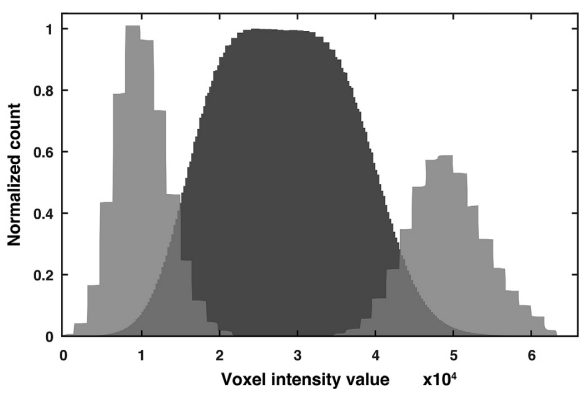

Fig. 3. Intensity histogram of the tomogram voxels before (black) and after (gray) processing steps, which allow automatic determination of threshold level.

voxel count. The mass (g) of the solid material was obtained from V_s and the material density, ρ. This consequently allowed us to calculate specific surface area in commonly used units (m^2/g). In order to calculate the tomographic surface normalized dissolution rates, the average surface area, $\overline{X}$, over all of the solid was calculated as the arithmetic mean,

$$\overline{X} = \frac{1}{n}\sum_{i=1}^{n} X_i \tag{4}$$

where n represents the set of sample and X_i, the specific surface area of samples. Consequently average surface area, $\overline{X}$, was multiplied with the residual mass of material to obtain total surface area.

2.5. Reactive transport modeling

Reactive transport modeling was conducted using the PHREEQC program (Parkhurst and Appelo, 2013). The reactor was divided into 10 reactive cells to track reaction progress as a function of column distance, with a total 52 to $62 \cdot 10^3$ transport calculation steps per cell to calculate 1 month of experimental duration. This number of transport shifts depended on the initial pore volume and corresponding solution refill rate; the time step associated with each shift was close to 1 minute. 1D advective-dispersive-reactive transport of the solution was determined using the forward flow direction from cell 1 up to cell 10 to mimic experimental behavior (Appelo and Postma, 2005). Dispersivity in each cell (10% of travelled distance) was corrected for the total length of the cell and we assumed no diffusion.

The rate of dissolution was calculated using the transition state theory for the i-th solid phase,

$$r_{+i} = A_i \sum_i \left(k_{T,i} \prod_j a_j^n \right) (1 - SI_i) \tag{5}$$

where A represents the surface area, k_T represents the kinetic rate constant at a given pH and temperature, and $\prod a_j^n$ represents the activity expression for the j-th dissolved aqueous species in the solution, to the power of the reaction order of species j, n.

The saturation index, SI, was calculated from,

$$SI_i = Q_i/K_i \quad (6)$$

where Q denotes the reaction quotient of the dissolution reaction and K, the respective equilibrium solubility constant.

Dissolution rates and solubility data used in this study are listed in Table 3. These were taken from dissolution rate studies reported by Gíslason and Oelkers (2003), Palandri and Kharaka (2004), Olsen and Rimstidt (2008), and Gudbrandsson et al. (2014). The thermodynamic data for aqueous species and the minerals used to calculate the mineral solubilities were taken from by Phillips et al. (1988), Shock and Helgeson (1988), Cox et al. (1989), Shock et al. (1997), Arnórsson and Andrésdóttir (1999), Arnórsson and Stefánsson (1999), Gunnarsson and Arnórsson (2000), Stefánsson (2001), and Aradóttir et al. (2012).

The pore volume or porosity, ϕ, was calculated from the volume difference between the empty experimental reactor and the volume of the solid material in the reactor. The volume of solid was determined from the mass of material divided by its density.

The total surface area of the grains, A, was determined in two ways, first, by assuming spherical grains and homogeneous dissolution of the solid particles with time, and second, using the sugar lump model (Noiriel et al., 2009), where material is dissociated into smaller grains, which increased the surface area. In the spherical dissolution model, the surface area of the dissolving phases was calculated from the initial surface area, A_0, and the ratio of the initial number of moles of the solid, m_0, and the number of moles remaining, as a function of time, m_t, assuming the grains to be spherical, hence a factor of 2/3,

$$A = \varsigma_i A_0 \left(\frac{m_t}{m_0}\right)^{2/3} \quad (7)$$

In this model, total surface area does not increase with dissolution progress. However, in the sugar lump model, dissolution can generate extra surface initially and then decrease it,

$$A = \varsigma_i \left(A_0 + A_m \left(1 - \left(\frac{m_t}{m_0}\right)^{n_1}\right)^{n_2}\right)\left(\frac{m_t}{m_0}\right)^{n_3} \quad (8)$$

where A_m represents the maximum surface area, which is given by the sum of the surface area for all of the individual particles. $n_{1,2,3}$ are empirical coefficients that depend on the geometry of the aggregate. Coefficient n_3 is equal to 2/3, assuming spherical grains. In addition to the sugar lump model, the coefficient ς_i represents the fraction of reactive surface area of the solids. Its value can range from 0 to 1, where 0 represents the case where none of the surface is reactive and 1, where all of the surface reacts. Here, we have assumed ς_i to be 1 but the reactive surface area could be only a part of the total surface area (e.g., Brantley and Mellott, 2000; Colón et al., 2004; Aagaard and Helgeson, 1982; Helgeson et al., 1984), and it could vary greatly over long periods of water-rock interaction. This would cause dissolution rates to change significantly (e.g., Lichtner, 1996; White and Brantley, 2003; Luquot and Gouze, 2009; Noiriel et al., 2004).

3. Results

3.1. Solution composition

The chemical composition of the inlet and outlet solutions is presented in Table 4. The concentration of the inlet solution for all experiments was similar, between 8.44 and 8.68 mmol/kg HCl, pH of 2.10–2.11, and the concentration of other elements was below detection. The outflow solution pH was similar from all solid

Table 3
Thermodynamic and kinetic data used for the kinetic reaction path simulations. Kinetic constants were recalculated for geometric surface area.

Solid	Symbol	Simulation	Mineral compostion	Dissolution reaction	log $K_{25°C}$	log $k_{25°C}$ (mol/m^2/sec)	$r_{i\pm} = A_{geo}\, k\, (1\text{-}SI_i^n)$
Basaltic glass	BG	BG	$Na_{0.08}K_{0.008}Mg_{0.282}Ca_{0.263}Fe_{0.171}Al_{0.358}SiO_{3.297}$ [a]	$Na_{0.08}K_{0.008}Mg_{0.282}Ca_{0.263}Fe_{0.171}Al_{0.358}SiO_{3.297} + 1.162H^+ + 2.135H_2O = 0.081Na^+ + 0.008K^+ + 0.263Ca^{2+} + 0.282Mg^{2+} + 0.171Fe^{2+} + 0.358Al(OH)_4 + H_4SiO_4$	2.92[d]	[g] $8.557E-07(a_{H^+}^3/a_{Al}^1)^{1/3}$	$A\, k\, (1\text{-}SI)$
Crystalline basalt	Cpx	XB	$Ca_{0.415}Mg_{0.399}Fe_{0.209}Si_{0.9735}O_3$ [b]	$Ca_{0.415}Mg_{0.399}Fe_{0.209}Si_{0.9735}O_3 + 2.106H^+ + 0.894H_2O = 0.415Ca^{2+} + 0.399Mg^{2+} + 0.209Fe^{2+} + 0.9735H_4SiO_4$	10.05[e]	[h] –6.82	$A\, k_d\, a_{H^+}^{0.7}\, (1\text{-}SI)$
	Plag	XB	$Ca_{0.674}Na_{0.338}Al_{1.550}Si_{2.410}O_8$ [b]	$Na_{0.33}Ca_{0.674}Al_{1.55}Si_{2.410}O_8 + 7.864H_2O + 0.136\,H^+ = 0.33Na^+ + 0.67Ca^{2+} + 1.55Al(OH)_4^- + 2.416H_4SiO_4$	18.61[f]	[i] $10^{(0.33\ \log(a_{H^+}^1/a_{H_2O}^4)-12.46)}$ 10000	$A\, k\, (1\text{-}SI)$
	Fo	XB	$Mg_{1.68}Fe_{0.32}SiO_4$ [b]	$Mg_{1.68}Fe_{0.32}SiO_4 + 4H^+ = 1.68Mg^{2+} + 0.32Fe^{2+} + H_4SiO_4$	27.38[e]	[j] –7.54	$A\, k\, (1\text{-}SI)$
Forsterite	Fo93	FO	$Mg_{1.86}Fe_{0.14}SiO_4$ [c]	$Mg_{1.86}Fe_{0.14}SiO_4 + 4H^+ = 1.86Mg^{2+} + 0.14Fe^{2+} + H_4SiO_4$	28.43[e]	[j] –7.54	$A\, k\, (1\text{-}SI)$

[a] Oelkers and Gíslason (2001).
[b] Gudbrandsson et al. (2011).
[c] This study.
[d] Calculated using the approach of Techer et al. (2001) with dissolution equilibrium constants presented by Phillips et al. (1988) and Aradóttir et al. (2012).
[e] Stefánsson (2001).
[f] Arnórsson and Stefánsson (1999).
[g] From Gíslason and Oelkers (2003).
[h] Augite from Palandri and Kharaka (2004).
[i] Gudbrandsson et al. (2014).
[j] From Olsen and Rimstidt (2008).

Table 4
Chemical composition of the solutions sampled at the column outlet.

Exp. #	Time	Flow rate	pH/25 °C	Si	Na	K	Ca	Mg	Fe	Al	Cl
	Days	ml/min		mmol/kg	mmol/kg	mmol/kg	mmol/kg	mmol/kg	mmol/kg	mmol/kg	mmol/kg
Basaltic glass											
BG inlet			2.11	0.010	<0.04	<0.02	<0.001	<0.001	0.0006	0.002	8.44
BG 1 outlet	4	0.51	2.92	1.32	0.248	0.021	0.760	0.731	0.504	0.981	8.49
BG 2 outlet	6	0.5	2.85	1.33	0.239	0.020	0.734	0.705	0.502	0.940	8.48
BG 3 outlet	8	0.5	2.85	1.37	0.234	0.021	0.737	0.707	0.485	0.927	8.43
BG 4 outlet	10	0.53	2.73	1.39	0.220	0.028	0.685	0.663	0.461	0.864	8.49
BG 5 outlet	15	0.5	2.25	0.64	0.097	<0.02	0.241	0.257	0.193	0.314	8.60
BG 6 outlet	20	0.53	2.36	0.80	0.137	0.059	0.382	0.394	0.269	0.488	8.48
BG 7 outlet	22	0.48	2.52	1.09	0.201	<0.02	0.547	0.554	0.366	0.678	8.51
BG 8 outlet	25	0.48	2.66	1.35	0.208	<0.02	0.640	0.639	0.422	0.792	8.40
BG 9 outlet	29	0.48	2.62	1.38	0.199	0.020	0.622	0.625	0.417	0.795	8.56
Crystalline basalt											
XB inlet			2.10	0.020	<0.04	<0.02	<0.001	0.004	0.003	0.004	8.68
XB 1 outlet	1	0.47	2.24	0.438	0.047	<0.02	0.188	0.418	0.277	0.145	8.59
XB 2 outlet	3	0.44	2.33	0.814	0.049	<0.02	0.097	0.952	0.490	0.137	8.74
XB 3 outlet	6	0.44	2.34	0.804	0.047	<0.02	0.089	0.962	0.467	0.146	8.60
XB 4 outlet	9	0.44	2.32	0.706	0.1833	<0.02	0.091	0.820	0.392	0.165	8.54
XB 5 outlet	11	0.45	2.28	0.589	0.066	<0.02	0.093	0.628	0.303	0.182	8.42
XB 6 outlet	13	0.51	2.23	0.433	0.043	<0.02	0.086	0.456	0.213	0.176	8.56
XB 7 outlet	16	0.51	2.21	0.320	0.044	<0.02	0.086	0.306	0.133	0.186	8.43
XB 8 outlet	20	0.54	2.19	0.255	0.043	<0.02	0.089	0.213	0.075	0.193	8.38
XB 9 outlet	25	0.41	2.20	0.244	<0.04	<0.02	0.097	0.181	0.056	0.215	8.25
XB 10 outlet	28	0.45	2.18	0.205	<0.04	<0.02	0.090	0.139	0.041	0.199	8.37
XB 11 outlet	30	0.54	2.17	0.171	<0.04	<0.02	0.081	0.102	0.030	0.178	8.36
Forsterite											
FO inlet			2.10	0.006	<0.04	<0.02	<0.001	<0.001	0.0003	<0.001	8.68
FO 1 outlet	1	0.47	2.75	1.76	<0.04	<0.02	0.002	3.12	0.229	0.003	8.72
FO 2 outlet	3	0.47	2.64	1.69	<0.04	<0.02	0.001	2.87	0.210	0.002	8.74
FO 3 outlet	6	0.47	2.62	1.54	<0.04	<0.02	<0.001	2.77	0.197	0.002	8.62
FO 4 outlet	9	0.47	2.56	1.46	<0.04	<0.02	0.002	2.57	0.186	0.003	8.59
FO 5 outlet	11	0.46	2.86	1.69	<0.04	<0.02	<0.001	3.05	0.212	0.002	8.11
FO 6 outlet	13	0.53	2.54	1.35	<0.04	<0.02	<0.001	2.37	0.170	0.002	8.31
FO 7 outlet	16	0.51	2.48	1.25	<0.04	<0.02	<0.001	2.19	0.164	0.001	8.37
FO 8 outlet	20	0.54	2.52	1.35	<0.04	<0.02	<0.001	2.39	0.173	0.001	8.53
FO 9 outlet	28	0.42	2.56	1.44	<0.04	<0.02	<0.001	2.50	0.189	0.018	8.52
FO 10 outlet	30	0.40	2.60	1.50	<0.04	<0.02	<0.001	2.64	0.192	0.002	8.52
2σ [a]				0.01	0.05	0.01	0.001	0.0002	0.0003	0.0006	0.05

[a] Analytical uncertainity based on repeated analysis of the reference sample (GYG13).

materials: for basaltic glass, in the range of 2.25–2.92, for crystalline basalt, in the range of 2.17–2.30, and for forsterite, in the range of 2.48–2.86 (Fig. 4). For the output solutions from the crystalline basalt and forsterite experiments, the concentrations of the dissolved elements reached steady state within 10–15 days. For the basaltic glass, outflow solution concentration was relatively constant during the entire experiment.

The reaction stoichiometry can be studied by comparing element ratios in the solutions with those in the bulk solid. For basaltic glass dissolution, the element mole ratios in the outlet solutions after 10 days were Si/Mg = 2.15 ± 0.19, Si/Ca = 2.19 ± 0.25 and Mg/Ca = 0.99 ± 0.03. The corresponding ratios for the initial basaltic glass were 3.55, 3.80 and 0.93, suggesting non-stoichiometric dissolution under acid conditions with respect to Ca and Mg relative to Si. The element ratio in the outlet solution for forsterite was Si/Mg = 0.57 ± 0.01, close to the corresponding mineral ratio, 0.54, indicating stoichiometric dissolution of forsterite. For crystalline basalt, the elemental ratios in the outlet solutions were Si/Mg = 1.35 ± 0.24, Si/Ca = 2.70 ± 0.64 and Mg/Ca = 2.13 ± 0.91, compared with the corresponding bulk crystalline basalt ratios, 3.62, 3.47 and 1.01, respectively, indicating non-stoichiometric dissolution.

3.2. Solid product

The changes in solid surface properties, as a function of distance within the column and time, are shown in Fig. 5. Two features were observed. First, with increasing reaction time, dissolution features became progressively more obvious. This applied for all of the solids. Particle edges were covered by etch pits up to ~20 μm in diameter, which intercepted in some cases and formed corrosion troughs up to ~100 μm in length. Some amorphous basaltic glass grains developed networks of interconnected fractures all over their surfaces, forming flakes (~10–30 μm wide). Such features are caused by preferential dissolution along weaker planes or areas of the glass particles: effects of grain drying and spalling of an altered layer that precipitated on the surface (Gíslason and Oelkers, 2003). Second, dissolution features were unevenly distributed in the column. Deeper etch pits and more extensive dissolution channeling were observed near the inlet of the column than near the outlet. For glass, the powder on inlet side, within the first 1 cm, even lost its black color and appeared mostly white. This indicated extensive dissolution at the inlet, where fresh solution came into contact with the solid. This was accompanied by a slight increase in pH through the rest of the column and slower dissolution toward the outlet.

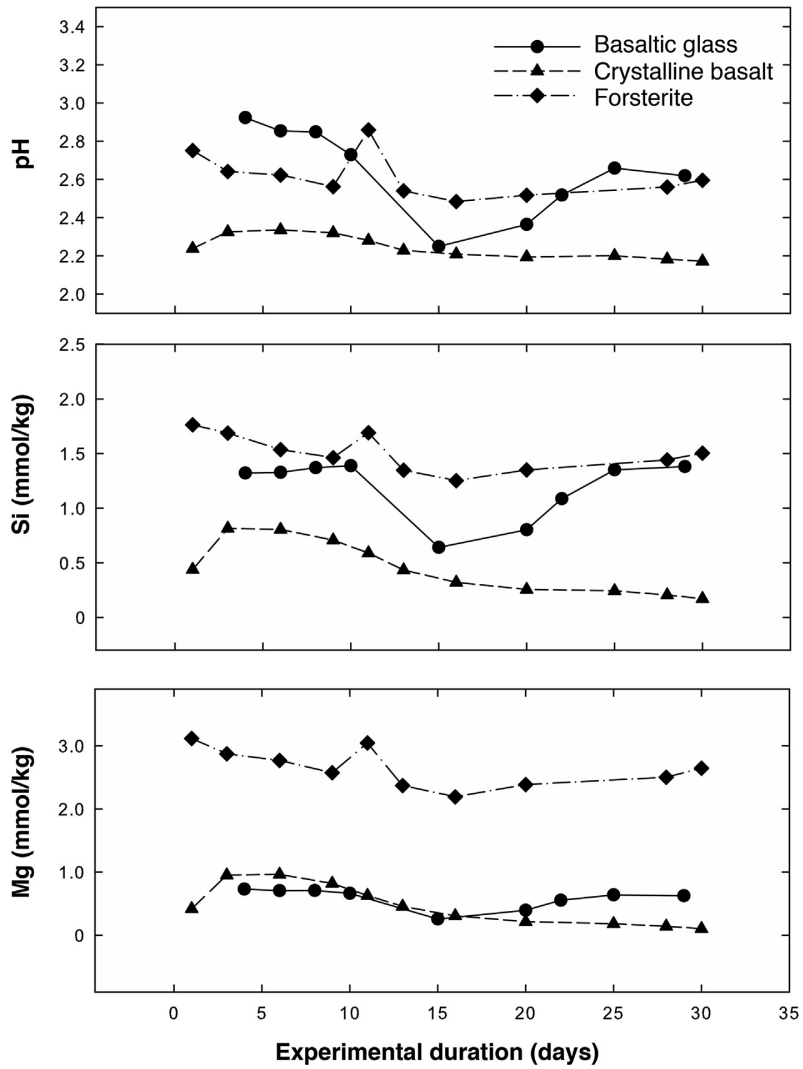

Fig. 4. The composition (pH, Si and Mg) in the outlet solution as a function of time.

3.3. X-ray microtomography

The results derived from X-ray microtomography, i.e. grain size, porosity, ϕ, and surface area, A, for the initial and the reacted material as a function of experiment duration are listed in Table 5.

The grain size distributions for the fresh and reacted material are shown in Fig. 6. There are two characteristic features. First, there was a considerable range in grain size for all of the solids. Although we used the sieved portion that was between 125 and 250 μm, the actual particles ranged from ~50 to ~200 μm, with initial distribution skewed towards the smaller grain size. Second, the median grain size decreased with increasing experiment duration for amorphous and crystalline basalt at the inlet side of the flow-through reactors but increased for forsterite. For basaltic glass, the median value for grain size decreased in the inlet of the reactor, from 103 (±39) μm to 79 (±40) μm after 4 weeks, while the outlet grain size remained relatively constant at 103–97 (±39–37) μm for the first two weeks, followed by a decrease to 77 (±32) μm at the end of the experiment. The trend for crystalline basalt was similar, with a decrease in the inlet grain size from 96 to 90 (±31–33) μm in 4 weeks, whereas the outlet grain size decreased from 96 to 88 (±31) μm throughout the experiment. For forsterite, the grain size did not change significantly at 2 weeks from 71 (±31) to 77 (±32–34) μm, either at the inlet and or the outlet, but at 4 weeks was 80 (±33) μm at the inlet and 64 (±27) μm at the outlet.

The specific surface area of all solids increased during the experiments. These changes were minor for forsterite and crystalline basalts (~7–13% ±5–6 increase in 4 weeks), whereas the specific surface area of basaltic glass changed considerably (up to 43% ± 5 in 4 weeks).

A similar trend was observed for porosity. It increased with experiment duration for all solids. For crystalline basalt and forsterite, these changes were minor, up to 6% ±5–6 increase, whereas the porosity for basaltic glass changed considerably, up to an

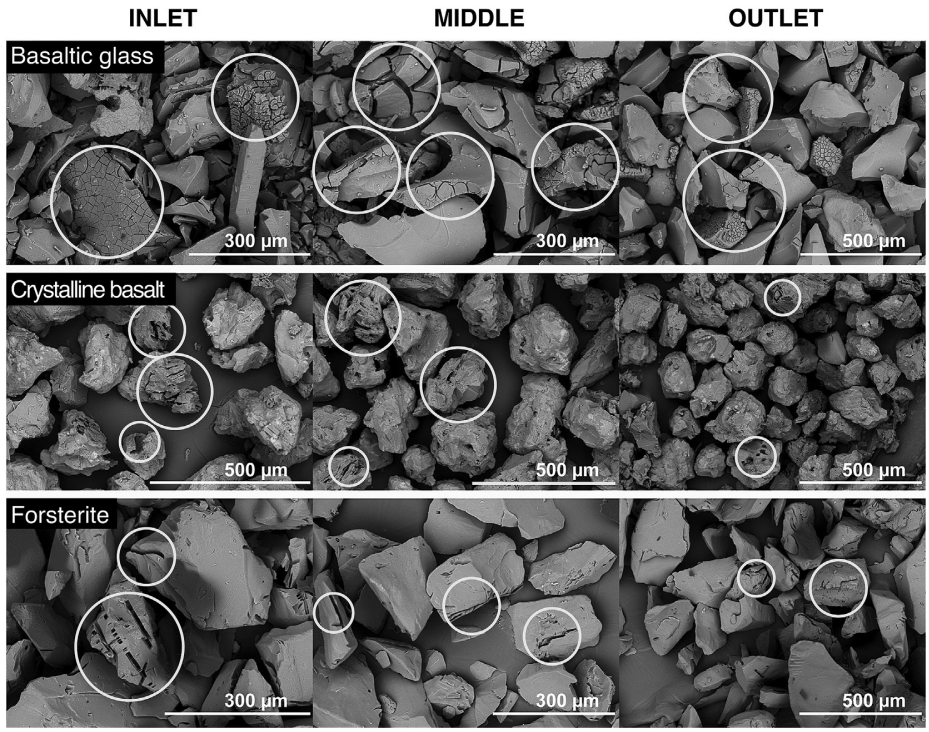

Fig. 5. SEM images of the solids after 4 weeks of reaction from the inlet, middle and outlet of the flow-through reactors. Etch pits and fractures on the reacted material were probably caused by preferential dissolution on weak areas or along weaker planes. Dissolution features are more dominant near the inlet, which indicates more extensive dissolution, where the pH of the fresh solution is lower. During passage through the column, reaction increases pH and the dissolution rate decreases toward the outlet.

Table 5
The measured porosity, ϕ, and surface area, A, determined using X-ray microtomography, XMT.

Exp. #	Time Days	Grain size median µm	ϕ_{XMT} %	A_{XMT} m^2/g
Basaltic glass				
BG inital	0	103	50	0.012
BG 5 inlet	15	78	83	0.020
BG 5 outlet	15	97	46	0.013
BG 9 inlet	29	79	86	0.021
BG 9 outlet	29	77	52	0.018
Crystalline basalt				
XB inital	0	96	52	0.013
XB 6 inlet	13	92	56	0.014
XB 6 outlet	13	92	53	0.013
XB 11 inlet	30	58	58	0.014
XB 11 outlet	30	88	56	0.015
Forsterite				
FO initial	0	71	42	0.014
FO 7 inlet	16	77	43	0.013
FO 7 outlet	16	77	44	0.013
FO 10 inlet	30	80	44	0.013
FO 10 outlet	30	64	46	0.015

Cumulative error is estimated to be ±5% for BG, XB and ±6% for FO.

increase of ~42% ± 5. The change in porosity was not evenly distributed within the reaction column. For all solid types, the difference was greater near the inlet. Porosity increased as grain size decreased and specific surface area increased, in all cases.

These observations demonstrate that dissolution along a flow path resulted in progressive changes in grain size, which led to changes in surface area and pore volume. These changes were dependent on the type of solid.

4. Discussion

4.1. Dissolution rates

The forward dissolution rates were calculated from the difference in solution composition at the inlet and the outlet side of the flow-through reactor, the flow rate and surface area of the solids (Eqn. (2)). The resulting rates with respect to Si and Mg are listed in Table 6 and shown in Fig. 7. For forsterite, the calculated dissolution rates derived from geometric surface area are systematically lower than those calculated from the surface area derived from X-ray microtomography images. The difference was ~0.3 log $mol/m^2/s$ units. Dissolution rates determined from Si and Mg were equivalent to those previously reported by Olsen and Rimstidt (2008) at the same pH and temperature. The Si rates obtained in this study are comparable to those reported by Rimstidt et al. (2012) from a compilation of available literature data but somewhat lower than the rates reported by Oelkers (2001), Golubev et al. (2005) and Pokrovsky and Schott (2000) (Table 7). Rimstidt et al. (2012) concluded that there was a negligible difference, within uncertainty, whether the forsterite dissolution rate was normalized to BET or the geometric surface area. As observed here, the calculated geometric surface area of forsterite was systematically greater (0.46 m^2) than that obtained from X-ray microtomography images and integrated over the entire flow-through reaction vessel (0.24–0.19 m^2). Using a fixed geometric surface for the calculations

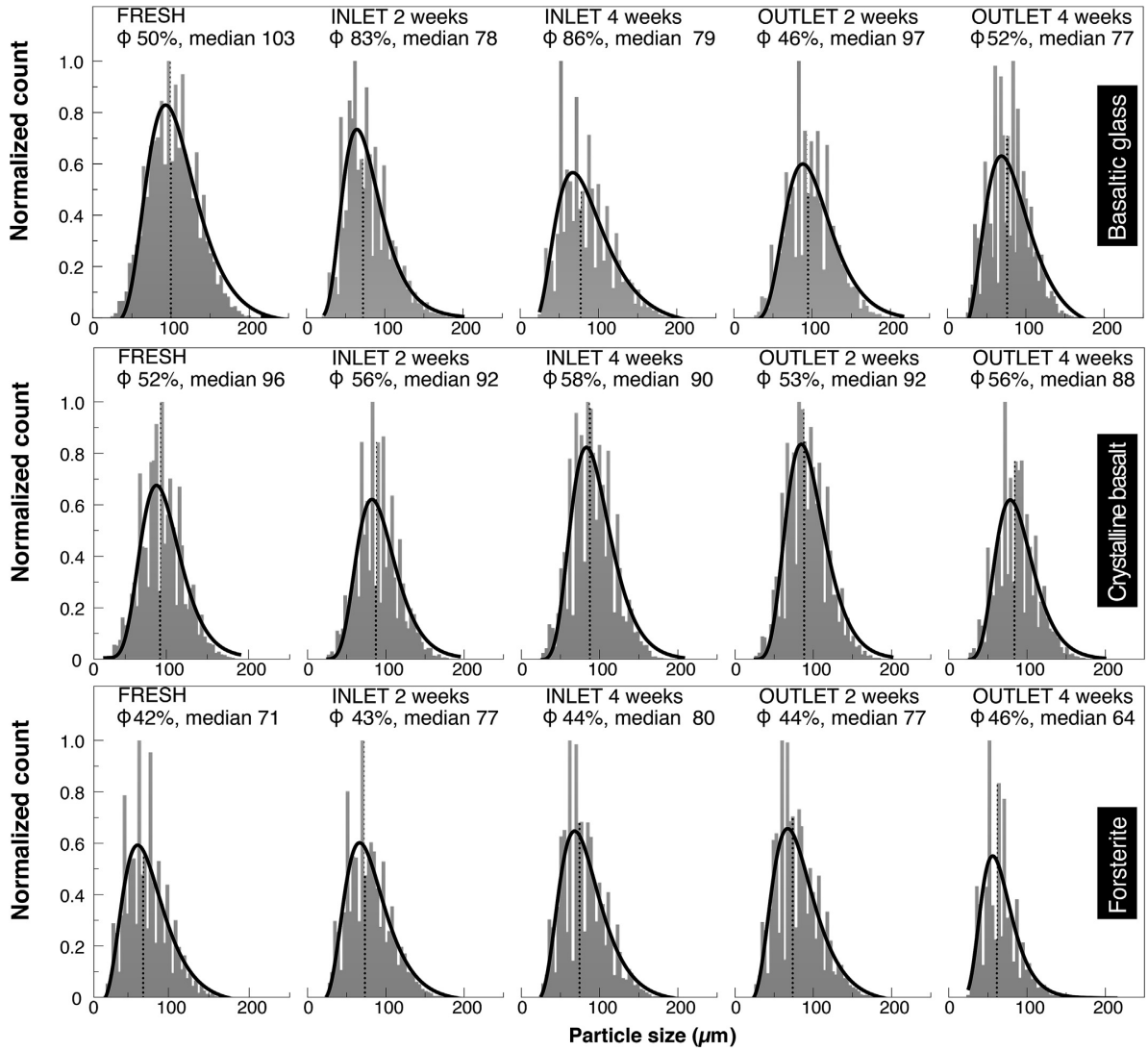

Fig. 6. Grain size distribution (lognormal) evolution as a function of time and distance in the reactor, determined from the 3D X-ray microtomography images. Porosity, ϕ, and median grain size are included.

resulted in lower reaction rates (log $r_{+,Si} = -7.52$ to -7.66 mol/m^2/s) whereas using the surface area obtained from the X-ray microtomography 3D images, which took into account the progressive decrease in forsterite surface, resulted in similar rates throughout the experiment (log $r_{+,Si} = -7.28$ to -7.24 mol/m^2/s).

For basaltic glass and crystalline basalt, the results were similar to forsterite. The rates determined from the geometric surface area were systematically lower than those determined from the X-ray microtomography measurements. Both the geometric and tomographic normalized rates obtained in this study compare well with those previously reported for crystalline basalt (Gudbrandsson et al., 2011) but the rate for basaltic glass was an order of magnitude lower than those reported by Gíslason and Oelkers (2003) (Table 7). The most probable reason was the different experimental setup, which resulted in a wide solute gradient with steeply increasing pH along our reaction pathway, which slowed the dissolution rate. The difference in surface area derived from the X-ray microtomography data was higher for basaltic glass and forsterite than for crystalline basalt, however the dissolution rate of crystalline basalt changed more during the experiment despite the changes in surface area.

From our results, we interpret that bulk dissolution rates for mafic minerals and rocks are relatively insensitive to change in the total surface area during progressive water-rock interaction. Dissolution of forsterite, basaltic glass and crystalline basalt all resulted in consumption of H^+ (acid) (reactions listed in Table 3), causing increased pH and decreased dissolution rates along the flow path. According to the geochemical model calculations, this was indeed to be expected, i.e. with increasing distance into the reactor, pH increases and dissolution rate decreases (Fig. 8). The

Table 6
The calculated rates of experimental dissolution using Si and Mg concentrations. The dissolution rates are normalized to geometric initial surface and tomographic surface. A_{XMT} tot = averaged surface area of tomographic measurements as a function of column distance, x, residual grams in the column (obtained from mass balance of outlet concentration).

Exp. #	Time days	A_{geo} tot m^2	A_{XMT} tot m^2	Dissolution rate, log $r_{+,i}$ (mol/m^2/s)			
				Si_{geo}	Si_{XMT}	Mg_{geo}	Mg_{XMT}
Basaltic glass							
BG 1 outlet	4	0.41	0.153	−7.57	−7.14	−7.27	−6.84
BG 2 outlet	6	0.41		−7.57		−7.30	
BG 3 outlet	8	0.41		−7.56		−7.30	
BG 4 outlet	10	0.41		−7.53		−7.30	
BG 5 outlet	15	0.41	0.144	−7.89	−7.44	−7.74	−7.28
BG 6 outlet	20	0.41		−7.77		−7.53	
BG 7 outlet	22	0.41		−7.68		−7.42	
BG 8 outlet	25	0.41		−7.59		−7.36	
BG 9 outlet	29	0.41	0.162	−7.58	−7.17	−7.37	−6.91
Average				−7.64 ± 0.12	−7.25 ± 0.22	−7.40 ± 0.15	−7.01 ± 0.25
Crystalline basalt							
XB 1 outlet	1	0.39	0.173	−8.07	−7.72	−7.36	−7.00
XB 2 outlet	3	0.39		−7.82		−7.02	
XB 3 outlet	6	0.39		−7.83		−7.02	
XB 4 outlet	9	0.39		−7.89		−7.09	
XB 5 outlet	11	0.39		−7.96		−7.20	
XB 6 outlet	13	0.39	0.166	−8.04	−7.68	−7.28	−6.91
XB 7 outlet	16	0.39		−8.18		−7.46	
XB 8 outlet	20	0.39		−8.26		−7.59	
XB 9 outlet	25	0.39		−8.40		−7.78	
XB 10 outlet	28	0.39		−8.45		−7.86	
XB 11 outlet	30	0.39	0.173	−8.45	−8.1	−7.91	−7.56
Average				−8.12 ± 0.24	−7.83 ± 0.23	−7.42 ± 0.33	−7.16 ± 0.35
Forsterite							
FO 1 outlet	1	0.46	0.238	−7.52	−7.24	−7.54	−7.26
FO 2 outlet	3	0.46		−7.54		−7.58	
FO 3 outlet	6	0.46		−7.58		−7.60	
FO 4 outlet	9	0.46		−7.61		−7.63	
FO 5 outlet	11	0.46		−7.55		−7.56	
FO 6 outlet	13	0.46		−7.58		−7.61	
FO 7 outlet	16	0.46	0.201	−7.63	−7.28	−7.66	−7.30
FO 8 outlet	20	0.46		−7.57		−7.60	
FO 9 outlet	28	0.46		−7.66		−7.69	
FO 10 outlet	30	0.46	0.186	−7.66	−7.27	−7.69	−7.30
Average				−7.59 ± 0.05	−7.26 ± 0.02	−7.62 ± 0.05	−7.29 ± 0.02

geometric dissolution rate from the inlet side of the reactor matched well with the results of Gíslason and Oelkers (2003). Increase of pH and decreasing rates in flow-through systems have been presented previously (Molins et al., 2014). The pH change from the inlet to the outlet of the column resulted in a corresponding dissolution decrease of 0.4–0.6 log units for the three solids studied. This was at a similar order and greater than the changes in the dissolution rate that resulted from changes in surface area at the inlet and outlet of the reactor and with time. It is therefore clear that small changes and heterogeneity in solution composition, including pH, can cause considerable effects on dissolution and the rate of elemental leaching.

4.2. Porosity and surface area change during progressive dissolution

During progressive mineral and rock dissolution, the porosity and surface area can change. In its simplest form, when only mineral dissolution occurs, mass decreases and pore volume increases. The specific surface area for individual grains increases due to reduction in grain size; the overall specific surface area of the material may change differently as small particles may also dissolve to completion, leaving a residue with, on average, larger particles. In more complex cases, progressive water-rock interaction dissolves primary solid phases and forms secondary phases. This can result in solid volume increase if the mole volume of the secondary phases is greater than the mole volume of the primary phases initially. An example is calcium carbonate precipitation experiments in cylindrical plug flow column reactors filled with calcite seed and glass beads (Noiriel et al., 2012, 2015). As a result, porosity can decrease in the rock matrix because of progressive water-rock interaction. In this work, we focused on the simpler case, dissolution only.

The changes in porosity were determined for the inlet and outlet sides of the flow-through reactor column using in situ XMT images. Progressive mineral and rock dissolution caused porosity in the columns to increase. Changes were greatest for basaltic glass, followed by crystalline basalt and forsterite (Fig. 9). Preferential dissolution was observed on the inlet side of the flow-through reactor. This trend was consistent with predictions from the reactive transport modeling, with dissolution of basaltic glass leading to pore volume increase from 50 to 90% on the inlet side but only 60% at the outlet side after 4 weeks of dissolution. These differences within the flow-through reactor system resulted from the pH dependence of the mineral and rock dissolution rates on progressive consumption of H^+ from the solution, increasing the pH and slowing the dissolution rate (Fig. 8). The average final porosity derived from the modeling matched well with the averaged XMT porosity for the glass (4% difference) and crystalline basalt (3% difference) but for olivine, the difference derived from solution composition was 27% higher. The reason for these differences was a different solid mass used for different experiments and the olivine

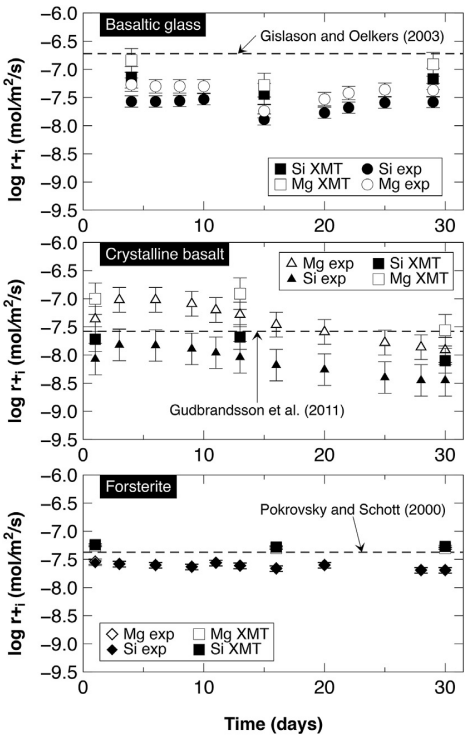

Fig. 7. Dissolution rates based on Si and Mg solution concentration as a function of time. The rates have been normalized to bulk geometric surface area (exp) or to the surface area derived from the X-ray microtomography images (XMT). The lines represent geometric normalized Si rates from the literature, recalculated for pH averaged from the experiments.

was finer grained than the basaltic glass or the crystalline basalt. The finest material dissolved first and its loss had no major impact on porosity (Fig. 9). The columns containing crystalline basalt and amorphous glass had similar initial porosity and grain size. The glass dissolved faster and its porosity changed heterogeneously compared with the less reactive crystalline basalt, which dissolved more homogeneously, as predicted by the spherical and sugar cube dissolution modeling.

Progressive mineral and rock dissolution decreases grain size and this was observed by XMT and geochemical modeling. Surface area increased as water-rock interaction progressed. The changes were reasonably modeled by the reactive transport simulations, particularly in the case of basaltic glass, but less successfully for forsterite and crystalline basalt (Fig. 10). Very little difference resulted from the method used for calculating surface area, i.e. the sugar lump or the spherical loss approach.

4.3. Do geochemical model calculations predict reactive transport behavior in porous media?

Reactive transport models are used to understand: the composition of natural waters; acidic water generation and leaching of metals from mine wastes; the origin of mineral deposits; the formation and dissolution of rocks and minerals in geologic formations in response to re-injection of industrial wastes, steam, CO_2 and H_2S; and to predict contaminant plume migration such as radionuclides in waste repositories, biodegradation of chemicals in landfills, and other contaminants (e.g., Steefel et al., 2005).

Comparison of the results from the reactive transport modeling and the experimental observations for solution composition, porosity, and surface area evolution for mineral and rock dissolution in a flowing system revealed some important aspects in the capabilities and limitations of commonly applied reactive transport modeling. First, some of the studied minerals and rocks were not observed to dissolve stoichiometrically. Non-stoichiometric dissolution of minerals and solids is usually not taken into account in geochemical modeling. However, such a modeling approach is possible by redefining individual elemental leaching rates along the flow-path and time rather than bulk mineral or solid dissolution rate. Second, fluid dynamics and preferential flow are commonly ignored in simple reactive transport modeling. This however affects the pore fluid composition and in turn the dissolution rates and changes in pore volume and surface area with time. Faster refill rate of the solution and/or a higher water/rock ratio would enhance the dissolution and porosity generation. However, the capacity of the model to infer the dissolution dynamics at larger field scales is not affected when the same macroscopic approach is applied to define input parameters as presented here in the models. Moreover, the systems under study were the simplest cases: dissolution far from equilibrium. For systems at close-to-equilibrium, other complications can be introduced like nucleation and growth of secondary phases; flow path heterogeneity favouring non-uniform precipitation patterns; and geometry of porous network and in turn

Table 7
Comparision of dissolution rates obtained in this study and reported in the literature.

Solid	pH/25 °C	Surface area	log $r_{+,Si}$ mol/m^2/s	Reference
Basaltic glass	2.25–2.92	geo	−7.64 ± 0.12	This study
	2.25–2.92	XMT	−7.25 ± 0.22	This study
	2.50	geo	−6.34[a]	Gíslason and Oelkers (2003)
Crystalline basalt	2.19–2.34	geo	−8.12 ± 0.24	This study
	2.19–2.34	XMT	−7.83 ± 0.23	This study
	2.30	geo	−7.64[a,b]	Gudbrandsson et al. (2011)
Forsterite	2.48–2.86	geo	−7.59 ± 0.05	This study
Forsterite	2.48–2.86	XMT	−7.26 ± 0.02	This study
Forsterite	2.62	geo	−7.66	Olsen and Rimstidt (2008)
Forsterite	2.00	geo	−6.97[a]	Oelkers (2001)
Forsterite	3.05	geo	−7.58 [a]	Golubev et al. (2005)
Forsterite	2.50	geo	−7.46	Rimstidt et al. (2012)
Forsterite	2.70	geo	−7.23[a]	Pokrovsky and Schott (2000)

[a] Converted to geo from BET surface area.
[b] Extrapolated.

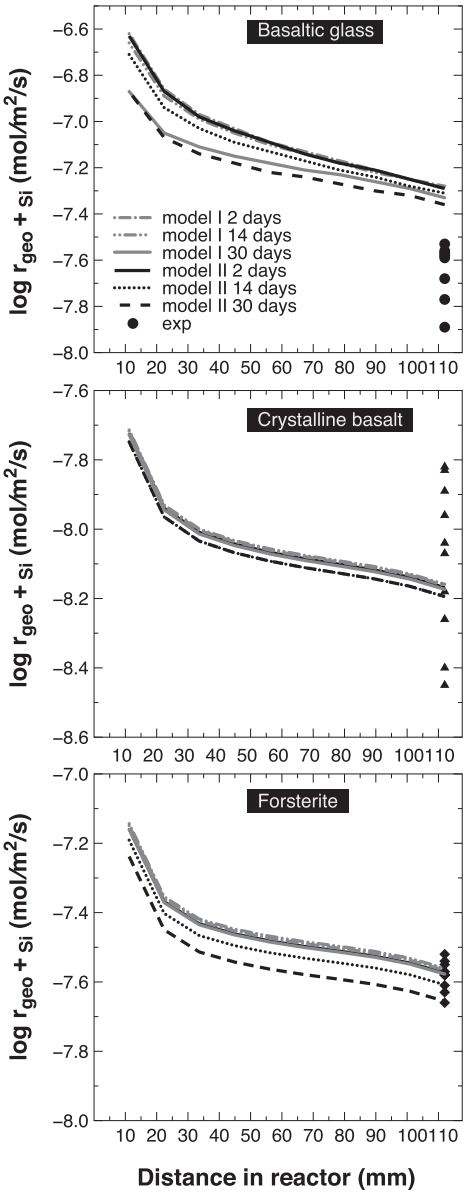

Fig. 8. Dissolution rates derived from the reactive transport modeling as a function of distance through the reactor. Model I used the sugar lump approach to estimate change in surface area (gray) and Model II assumed spherical particles with homogeneous loss (black).

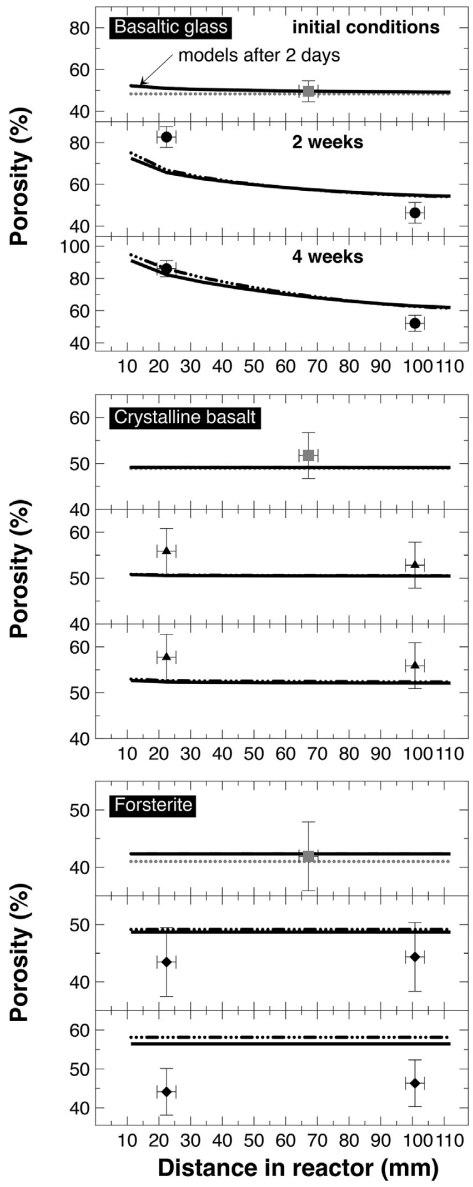

Fig. 9. Experiment (symbols) and model derived (lines) porosity as a function of distance at initial conditions (gray square and gray line marked), 2 and 4 weeks of interaction. The model that used simple spherical dissolution is the solid line, the model that used sugar lump dissolution is shown as a dashed black line.

closure of flow paths with time (Noiriel et al., 2015; Peuble et al., 2015). Third, similar results were obtained for mineral surface area and surface area normalized dissolution rates independent of the method applied in the calculations, i.e. whether geometric or tomographic normalized surface area was used for calculating solid dissolution rates or whether the simple spherical model or the more complicated sugar lump model was used. Fourth, the dissolution rates obtained from a complex flow-through system were observed to be comparable to those obtained from mixed flow reactor experiments at far from equilibrium. However, observed differences in our results arose from changes in the properties of the solid and solution along the flow path and as a function of time, such as surface area heterogeneity and pH variations. Such variations must be included in computations to be able to compare the two systems. Fifth, the calculated porosity and surface area changes along flow-path and time were observed to represent similar trends as those measured, however, accurate values are difficult to predict. This points towards the problem of the predicting capabilities of reactive transport modeling, i.e. calculations of pore

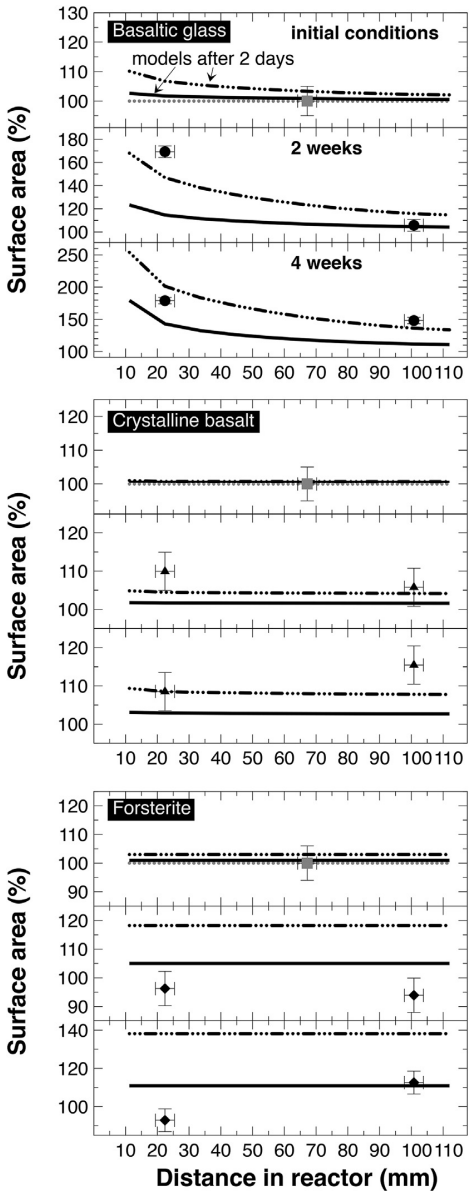

Fig. 10. Experiment (symbols) and model derived (lines) specific surface area as a function of distance at initial conditions (gray square and gray line marked), 2 and 4 weeks of interaction converted to $\% = \frac{surface\ at\ time}{initial\ surface} * 100$. The model with simple spherical dissolution is represented with a full line; the model that uses sugar lump dissolution is shown as a dashed black line.

volume and mineral and rock surface area changes with time and along flow paths that in turn are key parameters in determining dissolution rates, overall chemical mass movement in the system, and fluid flow paths and velocities.

5. Conclusions

Mineral and rock dissolution was studied experimentally using flow-through reactors and reactive transport modeling. The studied rocks and minerals were forsterite and crystalline and amorphous basalt, dissolved in HCl solutions at pH ~2.5. Solution composition, particle surface area, and porosity were determined as a function of reaction time and travel distance within the reactor, using in situ X-ray computed tomography (XMT) and chemical composition of the inlet and outlet solutions. Comparison of the results from the modeling and experiments demonstrate some important points.

(1) The dissolution rates far from equilibrium obtained here using a complex flow-through system were observed to be comparable to those obtained from mixed flow reactor experiments. The rates, normalized to the initial geometric surface area, were: log $r_{+,Si}$ −7.59 ± 0.05 for forsterite, −7.64 ± 0.12 for basaltic glass and −8.12 ± 0.24 (mol/m^2/s) for crystalline basalt, at 25 °C and pH ~2.5.
(2) Some of the minerals and rocks were not observed to dissolve stoichiometrically; such non-stoichiometric dissolution of minerals and solids is commonly not taken into account in reactive transport modeling.
(3) Similar results were obtained independent of the method applied in the calculations for mineral surface area and surface area normalized dissolution rates, i.e. whether geometric or tomographic normalized surface area was used or whether the simple spherical model or more complicated sugar lump model implemented.
(4) Mineral and rock dissolution resulted in increased porosity and specific surface area of the solids; these changes were not uniformly distributed along the fluid flow path or with time. Similar trends were predicted by reactive transport modeling, however, true values were difficult to predict. It follows that accurate prediction capabilities of simple reactive transport modeling may be limited for calculating pore volume and mineral and rock surface area changes with time and along flow paths that in turn are key parameters in determining dissolution rates, overall chemical mass movement in the system, and fluid flow paths and velocities.

Acknowledgements

We thank Gissur Örlygsson, Nicole Keller, Matthijs A. Smith, Snorri Guðbrandsson and Prathap Moola for analytical and experimental assistance. We also thank two anonymous reviewers for providing insightful reviews on the original manuscript and Michael Kersten for editorial handling. This research was made possible by a Marie Curie grant from the European Commission in the 7th Framework, as the MINSC ITN (Initial Training Research Network) Project Number 290040, and Landsvirkjun grant DOK-08-2016 to J. Přikryl.

References

Aagaard, P., Helgeson, H.C., 1982. Thermodynamic and kinetic constraints on reaction rates among minerals and aqueous solutions: I. Theoretical considerations. Am. J. Sci. 282, 237–285.
Akcil, A., Koldas, S., 2006. Acid mine drainage (AMD): causes, treatment and case studies. J. Clean. Prod. 14, 1139–1145.
Appelo, C.A.J., Postma, D., 2005. Geochemistry, Groundwater and Pollution. CRC Press.
Aradóttir, E.S.P., Sonnenthal, E.L., Jónsson, H., 2012. Development and evaluation of a thermodynamic dataset for phases of interest in CO_2 mineral sequestration in basaltic rocks. Chem. Geol. 304, 26–38.
Aradóttir, E.S.P., Sigfússon, B., Sonnenthal, E.L., Björnsson, G., Jónsson, H., 2013. Dynamics of basaltic glass dissolution–Capturing microscopic effects in continuum scale models. Geochim. Cosmochim. Acta. 121, 311–327.
Arnórsson, S., Andrésdóttir, A., 1999. The Dissociation Constants of Al-hydroxy Complexes at 0–350°C and Psat. Geochemistry of the Earth's Surface, Balkema, Rotterdam, pp. 425–428.
Arnórsson, S., Stefánsson, A., 1999. Assessment of feldspar solubility constants in water in the range 0° to 350°C at vapor saturation pressures. Am. J. Sci. 299,

173–209.
Brantley, S.L., Kubicki, J.D., White, A.F., 2008. Kinetics of Water-rock Interaction. Springer, New York.
Brantley, S.L., Mellott, N.P., 2000. Surface area and porosity of primary silicate minerals. Am. Mineral. 85, 1767–1783.
Brueckner, H.K., Carswell, D.A., Griffin, W.L., Medaris, L.G., Van Roermund, H.L.M., Cuthbert, S.J., 2010. The mantle and crustal evolution of two garnet peridotite suites from the Western Gneiss Region, Norwegian Caledonides: an isotopic investigation. Lithos 117, 1–19.
Cnudde, V., Boone, M.N., 2013. High-resolution X-ray computed tomography in geosciences: a review of the current technology and applications. Earth-Sci. Rev. 123, 1–17.
Colón, C.F.J., Oelkers, E.H., Schott, J., 2004. Experimental investigation of the effect of dissolution on sandstone permeability, porosity, and reactive surface area. Geochim. Cosmochim. Acta. 68, 805–817.
Cox, J.D., Wagman, D.D., Medvedev, V.A., 1989. CODATA Key Values for Thermodynamics. Hemisphere Publication Corp.
Galeczka, I., Wolff-Boenisch, D., Oelkers, E.H., Gíslason, S.R., 2014. An experimental study of basaltic glass–H_2O–CO_2 interaction at 22 and 50°C: implications for subsurface storage of CO_2. Geochim. Cosmochim. Acta. 126, 123–145.
Gandy, C.J., Smith, J.W.N., Jarvis, A.P., 2007. Attenuation of mining-derived pollutants in the hyporheic zone: a review. Sci. Total Environ. 373, 435–446.
Giammar, D.E., Bruant, R.G., Peters, C.A., 2005. Forsterite dissolution and magnesite precipitation at conditions relevant for deep saline aquifer storage and sequestration of carbon dioxide. Chem. Geol. 217, 257–276.
Gíslason, S.R., Oelkers, E.H., 2003. Mechanism, rates, and consequences of basaltic glass dissolution: II. An experimental study of the dissolution rates of basaltic glass as a function of pH and temperature. Geochim. Cosmochim. Acta. 67, 3817–3832.
Gíslason, S.R., Oelkers, E.H., 2014. Carbon storage in basalt. Science 344, 373–374.
Golubev, S.V., Pokrovsky, O.S., Schott, J., 2005. Experimental determination of the effect of dissolved CO_2 on the dissolution kinetics of Mg and Ca silicates at 25°C. Chem. Geol. 217 (3), 227–238.
Gouze, P., Luquot, L., 2011. X-ray microtomography characterization of porosity, permeability and reactive surface changes during dissolution. J. Contam. Hydrol. 120–121, 45–55.
Gudbrandsson, S., Wolff-Boenisch, D., Gíslason, S.R., Oelkers, E.H., 2011. An experimental study of crystalline basalt dissolution from $2 \leq$ pH ≤ 11 and temperatures from 5 to 75°C. Geochim. Cosmochim. Acta. 75, 5496–5509.
Gudbrandsson, S., Wolff-Boenisch, D., Gíslason, S.R., Oelkers, E.H., 2014. Experimental determination of plagioclase dissolution rates as a function of its composition and pH at 22°C. Geochim. Cosmochim. Acta. 139, 154–172.
Gunnarsson, I., Arnórsson, S., 2000. Amorphous silica solubility and the thermodynamic properties of $H_4SiO^\circ_4$ in the range of 0° to 350°C at P_{sat}. Geochim. Cosmochim. Acta. 64, 2295–2307.
Gysi, A.P., Stefánsson, A., 2012a. CO_2-water–basalt interaction. Low temperature experiments and implications for CO_2 sequestration into basalts. Geochim. Cosmochim. Acta. 81, 129–152.
Gysi, A.P., Stefánsson, A., 2012b. Experiments and geochemical modeling of CO_2 sequestration during hydrothermal basalt alteration. Chem. Geol. 306–307, 10–28.
Gysi, A.P., Stefánsson, A., 2012c. Mineralogical aspects of CO_2 sequestration during hydrothermal basalt alteration — an experimental study at 75 to 250°C and elevated pCO_2. Chem. Geol. 306–307, 146–159.
Helgeson, H.C., Murphy, W.M., Aagaard, P., 1984. Thermodynamic and kinetic constraints on reaction rates among minerals and aqueous solutions. II. Rate constants, effective surface area, and the hydrolysis of feldspar. Geochim. Cosmochim. Acta. 48, 2405–2432.
Jha, D., Sørensen, H.O., Dobberschütz, S., Feidenhans'l, R., Stipp, S.L.S., 2014. Adaptive center determination for effective suppression of ring artifacts in tomography images. Appl. Phys. Lett. 105 (14), 143107–1-4.
Kieffer, B., Jové, C.F., Oelkers, E.H., Schott, J., 1999. An experimental study of the reactive surface area of the Fontainebleau sandstone as a function of porosity, permeability, and fluid flow rate. Geochim. Cosmochim. Acta. 63, 3525–3534.
Lichtner, P.C., 1996. Continuum formulation of multicomponent- multiphase reactive transport. Rev. Min. 34, 1–81.
Liu, X., Tanaka, M., Okutomi, M., 2013. Single-image noise level estimation for blind denoising. IEEE T. Image Process. 22 (12), 5226–5237.
Luquot, L., Gouze, P., 2009. Experimental determination of porosity and permeability changes induced by injection of CO_2 into carbonate rocks. Chem. Geol. 265, 148–159.
McGrail, B.P., Schaef, H.T., Ho, A.M., Chien, Y.J., Dooley, J.J., Davidson, C.L., 2006. Potential for carbon dioxide sequestration in flood basalts. J. Geophys. Res. 111.
Molins, S., Trebotich, D., Yang, L., Ajo-Franklin, J.B., Ligocki, T.J., Shen, C., Steefel, C.I., 2014. Pore-scale controls on calcite dissolution rates from flow-through laboratory and numerical experiments. Environ. Sci. Technol. 48, 7453–7460.
Nagy, K.L., Blum, A.E., Lasaga, A.C., 1991. Dissolution and precipitation kinetics of kaolinite at 80 degrees C and pH 3; the dependence on solution saturation state. Am. J. Sci. 291, 649–686.
Noiriel, C., Gouze, P., Bernard, D., 2004. Investigation of porosity and permeability effects from microstructure changes during limestone dissolution. Geophys. Res. Lett. 31.
Noiriel, C., Luquot, L., Madé, B., Raimbault, L., Gouze, P., van der Lee, J., 2009. Changes in reactive surface area during limestone dissolution: an experimental and modelling study. Chem. Geol. 265, 160–170.
Noiriel, C., Steefel, C.I., Yang, L., Ajo-Franklin, J., 2012. Upscaling calcium carbonate precipitation rates from pore to continuum scale. Chem. Geol. 318–319, 60–74.
Noiriel, C., 2015. Resolving time-dependent evolution of pore-scale structure, permeability and reactivity using x-ray microtomography. Rev. Min. Geochem. 80, 247–285.
Noiriel, C., Steefel, C.I., Yang, L., Bernard, D., 2015. Effects of pore-scale precipitation on permeability and flow. Adv. Water Resour. 95, 125–137.
Oelkers, E.H., 2001. An experimental study of forsterite dissolution rates as a function of temperature and aqueous Mg and Si concentrations. Chem. Geol. 175, 485–494.
Oelkers, E.H., Gíslason, S.R., 2001. The mechanism, rates and consequences of basaltic glass dissolution: I. An experimental study of the dissolution rates of basaltic glass as a function of aqueous Al, Si and oxalic acid concentration at 25°C and pH = 3 and 11. Geochim. Cosmochim. Acta. 65, 3671–3681.
Olsen, A.A., Rimstidt, J.D., 2008. Oxalate-promoted forsterite dissolution at low pH. Geochim. Cosmochim. Acta. 72, 1758–1766.
Otsu, N., 1979. Thresholds selection method form grey-level histograms. IEEE T. Syst. Man. Cyb. 9 (1), 62–66.
Palandri, J.L., Kharaka, Y.K., 2004. A Compilation of Rate Parameters of Water-mineral Interaction Kinetics for Application to Geochemical Modeling (No. Open-file-2004-1068). Geological Survey, Menlo Park CA.
Parkhurst, D.L., Appelo, C.A.J., 2013. Description of Input and Examples for PHREEQC Version 3—a Computer Program for Speciation, Batch-reaction, One-dimensional Transport, and Inverse Geochemical Calculations. U.S. Geological Survey Techniques and Methods, book 6.
Peuble, S., Godard, M., Luquot, L., Andreani, M., Martinez, I., Gouze, P., 2015. CO_2 geological storage in olivine rich basaltic aquifers: new insights from reactive-percolation experiments. Appl. Geochem. 52, 174–190.
Pokrovsky, O.S., Schott, J., 2000. Kinetics and mechanism of forsterite dissolution at 25°C and pH from 1 to 12. Geochim. Cosmochim. Acta. 64, 3313–3325.
Phillips, S.L., Hale, F.V., Silvester, L.F., Siegel, M.D., 1988. Thermodynamic Tables for Nuclear Waste Isolation: Vol. 1, Aqueous Solutions Database. Report LBL-22860, NUREG/CR-4864, SAND87–0323. Lawrence Berkeley Lab, Berkeley, CA, USA.
Rimstidt, J.D., Brantley, S.L., Olsen, A.A., 2012. Systematic review of forsterite dissolution rate data. Geochim. Cosmochim. Acta 99, 159–178.
Saldi, G.D., Jordan, G., Schott, J., Oelkers, E.H., 2009. Magnesite growth rates as a function of temperature and saturation state. Geochim. Cosmochim. Acta. 73, 5646–5657.
Shock, E.L., Helgeson, H.C., 1988. Calculation of the thermodynamic and transport properties of aqueous species at high temperatures and pressures: correlation algorithms for ionic species and equation of state predictions to 5kb and 1000°C. Geochim. Cosmochim. Acta. 52, 2009–2036.
Shock, E.L., Sassani, D.C., Willis, M., Sverjensky, D.A., 1997. Inorganic species in geologic fluids: correlations among standard molal thermodynamic properties of aqueous ions and hydroxide complexes. Geochim. Cosmochim. Acta. 61, 907–950.
Stefánsson, A., 2001. Dissolution of primary minerals of basalt in natural waters: I. Calculation of mineral solubilities from 0 C to 350 C. Chem. Geol. 172, 225–250.
Steefel, C.I., DePaolo, D.J., Lichtner, P.C., 2005. Reactive transport modeling: an essential tool and a new research approach for the Earth sciences. Earth Planet. Sci. Let. 240, 539–558.
Stockmann, G.J., Wolff-Boenisch, D., Gíslason, S.R., Oelkers, E.H., 2011. Do carbonate precipitates affect dissolution kinetics? 1: Basaltic glass. Chem. Geol. 284, 306–316.
Techer, I., Advocat, T., Lancelot, J., Liotard, J.M., 2001. Dissolution kinetics of basaltic glasses: control by solution chemistry and protective effect of the alteration film. Chem. Geol. 176, 235–263.
Tester, J.W., Worley, W.G., Robinson, B.A., Grigsby, C.O., Feerer, J.L., 1994. Correlating quartz dissolution kinetics in pure water from 25 to 625°C. Geochim. Cosmochim. Acta. 58, 2407–2420.
Tomasi, C., Manduchi, R., 1998, January. Bilateral filtering for gray and color images. In: Sixth International Conference on Computer Vision (IEEE Cat. No.98CH36271), Bombay, vol. 1998, pp. 839–846.
White, A.F., Brantley, S.L., 2003. The effect of time on the weathering of silicate minerals: why do weathering rates differ in the laboratory and field? Chem. Geol. 202, 479–506.

Appendix II

Appendix II

H_2S sequestration process and sustainability in geothermal systems

Jan Přikryl[1], Chiara Marieni[1,3], Snorri Gudbrandsson[1,2], Edda Sif Aradóttir[3], Ingvi Gunnarsson[3] and Andri Stefánsson[1]

[1]Institute of Earth Sciences, University of Iceland, Sturlugata 7, 101 Reykjavik, Iceland

[2]Reykjavík Geothermal, Sudurlandsbraut 18, 108 Reykjavík, Iceland

[3]Reykjavík Energy, Bæjarháls 1, 110 Reykjavík, Iceland

Geothermics, 2018

Highlights:

- H_2S injection into rocks is cheap and a sustainable abatement method.
- Optimal sequestration condition is 200-250 °C with fluid's acidic pH and H_2S 10-30 mmol/kg.
- Formation of Fe silicates is limiting factor in H_2S sequestration efficiency.

Keywords: Geothermal energy; Environment; Mitigations; H_2S emissions; H_2S abatement

Geothermics 71 (2018) 156–166

Contents lists available at ScienceDirect

Geothermics

journal homepage: www.elsevier.com/locate/geothermics

H_2S sequestration process and sustainability in geothermal systems

Jan Přikryl[a,*], Chiara Marieni[a,c], Snorri Gudbrandsson[a,b], Edda Sif Aradóttir[c], Ingvi Gunnarsson[c], Andri Stefánsson[a]

[a] Institute of Earth Sciences, University of Iceland, Sturlugata 7, 101 Reykjavik, Iceland
[b] Reykjavík Geothermal, Sudurlandsbraut 18, 108 Reykjavík, Iceland
[c] Reykjavík Energy, Bæjarháls 1, 110 Reykjavík, Iceland

ARTICLE INFO

Keywords:
Geothermal energy
Environment
Mitigation
H_2S emissions
H_2S abatement

ABSTRACT

Reduction of H_2S emissions from geothermal power plants is an important environmental, economic, and social challenge that needs to be addressed. The geochemistry associated with H_2S injection into a geothermal reservoir with a basaltic host rock followed by sulfide mineralization was investigated experimentally, and reactive transport modeling used to determine the geochemical feasibility of such H_2S sequestration. Re-injection of H_2S-rich fluids into geothermal systems resulted in the dissolution of basalt followed by the mineralization of the H_2S into pyrite and pyrrhotite. At a neutral pH of the injected solution the H_2S mineralization was observed to be slow and result in limited H_2S mineralization, whereas at acid pH the reaction rates are much faster, and up to ~62% of the injected H_2S mineralized. The rate of H_2S mineralization was observed to be limited by Fe leaching rates from basaltic glass, suggesting that the rock dissolution rate is the limiting factor of H_2S sequestration in geothermal systems. The long-term effects of H_2S-rich fluid re-injection into geothermal systems (> 100 years) apparently results in increased porosity close to the outlet of the injection well due to rock dissolution, whereas pyrite formation has only limited effects on the porosity of the entire system. The optimized conditions of H_2S sequestration are moderate H_2S concentrations of re-injection fluids (10–30 mmol/kg) with acid pH/25 °C ~2–3, and reaction temperatures of 200–250 °C. Higher H_2S concentrations result in a lower sequestration proportion due to the limited supply of Fe from the host rocks for sulfide precipitation. Higher temperatures result in the uptake of Fe by minerals other than pyrite, such as epidote, and also lower the proportion of sequestration. H_2S re-injection and sequestration in geothermal systems is thought to be a geochemically and economically feasible option, as the method is cheaper than commonly used procedures today.

1. Introduction

Hydrogen sulfide (H_2S) is among the major elements in geothermal fluids, with concentrations ranging from a few ppb to hundreds of ppm (e.g., Kaasalainen and Stefánsson, 2011; Stefánsson et al., 2015; Gunnarsson-Robin et al., 2017). Although geothermal energy generation is more environmentally friendly than many other energy sources like coal, oil and gas, geothermal power plants also contribute to atmospheric carbon dioxide (CO_2) and H_2S pollution (e.g., DiPippo, 2012). Odor can be detected even at very low concentrations or ~1 μg/m^3, and when exceeding 1500 μg/m^3 H_2S is considered toxic to humans, animals and vegetation (e.g., Koch and Erskine, 2001; Selene and Chou, 2003). Moreover, contact with atmospheric oxygen may cause the oxidation of H_2S to elemental sulfur (S), sulfur dioxide (SO_2), and sulfuric acid (H_2SO_4) and result in the formation of acid rain, which damages structures, buildings, agricultural crops, and other vegetation (e.g., Greaver et al., 2012; Likens et al., 1979). Over the last two decades, local (e.g. in Iceland, 5/14/2010) and international (World Health Organization, 2000) air quality regulations have been enacted to control the anthropogenic harmfulness, with the maximum atmospheric H_2S concentrations not allowed to exceed 50–150 μg/m^3 in 24 h, depending on location.

A method proposed to abate the H_2S emissions from geothermal power plants is re-injection into the geothermal reservoir followed by mineralization into sulfides (e.g. Stefánsson et al., 2011). Such re-injection is currently being tested at the Hellisheiði geothermal plant, SW Iceland, in a project named SulFix. A mixture of H_2S and CO_2 is injected together with condensed steam and waste water into the geothermal reservoir (Gunnarsson et al., 2013). The interaction between host basaltic rocks and gas-loaded water at temperatures above 230 °C is thought to result in the precipitation of H_2S as secondary minerals (Stefánsson et al., 2011). The minerals involved in the reactions may

* Corresponding author.
E-mail address: jap5@hi.is (J. Přikryl).

http://dx.doi.org/10.1016/j.geothermics.2017.09.010
Received 28 June 2017; Received in revised form 22 September 2017; Accepted 24 September 2017

include various sulfides such as pyrite and pyrrhotite as well as prehnite, epidote and magnetite (Stefánsson and Arnórsson, 2002; Stefánsson et al., 2015; Gunnarsson-Robin et al., 2017). However, the rates and mechanisms, possible changes in rock porosity upon sulfide mineralization and prolonged sustainability of H_2S re-injection into geothermal system are not well understood.

The aim of the present study is to assess the geochemical reactions associated with H_2S re-injection and mineralization in geothermal systems, in particular the reaction mechanisms, secondary minerals involved, the effects of pH, temperature, H_2S concentration on the rate of mineralization, and the long-term changes within the geothermal reservoir. In order to answer these questions, flow-through experiments were conducted on basalt in the form of glass reacted with an H_2S-rich solution under geothermal conditions (100–250 °C). Both solution chemistry and alteration mineralogy were analyzed. Furthermore, reactive transport modeling was carried out to further support the mechanisms for the reactions and forecast long-term geochemical effects on H_2S re-injection into geothermal systems.

2. Application of experiments and modeling to large-scale H_2S sequestration problems

Large-scale geothermal processes can be studied quickly and reliably using experiments and geochemical modeling. A combination of small-scale flow-through experiments and reactive transport numerical simulations in an open system, where fluid-rock interaction causes H_2S abatement, occurs as an analogue to a field scenario (Fig. 1). With such a method, we can sample and study changes in rock, physical properties, secondary minerals, solution composition and the sulfide precipitation process as a function of reaction distance, time or system conditions. This profoundly reduces any environmental hazard and investment risk and the findings can easily be enlarged for field scale applications.

3. Experimental details

3.1. Experimental solutions

The initial aqueous solutions were created following two different experimental series, A and B. In series A, two solutions were mixed inline prior to entering the flow-through reactor; one solution consisted of an H_2S-rich solution made from Na_2S (Sigma-Aldrich®, > 99.99%) and deionized water with a pH of ~12, whereas the other solution was a ~0.01 M HCl solution (Sigma-Aldrich®) of a pH of ~2. The desired pH of the mixed inlet fluid was reached by adjusting the flow rates of the two solutions. In series B, a single inlet solution was prepared by dissolving Na_2S in degassed deionized water followed by adjustment of the pH using 0.01 M HCl (Sigma) to a value of ~7. For series B, the ionic strength of the solutions was adjusted using NaCl (Sigma-Aldrich®, > 99%). For both experimental series A and B, the concentrations of all the inlet solutions were undersaturated with respect to sulfide minerals, including pyrite and pyrrhotite. The composition of the initial aqueous solutions is given in Tables 1 and 3.

3.2. Solid material

The solid material used in the experiments consisted of basaltic glass collected from Mt. Stapafell, SW Iceland. The solid material was ground and then sieved to obtain a 45–125 μm size fraction which was then used in the experiments. The material was ultrasonically cleaned in deionized water and acetone. An ultrafine suspension was removed at the end of each cleaning cycle. The cleaned material was dried overnight at 50 °C. The chemical composition of the basaltic glass is given in Table 2 (Oelkers and Gislason, 2001) and the geometric surface area (A_{geo}) was calculated to be 261 cm^2/g using the method of Tester et al. (1994).

3.3. Experimental setup

The experiments were carried out at 100, 200, 240 and 250 °C using a 29-cm long flow-through column reactor. A schematic illustration of the reactor system is shown in Fig. 2. It consisted of inlet solutions, HPLC pump(s) (Chromotech®), an inline sample valve (Vici), a reaction column made of Inconel and filled with basaltic glass, a cooling jacket, and a back pressure regulator (Coretest). All wetted parts of the experimental apparatus were made of inert material, including PEEK, titanium and Inconel. The reactor was heated to within ± 2 °C of the desired temperature using a heating mantle and a temperature controlling system. The experimental pressures were kept at ~55 bar. The flow-rate of the inlet solutions was ~0.5 ml/min. The experimental conditions are summarized in Table 1. For the series A experiments, two inlet solutions were pumped into a mixing chamber and connected with a tube to the reactor, whereas in the series B experiments, only one inlet solution was used. The series A experiments were carried out at 100, 200 and 240 °C, whereas the series B experiments were carried out at 250 °C.

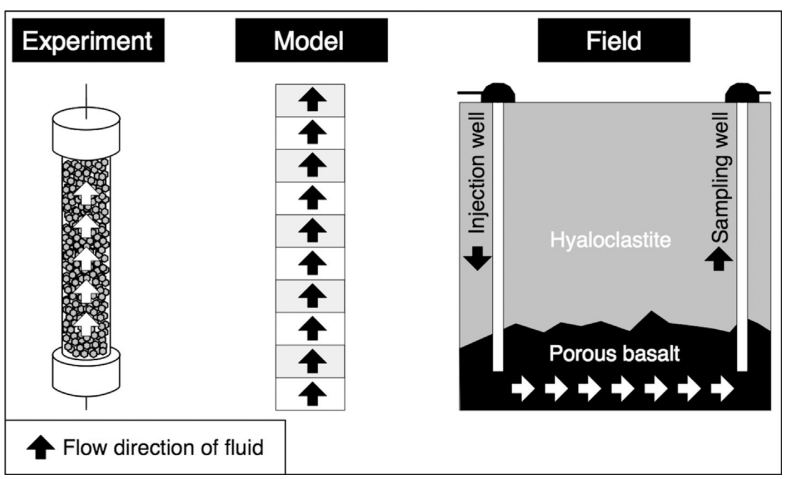

Fig. 1. Schematic comparison of fluid-rock interaction in porous medium in an experiment column filled with ground basaltic rock, transport model with reactive cells and geothermal field with porous aquifer layer (see text for details).

Table 1
Summary of the inital experimental conditions.

#	Series	T °C	Mass of basaltic glass	Duration	Inlet solution		Inital porosity
		°C	g	h	pH/22 °C	ΣS^{-II} mmol/kg	%
R1-1504	A	100	50	356	5.94–7.70	10.4–13.6	36
R1-glass	A	200	50	308	2.39–2.59	1.64–2.55	36
R1-BG-240	A	240	50	432	1.75–2.04	7.28–15.6	36
BG-1	B	250	37	260	7.26–7.50	2.50–3.76	53
BG-2	B	250	35	139	6.97–7.44	2.42–31.3	55

Table 2
The compostion of the basaltic glass from Stapafell used in the experiments and NORM basalt.

	Stapafell[a]	N-MORB[b]
	wt%	wt%
SiO_2	48.12	49.85
TiO_2	1.56	1.42
Al_2O_3	14.62	15.3
Fe_2O_3	1.11	
FeO	9.82	
Fe_{TOT}	10.93	10.35
MnO	0.19	0.19
MgO	9.08	8.01
CaO	11.82	11.49
Na_2O	1.97	2.6
K_2O	0.29	0.1
P_2O_5	0.2	0.16

[a] Oelkers and Gislason (2001).
[b] GERM (2000).

3.4. Solution analysis

Samples of the outlet solutions were collected at the low-pressure end of the back pressure regulator for major elemental analysis. Samples of the inlet solutions were collected using an in-line sampling loop (series A) or directly from the inlet solution bottle (series B). About 5 ml of solution were collected for immediate pH analysis using a combination pH electrode (713 Metrohm pH electrode coupled to a Mettler Toledo Inlab® 422 potentiometer). A further sample was collected for the determination of total dissolved sulfide (H_2S) analyzed by precipitation titration using mercuric acetate as a titrant and dithiozone as an indicator (Arnórsson et al., 2006). Samples for major elemental determination (Si, Na, K, Mg, Ca, Fe, Al and Cl) were filtered through a 0.2 µm filter (cellulose acetate), acidified to 1% using HNO_3 (Merck, Suprapur®), and degassed using N_2 followed by analysis using ICP-OES (Spectro Vision). The analytical precision based on repeated analysis of the internal standard (GYG13) at the 95% confidence level was > 3% for most elements, but as high as ~14% for Fe. The error of the pH measurements was estimated to be ± 0.05 pH units.

3.5. Solid analysis

The surface morphology, before and after the experiments, and the secondary mineralogical composition of the solid products were analyzed using scanning electron microscopy (LEO Supra™ 25 FE-SEM) and standard energy-dispersive spectrometry (EDS), both at the Innovation Center Iceland, Reykjavík. All chemical analysis was performed using an acceleration voltage of 20 kV, a beam current of 200 pA and a beam diameter of 1–2 µm. Natural and synthetic minerals and glasses were used as standards to check for potential drift.

In addition, the chemical composition of the alteration products was determined using electron microprobe analysis (EMPA) with JOEL Superprobe JSL 8200 at the University of Copenhagen. The analysis was performed using an acceleration voltage of 15 kV, a beam current of 15 nA and a beam diameter of 2 µm. Natural and synthetic minerals and glasses were used as standards to check for potential drift.

3.6. Dissolution rates

The steady-state sequestration rates r_{geo} (log mol/m^2/s) have been

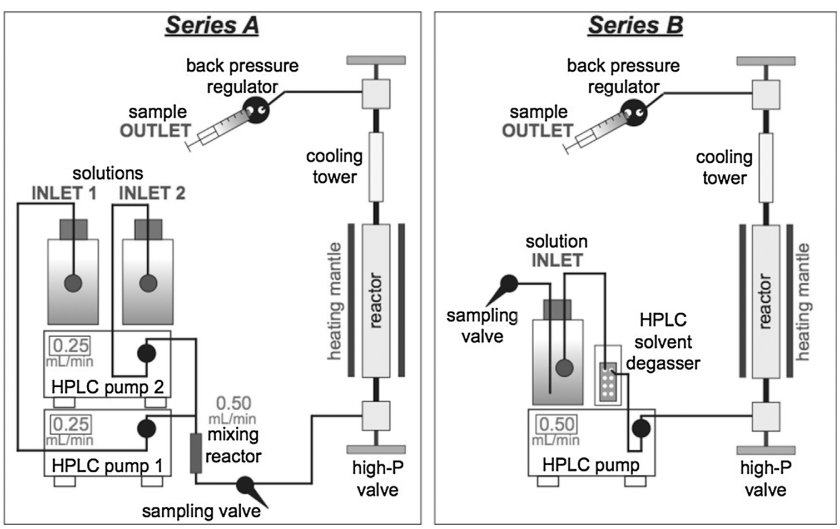

Fig. 2. Schematic figure of the experimental setup, with both series A (left) and B (right). Series A was conducted with two inlet solutions, whereas series B with one solution only.

Table 3
Chemical composition of experimental inlet and outlet solutions.

#	T	Duration	Flow rate	Inlet solution (mmol/kg)				Outlet solution (mmol/kg)								
	°C	hours	ml/min	pH/22 °C	ΣS^{-II}	Na	Cl	pH/22 °C	ΣS^{-II}	Si	Na	K	Ca	Mg	Fe	Al	Cl
R1-1504-1	100	23	0.50						0	1.21	19.6	0.012	0.33	0.149	0.0019	0.010	15.8
R1-1504-2	100	46	0.50	6.96	11.1	22.2	16.4	7.02	9.01	1.09	19.4	< 0.01	0.25	0.110	0.0009	0.006	15.7
R1-1504-3	100	66	0.52	6.90	10.8	21.6	16.3	6.82	8.78	0.91	19.2	< 0.01	0.15	0.206	0.0004	0.002	17.5
R1-1504-4	100	115	0.52	5.94	10.6	21.2	20.2	6.55	8.50	0.66	19.5	< 0.01	0.10	0.239	0.0003	0.001	17.9
R1-1504-5	100	171	0.52	6.35	10.4	20.9	18.6	6.56	8.28	0.93	21.1	< 0.01	0.03	0.049	0.0003	0.013	14.6
R1-1504-6	100	210	0.50	7.22	11.9	23.8	15.9	7.26	9.20	0.59	20.2	0.02	0.12	0.189	0.0008	0.007	15.3
R1-1504-7	100	259	0.50	6.92	11.0	22.1	16.5	6.96	9.02	0.56	19.7	< 0.01	0.12	0.181	0.001	0.006	15.1
R1-1504-8	100	283	0.50	6.91	11.2	22.5	16.9	7.00	9.13	0.51	19.5	< 0.01	0.11	0.178	0.0003	0.005	15.4
R1-1504-9	100	356	0.50	7.70	13.6	27.3	15.5	6.98	9.68	0.25	9.75	< 0.01	0.06	0.085	< 0.0001	0.002	7.49
R1-glass-1	200	119	0.50	2.42	1.73	3.47	7.67	7.91	0.61	3.54	4.30	0.042	1.38	0.011	0.0023	0.007	6.40
R1-glass-2	200	139	0.50	2.44	1.88	3.76	7.70	8.03	0.86	3.53	4.37	0.049	1.37	0.003	0.0003	0.008	6.49
R1-glass-3	200	164	0.50	2.39	1.64	3.28	7.73	7.80	0.62	3.45	4.27	0.046	1.30	0.002	0.0002	0.007	6.28
R1-glass-4	200	188	0.50	2.45	1.94	3.88	7.76	8.03	0.40	3.32	4.33	0.048	1.37	0.002	0.0003	0.007	6.37
R1-glass-5	200	220	0.50	2.50	2.17	4.34	7.78	7.80	1.01	3.64	4.38	0.045	1.40	0.002	0.0003	0.007	6.44
R1-glass-6	200	236	0.50	2.49	2.17	4.33	7.81	7.80	0.93	3.60	4.41	0.052	1.46	0.002	0.0003	0.006	6.53
R1-glass-7	200	259	0.45	2.45	1.99	3.98	7.84	7.92	0.88	3.61	4.43	0.047	1.44	0.002	0.0002	0.007	6.57
R1-glass-8	200	283	0.40	2.59	2.55	5.10	7.87	7.68	1.19	3.77	4.36	0.044	1.40	0.001	0.0002	0.007	6.48
R1-glass-9	200	308	0.30	2.54	2.40	4.79	7.90	7.83	1.01	3.65	4.63	0.075	1.39	0.002	0.0002	0.006	6.20
R1-BG-240-1	240	96	0.50		12.87	25.74	12.00	6.95	7.32	4.31	18.0	0.06	1.28	0.036	0.001	0.008	18.5
R1-BG-240-2	240	168	0.52	1.97	14.62	29.24	41.61	6.03	6.99	5.95	17.0	0.07	1.69	0.079	0.001	0.009	20.3
R1-BG-240-3	240	216	0.50	2.04	15.05	30.09	40.72	6.30	7.18	5.49	22.5	0.09	1.79	0.073	0.001	0.012	26.2
R1-BG-240-4	240	288	0.50	1.93	15.57	31.15	44.67	6.90	5.02	8.85	20.1	0.13	3.46	0.032	0.001	0.004	26.7
R1-BG-240-5	240	336	0.48	1.87	15.06	30.12	45.95	6.92	4.81	3.79	19.8	0.12	3.69	0.022	0.001	0.002	28.1
R1-BG-240-6	240	384	0.50	1.86	8.71	17.42	33.30	9.39	3.36	5.87	23.3	0.24	0.43	0.003	0.001	0.062	21.3
R1-BG-240-7	240	432	0.50	1.75	7.28	14.57	35.14	7.16	2.27	9.50	14.9	0.22	3.19	0.013	0.001	0.008	21.0
BG1-1	250	3	0.55	7.38	3.76	12.8	10.02	4.26	0.12	3.97	5.5	0.646	0.34	0.212	0.0151	0.006	5.41
BG1-2	250	24	0.50	7.39	3.52	12.5	9.67	9.28	2.78	0.03	12.3	< 0.01	0.00	0.002	0.0039	0.001	9.71
BG1-3	250	45	0.50	7.50	2.95	12.3	9.44	8.90	2.34	1.47	12.9	0.064	0.09	0.001	< 0.0001	0.460	9.61
BG1-4	250	66	0.51	7.33	3.19	11.3	9.07	8.97	2.51	1.50	12.0	0.074	0.23	0.001	< 0.0001	0.298	8.97
BG1-5	250	91	0.52	7.44	2.50	11.4	9.11	9.39	2.07	1.56	12.0	0.096	0.30	0.0004	< 0.0001	0.184	9.11
BG1-6	250	98	0.50	7.36	3.25	11.5	8.91	9.46	2.62	1.58	12.3	0.098	0.27	0.0003	0.0001	0.174	9.05
BG1-7	250	119	0.50	7.48	3.09	11.4	9.08	9.42	2.55	1.67	12.3	0.108	0.27	0.0003	< 0.0001	0.147	8.87
BG1-8	250	139	0.50	7.49	2.88	11.6		9.39	2.46	1.75	12.3	0.113	0.24	0.0003	< 0.0001	0.142	8.92
BG1-9	250	163	0.50	7.26	3.11	11.5	9.41	9.25	2.61	1.92	12.7	0.129	0.20	0.0003	< 0.0001	0.133	9.20
BG1-10	250	187	0.50	7.34	2.61	11.3	9.14	9.26	2.26	1.83	11.9	0.118	0.23	0.0003	< 0.0001	0.114	8.97
BG1-11	250	213	0.50	7.36	3.01	11.4	9.15	9.28	2.59	1.93	12.2	0.133	0.18	0.0003	< 0.0001	0.119	8.91
BG1-12	250	237	0.48	7.50	2.85	11.4	9.08	9.32	2.39	1.94	12.0	0.134	0.16	< 0.0002	< 0.0001	0.120	8.85
BG1-13	250	260	0.50	7.37	3.13	11.4	9.15	9.37	2.57	2.04	12.3	0.147	0.14	0.0003	< 0.0001	0.120	9.05
BG2-1	250	3	0.45	7.36	2.91	11.54	9.32	6.28	0.15	4.26	11.0	0.493	0.60	0.030	0.0043	0.075	10.9
BG2-2	250	18	0.45	7.44	2.48	11.21	9.19	9.68	1.83	3.02	13.3	0.216	0.02	0.0005	0.0005	0.648	8.91
BG2-3	250	42	0.48	6.97	3.11	10.54	9.04	9.16	2.23	1.61	11.4	0.101	0.31	0.0004	< 0.0001	0.154	8.87
BG2-4	250	66	0.40	7.03	2.57	10.57	9.05	9.22	1.77	1.61	11.2	0.108	0.31	0.0004	< 0.0001	0.150	8.99
BG2-5	250	90	0.50	7.08	3.11	10.68	9.04	9.27	2.41	1.75	11.7	0.137	0.22	0.0003	< 0.0001	0.152	8.95
BG2-6	250	117	0.50	7.21	2.45	10.67	9.24	9.46	1.82	0.97	11.3	0.155	1.38	0.0008	0.0006	0.088	10.3
BG2-7	250	138	0.50	6.99	3.13	10.54	9.07	9.20	2.33	1.97	12.5	0.199	0.18	0.0003	< 0.0001	0.181	9.40
BG2-8	250	139	0.50	7.03	2.42	10.85	9.43	9.37	1.80	1.94	11.9	0.189	0.15	0.0006	< 0.0001	0.182	9.14
[a]2σ						1.22	1.92			6.54	1.22	1.01	2.75	5.240	13.89	2.030	1.92

[a] Analytical uncertainit based on repeated analysis of reference sample (GYG13).

calculated for different elements applying the following equation,

$$r_{geo} = \frac{Q \times (m_i^{inlet} - m_i^{outlet})}{A_{geo} \times M} \quad (1)$$

where Q refers to the flow rate, and m_i^{inlet} and m_i^{outlet} are the concentrations of the i-th element in the inlet and outlet solutions, respectively. To obtain the precipitation rate of minerals and the leaching rate of basalt the numerator is multiplied by the stoichiometric coefficient of the i-th element. The initial specific geometric surface area is A_{geo}, and M stands for the initial mass of ground particles in the reactor.

4. Numerical modeling

Reactive transport modeling was performed using the PHREEQC program (Parkhurst and Appelo, 2013) and PhreeqcRM module (Parkhurst and Wissmeier, 2015) for parallel computing in order to simulate the reactions occurring and influencing H_2S mineralization under geothermal conditions. A one dimension advective-dispersive-reactive transport (Appelo and Postma, 2005) was computed to mimic the flow-through column reactor experiments and enlarged field scale simulations at 250 °C as the most relevant to the Hellisheiði geothermal plant conditions. Dispersivity in each cell (10% of travelled distance) was corrected for the total length of the cell and we assumed no diffusion. The system was divided into reactive cells to track reaction progress as a function of column distance, with variable transport calculation steps to calculate experimental or prolonged duration. This number of transport shifts depended on the initial pore volume and corresponding solution refill rate; the time step associated with each shift was 3 min for experiments and 28 h for field scale simulation.

The rate of basaltic glass dissolution was calculated using the transition state theory for the *i*-th solid phase,

$$r_{+i} = A_{geo^*i} \sum_i \left(k_{T,i} \prod_j a_j^n \right) (1 - SI_i) \quad (2)$$

where A_{geo^*} is the geometric normalized reactive surface area, k_T is the kinetic rate constant, $\prod_j a_j^n$ is an activity expression for the *j*-th

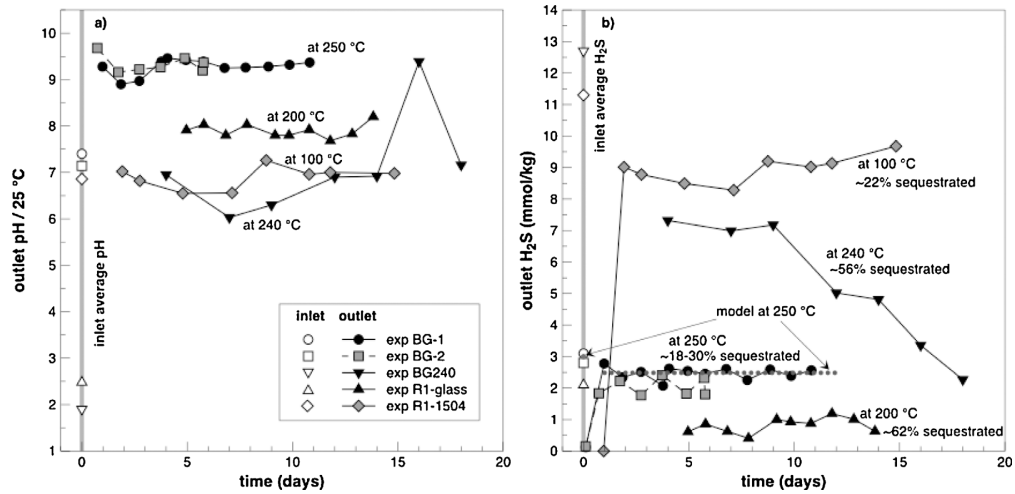

Fig. 3. Relationship between a) pH of outlet solution measured at 25 °C and b) H_2S concentration versus elapsed time, for all five experimental runs which are described as a function of reaction temperature and model I. The average inlet values of solutions are shown along the gray band.

dissolved aqueous species in solution to the power of the reaction order of species *j*, *n*, and SI is the saturation index.

The geometric normalized reactive surface area of basaltic glass A_{geo*} was obtained from the sugar-lump model (Noiriel et al., 2009),

$$A_{geo*} = \varsigma_i\left(A_{geo}^{tot} + A_m\left(1-\left(\frac{m_t}{m_0}\right)^{n_1}\right)^{n_2}\right)\left(\frac{m_t}{m_0}\right)^{n_3} \quad (3)$$

where ς_i is the reactive surface area of the phase, A_{geo}^{tot} is the total initial geometric surface area, A_m is the maximum surface area given by the sum of the surface areas of all individual particles, m_t/m_0 is the number of moles left as a function of time over the initial number of moles of the solid material, and $n_{1,2,3}$ are empiric coefficients defined by the geometry of the aggregates. In addition to the sugar-lump model, the coefficient ζ_i ranges from 0 to 1, from non-reactive to fully reactive surface of grains, respectively. In this case, the value of ζ_i was defined as equal to 1 as in Přikryl et al. (2017). The dissolution rate constant (k) of basaltic glass, $2.2{\cdot}10^{-7}$ mol/m^2/s, was fitted to experimental outcomes at 250 °C and was based on the results and approach of Guy and Schott (1989), Berger et al. (1994) and Daux et al. (1997).

Secondary minerals were allowed to form when saturated, i.e. no precipitation kinetics were included in the reactive transport simulations. The saturation indices, SI_i, were calculated based on,

$$SI_i = \frac{Q_i}{K_i} = \frac{\prod_j a_j^{v_j}}{K_i} \quad (4)$$

where Q_i and K_i are the reaction quotient and equilibrium constant of the i-th mineral, and a_j and v_j are the respective activities to the stoichiometric power that are negative for reactants and positive for products. The thermodynamic properties of aqueous species and minerals used to calculate the mineral solubility at water saturation pressure were taken from Phillips et al. (1988), Delaney and Wolery (1989), Johnson et al. (1992), Arnórsson and Stefánsson (1999), Gysi and Stefánsson (2011), Holland and Powell (2011), and Aradóttir et al. (2012). The aqueous speciation and reaction quotients were calculated with the aid of the PHREEQC program.

Two sets of reactive transport models were conducted (model I and II), the difference between the models reflecting variable mineral paragenesis. Model I incorporated the formation of secondary mineral phases observed experimentally in this study, whereas model II included mineralization of secondary phases commonly observed in geothermal systems at temperatures between 200 and 300 °C (e.g., Kristmannsdóttir, 1979; Stefánsson et al., 2011).

Finally, the total porosity ϕ within the reactor was calculated based on the volume difference of an empty reactor ($V_{reactor}$) and the volume of the solid material in the reactor, $V_{material}$,

$$\phi = \frac{V_{reactor} - V_{material}}{V_{reactor}} \times 100 = \frac{V_{reactor} - \sum m_i/\rho_i}{V_{reactor}} \times 100 \quad (5)$$

where m_i is the mass of basaltic glass and secondary phases, and ρ_i are the respective densities.

5. Assessing the process of H_2S sequestration into rocks

5.1. Solution trends

The chemical composition of the inlet and outlet experimental solutions is reported in Table 3. The inlet solution composition was very variable, whereas at each temperature the outlet solution composition was relatively constant. This was best reflected by the pH variations. The inlet pH varied from acid to neutral pH. However, pH of all the outlet solutions was neutral to mildly alkaline within a relatively narrow pH range with few exceptions: 6.55–7.26 at 100 °C, 7.68–8.20 at 200 °C, 6.03–9.39 at 240 °C and 8.90–9.68 at 250 °C (Fig. 3A). The same was observed for the major elemental chemical composition (Table 3). After the initial period of 2–4 days, most elemental concentrations including Si, Ca and Fe reached a stable concentration, with the absolute concentrations varying depending on temperature.

The concentrations of H_2S in the outlet solution are shown in Fig. 3B. In all cases, they attained close to a constant value at a given temperature, independently of the inlet H_2S concentration in solution: 8.50–9.69 mmol/kg at 100 °C, 0.40–1.19 mmol/kg at 200 °C, and 1.77–2.78 mmol/kg at 250 °C, but not actually for 2.27–7.32 mmol/kg at 240 °C (Fig. 3B). This is thought to indicate that fluid-rock interaction influenced the H_2S concentration at each temperature and pH, rather than the input H_2S concentration.

5.2. Secondary mineralogy

The typical surface morphology and secondary phases, with relative EDS spectra, obtained with the experiments are presented in Fig. 4 and the chemical composition determined by EMPA analysis is listed in Table 4. The most abundant ratio of precipitated secondary phases was observed on the inlet side, decreasing into the reactor along the flow-

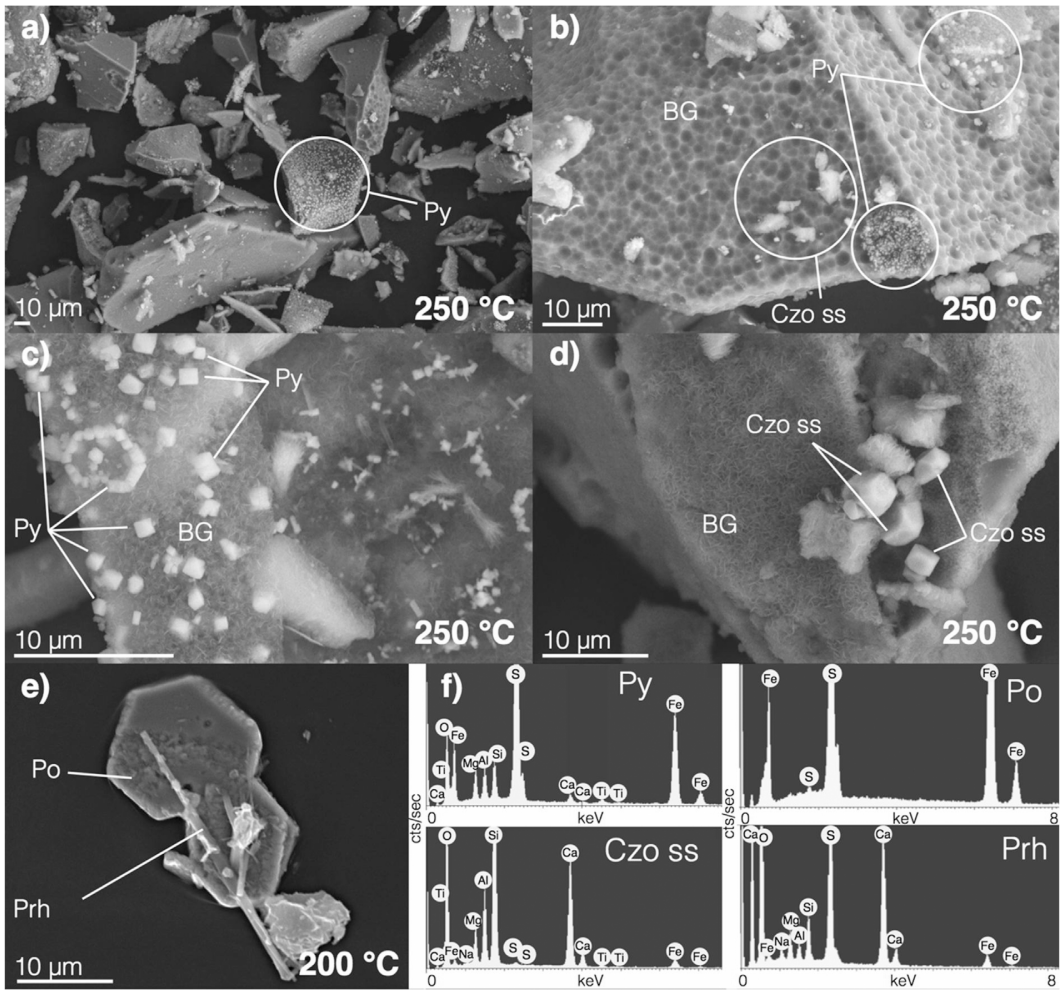

Fig. 4. SEM images of typical secondary phases: a) aggregates of basaltic glass (BG) with precipitated pyrite (Py); b) weathered grain all over the surface, and secondary pyrite and clinozoisite solid solution (Czo ss) along the depression edges; c) euhedral pyrite crystals; d) subhedral clinozoisite crystals; e) pyrrhotite (Po) with prehnite (Prh); f) and EDS spectra, some with basaltic glass interference on the background.

Table 4
The composition of altered material, selected EMPA analyses on reaction rim after experiments at 200 °C (R1-glass). Altered basaltig glass = BG, Pyrrhotite = Prh.

	BG	BG	Prh	Prh		Alteration rim			
wt%	AB-1	AB-2	s5-33	s5-34	s6-2	s6-16	s6-26	s6-27	s6-30
SiO_2	37.7	37.4	0.06	0.12	31.55	33.64	34.57	34.30	34.47
TiO_2	2.18	2.11	0.00	0.05	2.19	2.44	2.17	1.58	1.86
Cr_2O_3	0.07	0.1	0.00	0.00	0.09	0.06	0.03	0.08	0.05
Al_2O_3	12.8	11.6	0.10	0.20	16.56	18.85	17.84	18.61	17.88
SO_3	0.01	0.02	62.50	62.90	3.89	0.96	0.83	1.25	0.00
FeO	18.7	17.8	37.20	36.70	14.95	10.20	12.46	11.08	13.15
MnO	0.31	0.31	0.02	0.00	0.29	0.57	0.33	0.25	0.29
MgO	13.7	11.5	0.00	0.03	19.37	18.70	20.50	18.87	17.32
CaO	3.57	3.38	0.05	0.06	0.63	0.85	1.93	2.51	1.22
Na_2O	0.36	0.46	0.00	0.04	0.10	0.14	0.12	0.07	0.02
K_2O	0.24	0.34	0.02	0.01	0.02	0.05	0.07	0.02	0.01
Total	89.6	85.1	99.95	100.11	89.64	86.46	90.85	88.62	86.27

path. The secondary minerals containing sulfur included pyrrhotite that was only observed at 200 °C, whereas pyrite was the major sulfide mineral at 100, 240 and 250 °C. The pyrite displayed euhedral crystals of ~1–3 µm pyrite, and pyrrhotite up to ~20 µm. On the other hand, only a small amount of pyrite was observed at 100 °C, together with prevailing secondary iron oxides. Other common phases identified in the experiments are clay minerals at 100 °C, prehnite at 200 °C, and the solid solution of clinozoisite-epidote at 250 °C, with a prevailing clinozoisite end-member. Clinozoisite forms mostly subhedral crystals up to 5 µm, and its precipitation seems to be more abundant in the upper part of the reactor than sulfides.

Further inspection of the alteration products of basalt at 200 °C (Table 4) reveals three trends in cross sections: composition close to altered basalt, composition close to pyrrhotite and an alteration rim with composition close to that encountered in smectite, and chlorite members rich in Mg and Fe as, for instance, saponite.

Calcium-containing phases such as feldspars, zeolites, epidote end-member and wollastonite were not observed within the alteration product according to the EMPA analysis, whereas a clinozoisite in solid

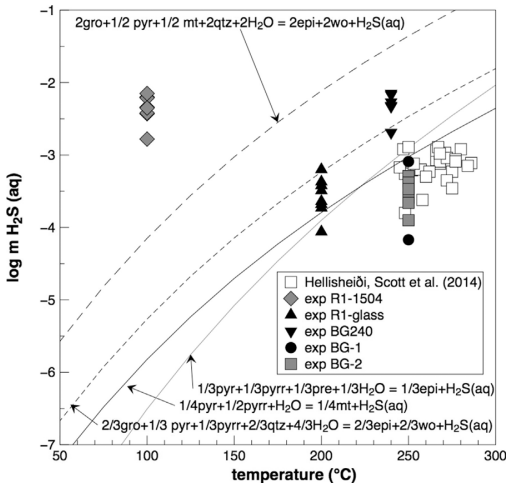

Fig. 5. The concentration of H_2S(aq) in the experimental solutions as a function of temperature. Shown are also the concentrations for reservoir waters at Hellisheiði (Scott et al., 2014) and the predicted equilibrium concentrations for four possible mineral buffer reactions.

solution and prehnite were clearly identified by SEM and EDS analysis. Moreover, anhydrite and other sulfate minerals were absent from the alteration product, suggesting a limited oxidation of H_2S to SO_4 in the experiments.

6. Discussion

6.1. H_2S mineralization under geothermal conditions

The decrease in H_2S concentrations between the inlet and outlet solutions, together with the observed formation of sulfide minerals like pyrite and pyrrhotite, indicate that H_2S mineralization took place with a fluid-rock reaction of H_2S-rich solutions and basaltic rocks under geothermal conditions.

The process of mineralization of H_2S from solution may be summarized from the percentage difference between the H_2S concentration in the inlet and outlet solutions. The difference at 100 °C corresponds to up ~22% of the injected H_2S converted into sulfur-containing minerals, like pyrite and possibly also into elemental sulfur (e.g. Meyer, 1976; Stefánsson et al., 2011), whereas at 200, 240 and 250 °C the difference indicates that ~62% of H_2S are mineralized into pyrite and pyrrhotite at an acidic pH and up to ~30% at a neutral pH.

In Fig. 5, the activities of H_2S(aq) in the outlet experimental solutions are compared with those calculated, assuming equilibrium with mineral buffers in reactions thought to control H_2S concentrations under geothermal conditions (e.g., Stefánsson and Arnórsson, 2002; Stefánsson et al., 2015; Gunnarsson-Robin et al., 2017). The H_2S(aq) activities in the reservoir fluids in the Hellisheiði geothermal system are also shown for comparison (Scott et al., 2014). As observed, the results of the experiments at 200–250 °C were close to those predicted, assuming equilibrium between fluids and selected minerals. The same was true with respect to geothermal fluids at Hellisheiði. In contrast, the experimental outlet solutions at 100 °C were considerably higher concentrated than those predicted by fluid-mineral equilibria. This suggests that at low temperature (100 °C) a significant amount of time is needed to attain equilibrium with respect to H_2S, whereas at higher temperatures (> 200 °C) the attainment of H_2S-fluid-mineral equilibrium is relatively rapid.

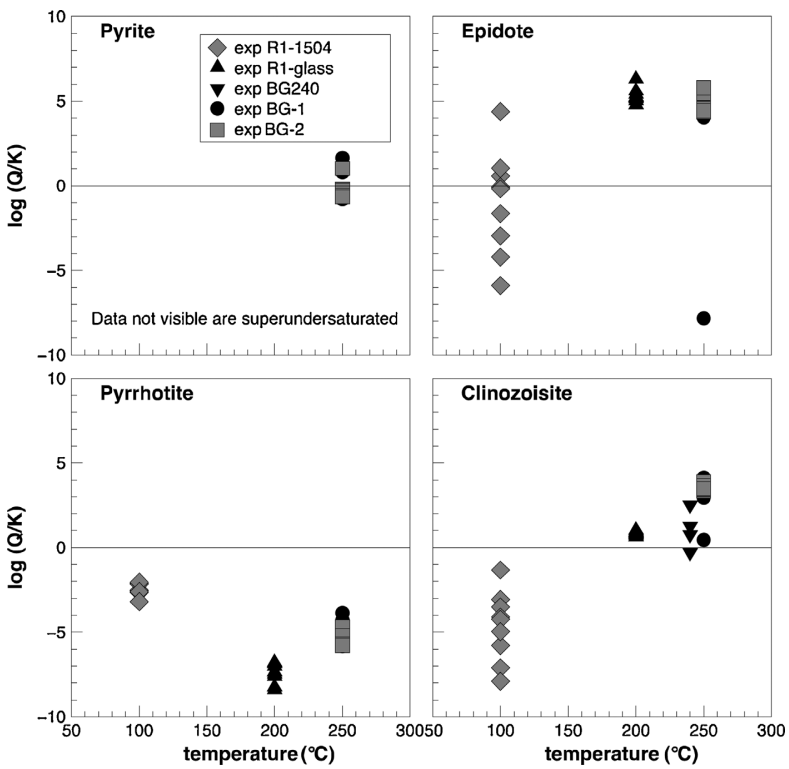

Fig. 6. Saturation index of the experimental solutions with respect to selected common geothermal minerals.

Many of the reactions suggested to possibly control H_2S concentration in geothermal fluids involve Ca-containing aluminum silicate minerals, such as epidote, grossular and wollastonite, which were not observed to form during the experiments. Investigation of the equilibrium with respect to some of these minerals reveals that the outlet experimental solutions were supersaturated with, for example, epidote (Fig. 6), resulting in higher Ca concentrations in the outlet experimental solutions than observed for natural geothermal fluids. This suggests that either more time is needed to attain equilibrium with common Ca-containing aluminum silicates than for pyrite, or that the system is mass limited, i.e. that there is a limited supply of some elements such as Al needed to form the Ca-containing aluminum silicates.

6.2. Rates and mechanisms of H_2S mineralization under geothermal conditions

The H_2S mineralization rates were calculated using the difference between inlet and outlet H_2S concentrations, the flow rate, and the basaltic glass surface area in the flow-through reactor (Eq. (1)). With the stoichiometric coefficient for Fe in pyrite and pyrrhotite the rate was normalized to Fe precipitation rates of the respective sulfides. The results are shown in Fig. 7 as a function of pH. At each temperature, relatively steady state rates were observed within 1–2 days after the start of the experiments, with rates increasing with a decreasing pH of the solution. The precipitation rates of H_2S are affected by the fluid's pH rather than by temperature and concentration (Fig. 7). However, at 100 °C the precipitation rates of Fe compounds did not correspond to the H_2S mineralization rate into sulfides completely, as elemental sulfur was formed too. This reaction explains the tiny amount of pyrite observed by SEM-EDS. In contrast, the H_2S mineralization rates at 250 °C correspond closely to the Fe dissolution rates modeled for basalt, based on mass balance. This suggests that the limiting factor in H_2S mineralization on re-injection of H_2S-rich fluids into geothermal systems is the leaching rate and availability of Fe. As the primary rock was dissolved during the transport, the pH of the fluid causes different release rates of Fe, which has a substantial effect on H_2S abatement, calculated from the dissolution and precipitation rates.

To get further insight into the mineralization of H_2S into pyrite, reactive transport calculations were conducted, simulating the conditions of the experimental flow-through the reactor. The results of the calculations reveal that the fluid-rock interaction process and H_2S mineralization along the flow-path of the flow-through reactor is somewhat more complicated than implied by the bulk basaltic glass dissolution and H_2S mineralization rates. Upon injection of H_2S-rich solutions into the flow-through reactor, an analogue to H_2S re-injection into geothermal reservoirs, rapid basaltic dissolution occurred, followed by H_2S mineralization into pyrite. Moreover, the basaltic glass dissolution results in the uptake of H^+, increased pH of the pore solutions along the flow path, and decreased basaltic glass dissolution rates and, hence, the quantity of alteration products. The results of the reactive transport calculations also demonstrate that the H_2S mineralization depends on secondary mineral paragenesis. Assuming that the pyrite-clinozoisite-clinochlore (model I) dominates the alteration mineralogy, the greater part of the Fe released from basaltic glass was consumed by pyrite. In contrast, assuming that pyrite, pyrrhotite, prehnite and epidote dominates the alteration mineralogy (model II), less H_2S mineralization into pyrite is observed due to significant uptake of Fe by epidote (Fig. 8). However, independent of modeled alteration mineralogy, pyrite is observed to preferentially form on the inlet side of the reactor, where the Fe leaching rate is rapid.

6.3. Sustainability of H_2S sequestration into geothermal systems

Based on the results of short term experimental and reactive transport modeling it is clear that H_2S-rich solutions re-injected into geothermal reservoirs with basaltic host rocks at temperatures higher than 200 °C are likely to cause vigorous dissolution of the primary rocks, followed by pyrite formation. However, the sustainability of such long-term injections and sequestration are unknown. Among the main questions needed to be answered for optimal H_2S sequestration in geothermal systems are: (1) the prolonged availability of Fe for pyrite formation, (2) the movement of the pyrite mineralization zone eventually reaching production wells, and (3) clogging of the reservoir due to intensive mineralization of pyrite close to the H_2S-rich fluid re-injection well.

In order to answer these questions, the reactive transport simulations were extended to cover a duration of H_2S-rich fluid re-injection for 120 years at 250 °C with conditions similar to those observed at Hellisheiði and associated with the Sulfix project (e.g., Gunnarsson et al., 2013). The system was characterized by an initial 10% porosity flow of 8.9 m/day and H_2S concentration of the injection fluid entering the reservoir of ~30 mmol/kg (Gunnarsson et al., 2011; Gunnarsson et al., 2013). The reactor dimensions were scaled up to 96 m in length and 3.6 m in width. In accordance with the reactive modeling (Fig. 9) the porosity close to the re-injection well was observed to increase with time due to the vigorous dissolution of the basaltic glass and formation of secondary minerals dominated by pyrite and some chlorite and epidote. A few meters into the geothermal reservoir, away from the outlet of the re-injection well (< 40 m within 120 years), the fluid-rock interaction had reached fluid chemistry and alteration mineralogy patterns observed within natural geothermal systems. Furthermore, the system maintained a similar rate over 120 years (a convenient time frame with other short-term simulations), dissolving 26% of the 2600 t of initial basalt, and precipitating 114 t of pyrite in 120 years. The modeled porous medium, of $1{\cdot}10^3$ m^3 (area of 0.001 km^2), could sequestrate 32 t of H_2S (16% of injected H_2S within the modeled volume) without clogging the system. This means 32 000 t/year emissions at Hellisheiði would be safely captured within a volume of $1{\cdot}10^6$ m^3 of rock, which will still have ~75% of its mass available for fluid-rock reaction. However, coating of the surface by secondary phases has not been considered and could mean an additional limitation of Fe supply. Fig. 9 shows a partly mobile reaction front for secondary minerals forming, where the mass of precipitated silicates is being shifted and re-mineralized farther along the flow path with elapsed time. On the other hand, sulfides were stable after precipitation and subsequent re-dissolution was not observed within the duration studied.

6.4. Comparison of Sulfix with common sequestration methods: economic implications

The reduction of the anthropogenic sulfur discharges into the atmosphere was influenced by the cost of the H_2S abatement systems and the urgency to decrease the emissions to meet air quality regulations. Many geothermal power plants have already been equipped with H_2S abatement apparatus (≥90% removal factor), employing burning and scrubbing with alkali, liquid-redox processes (e.g., Stretford, Unisulf, LO-CAT, SulFerox, and Hiperion), and oxidizing biocide "BIOX", from which the H_2S is converted to sulfates, elemental sulfur, and water-soluble sulfates, respectively (e.g., Dalrymple et al., 1989; Farison et al., 2010; Gallup, 1994; Nagl, 2009; Owen and Michels, 1984; Rodríguez et al., 2014; Sanopoulos and Karabelas, 1997; Stephens et al., 1980; Takahashi and Kuragaki, 2000; World Environment Center, 1994). A plant-specific method called AMIS has been implemented in the Italian field of Larderello, to deal with the particularly mercury-rich geothermal resources (Baldacci, 2004). Thanks to the AMIS process, the average specific emissions of mercury and H_2S decrease by 23 and 30%, respectively, producing sulfur dioxide (Pertot et al., 2013). An example of methods used in the gas industry, which are potentially applicable to geothermal power plants, is the THIOPAQ, which involves the use of microorganisms for oxidizing the H_2S to elemental sulfur (Benschop et al., 2002; Padilla, 2007). However, despite the different technicalities and final by-products, the standard abatement methods have

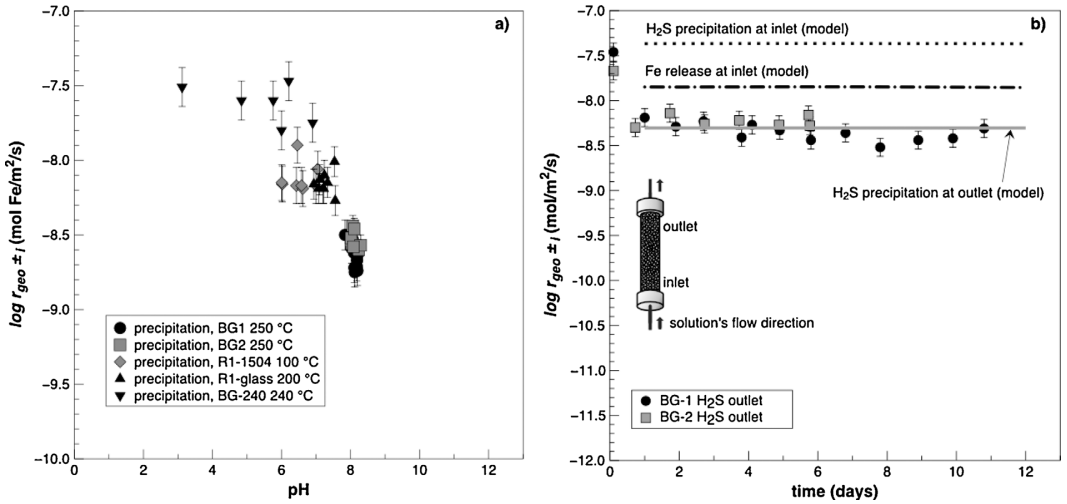

Fig. 7. A) Experimental H_2S sequestration rates shown as a precipitation rate of Fe in sulfide minerals, pyrite at 100–240–250 °C and pyrrhotite at 200 °C. B) Modeled Fe release from glass is further displayed as a function of the reactor distance, together with the modeled and experimental H_2S precipitation rates on the inlet and outlet sides at 250 °C.

relatively high operating costs in common (Table 5).

A more attractive option for the geothermal industry is on-site H_2S injection (SulFix), together with condensed steam and waste water, into the geothermal reservoir, where the cost per tonne of sequestered H_2S is one or even two orders of magnitude lower than that of the other methods. For example, if all the H_2S produced by the world's largest geothermal power plants, The Geysers (USA), were to be injected into the host reservoir, the final estimated cost would be $ < 300,000 per year, which is twenty times lower than the current abatement expenses. Still, this assessment depends on the success of H_2S mineralization through underground re-injection into different reservoir lithologies. To date, this strategy has been tested on basalt only, whereas most of the world reservoirs are characterized by intermediate to acidic rocks. Most importantly, the Fe concentration of the geothermal magmatic suite of host rocks, which has been suggested as a limiting factor in H_2S mineralization, should be evaluated.

7. Conclusions

Reduction of H_2S emissions from geothermal power plants is an important environmental, economic, and social challenge that needs to be addressed. The geochemistry associated with H_2S-injection into a geothermal reservoir with basaltic host rock followed by sulfide mineralization was investigated experimentally and reactive transport modeling used to determine the geochemical feasibility of such H_2S sequestration.

Re-injection of H_2S-rich fluids into geothermal systems resulted in dissolution of basalt, followed by mineralization of the H_2S into pyrite. At low temperatures (~100 °C) the reactions were observed to be limited to stable H_2S mineralization. At higher temperatures

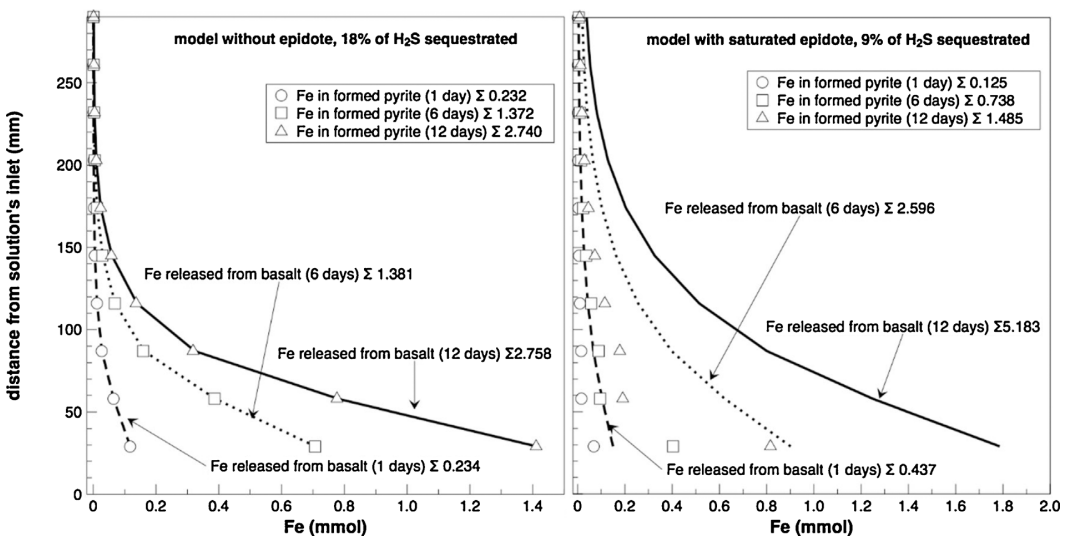

Fig. 8. Cumulative release of Fe from basaltic glass (BG) shown as a function of distance from the solution inlet, together with the Fe precipitated as a pyrite, for both model I (left) and II (right). Majority of Fe released from BG is consumed by pyrite in model I (without epidote), whereas in model II (with precipitating epidote) only about 1/3 of total released Fe from basalt forms sulfide minerals and the rest is bound to silicates.

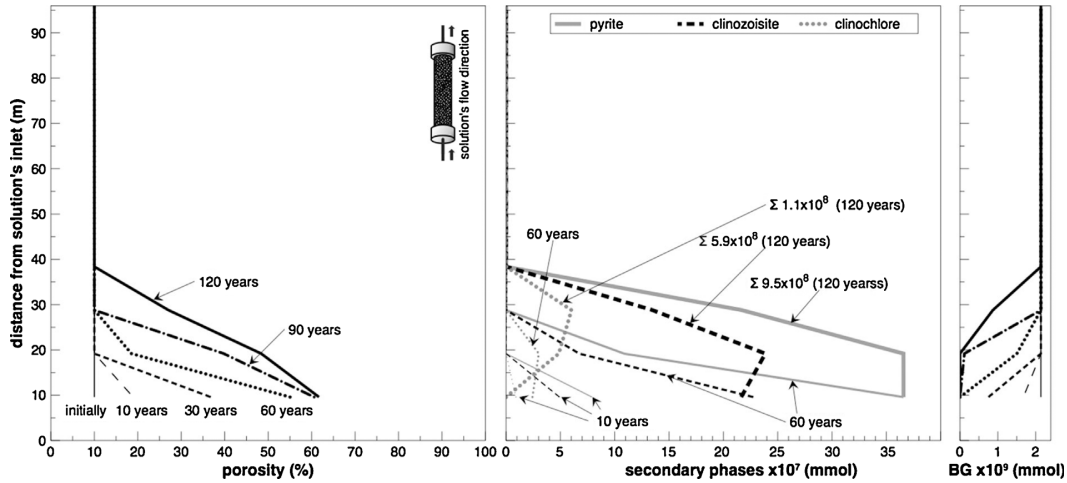

Fig. 9. Model results of porosity, formed secondary phases and basaltic glass dissolution as a function of distance from the solution inlet are shown for ~10% of initial porosity, and ~30 mmol/kg of injected H_2S concentration. The model results are extrapolated for different time-series, ranging from 10 to 120 years. The Σ represents the total mass of secondary phase in the system during a certain period.

Table 5
H_2S abatement costs and methods for a suite of geothermal power plants.

Location	Power Plant	Rock	H_2S emission before abatement (t/y)	Abatement method	Abatement cost ($/t of H_2S)
El Salvador[a]	Berlin	andesite	2725	THIOPAQ	725
Iceland[b]	Hellisheiði	basalt	16900	SulFix	< 30
Italy[c]	Larderello	granite	19635	AMIS	2200
USA	Coso[d]	granite	2392	LO-CAT II	225
USA	Geysers[e]	granite	6170	Burn/scrub	465
USA	Geysers[e]	granite	3880	Stretford	640

[a] Padilla (2007) and Torio-Henríquez (2007).
[b] Alfredsson et al. (2013); Júlíusson et al. (2015); Gunnarsson et al. (2013) and LDEO (2016).
[c] Personal communication Enel green power; Baldacci (2004); Barelli et al. (2010) and Pertot et al. (2013).
[d] Adams et al. (2000); Monastero (2002); Rodríguez (2013) and Rodríguez et al. (2014).
[e] Farison et al. (2010); Mamrosh et al. (2012) and Thompson (1992).

(200–250 °C) and an acidic pH the reactions were faster and resulted in up to ~62% of the injected H_2S to be stably mineralized. Moreover, the mineralization rates of H_2S were observed to be similar to the Fe leaching rates from basaltic glass. Close to equilibrium the dissolution of basalt could be the rate-limiting factor of H_2S sequestration. Uptake of other Fe-containing minerals such as epidote also decreased the H_2S sequestration efficiency. From a stoichiometric point of view, the formation of pyrite is preferred to pyrrhotite because pyrite needs less Fe and binds more S.

The main long-term effects of H_2S-rich fluid re-injection into geothermal systems are the porosity increase close to the outlet of injection well due to rock dissolution, and the fact that pyrite formation was observed not to decrease porosity fundamentally and possibly clog the system. Moreover, concentrations of the re-injected H_2S fluids (1–10 mmol/kg H_2S) were found to possibly limit release and supply of Fe and therefore H_2S sequestration. On the other hand, higher H_2S concentrations were found to result in quantitatively greater H_2S sequestration (~up to 62%) at 200–250 °C and an acid pH of the inlet fluid. It is therefore concluded that H_2S injection and sequestration is a geochemically feasible method for the reduction of H_2S emissions from geothermal power plants. The method is also much cheaper than commonly used ones and is also an economically feasible option. If the H_2S abatement by re-injection is demonstrated in different lithologies, worldwide application can save millions of dollars.

Acknowledgements

We would like to express our thanks to Gylfi Sigurðsson, Birgir Jóhannesson, Thorsteinn Jónnsson, Prathap Moola and Ríkey Kjartansdóttir for technical, analytical, and experimental assistance, and to Petr Přikryl for assistance with C++ coding. We thank reviewers for improving the manuscript and to Christopher Bromley for editorial handling. This research was supported by the European Union FP7 Marie Curie Actions Initial Training Network MINSC (290040) and CO_2-REACT (317235), and by Landsvirkjun grant DOK-08-2016 to J. Přikryl.

References

Adams, M.C., Moore, J.N., Bjornstad, S., Norman, D.I., 2000. Geologic history of the Coso geothermal system. Trans. Geother. Resour. Council 205–210.
Alfredsson, H.A., Oelkers, E.H., Hardarsson, B.S., Franzson, H., Gunnlaugsson, E., Gislason, S.R., 2013. The geology and water chemistry of the Hellisheidi: SW-Iceland carbon storage site. Int. J. Greenh. Gas Control 12, 399–418.
Appelo, C.A.J., Postma, D., 2005. In: Balkema, A.A. (Ed.), Geochemistry, Groundwater and Pollution, 2nd ed. the Netherlands.
Aradóttir, E.S.P., Sonnenthal, E.L., Jónsson, H., 2012. Development and evaluation of a thermodynamic dataset for phases of interest in CO_2 mineral sequestration in basaltic rocks. Chem. Geol. 304-305, 26–38.
Arnórsson, S., Stefánsson, A., 1999. Assessment of feldspar solubility constants in water in the range of 0–350 °C at vapor saturation pressures. Am. J. Sci. 299, 173–209.
Arnórsson, S., Bjarnason, J.Ö., Giroud, N., Gunnarsson, I., Stefánsson, A., 2006. Sampling and analysis of geothermal fluids. Geofluids 6, 203–216.
Baldacci, A., 2004. AMIS: an innovative technology for hydrogen sulfide and mercury abatement from geothermal gases. Geother. Resour. Council Trans. 28, 511–514.
Barelli, A., Ceccarelli, A., Dini, I., Fiordelisi, A., Giorgi, N., Lovari, F., Romagnoli, P., 2010. A review of the Mt. Amiata geothermal system (Italy). In: Proceedings of the World Geothermal Congress 2010. Bali, Indonesia. pp. 16.
Benschop, A., Janssen, A., Hoksberg, M., Seriwala, R., Abry, R., Ngai, C., 2002. The Shell-Paques/THIOPAQ Gas Desulphurization Process: Successful Start up First Commercial Unit. pp. 1–13.
Berger, G., Claparols, C., Guy, C., Daux, V., 1994. Dissolution rate of a basalt glass in silica-rich solutions: implications for long-term alteration. Geochim. Cosmochim. Acta 58, 4875–4886.
Dalrymple, D.A., Trofe, T.W., Evans, J.M., 1989. Liquid redox sulfur recovery options costs, and environmental considerations. Environ. Prog. 8, 217–222.
Daux, V., Guy, C., Advocat, T., Crovisier, J.-L., Stille, P., 1997. Kinetic aspects of basaltic glass dissolution at 90 °C: role of aqueous silicon and aluminium. Chem. Geol. 142, 109–126.
Delaney, J.M., Wolery, T.J., 1989. The LLNL Thermochemical Database. Report UCRL-

21658.
DiPippo, R., 2012. Geothermal Power Plants: Principles, Applications, Case Studies and Environmental Impact. Butterworth-Heinemann.
Farison, J., Benn, B., Berndt, B., 2010. Geysers power plant H_2S abatement update. Geother. Resour. Council Trans. 34, 1229–1234.
GERM, 2000. The Geochemical Earth Reference Model. https://earthref.org/GERM/.
Gallup, D.L., 1994. BIOX: A New Hydrogen Sulfide Abatement Technology for the Geothermal Industry. Gordon and Breach Basel, SUISSE.
Greaver, T.L., Sullivan, T.J., Herrick, J.D., Barber, M.C., Baron, J.S., Cosby, B.J., Deerhake, M.E., Dennis, R.L., Dubois, J.-J.B., Goodale, C.L., 2012. Ecological effects of nitrogen and sulfur air pollution in the US: what do we know? Front. Ecol. Environ. 10, 365–372.
Gunnarsson, G., Arnaldsson, A., Oddsdóttir, A.L., 2011. Model simulations of the Hengill area: Southwestern Iceland. Transp. Porous Media 90, 3–22.
Gunnarsson, I., Aradóttir, E.S., Sigfússon, B., Gunnlaugsson, E., Júlíusson, B.M., Energy, R., 2013. Geothermal gas emission from Hellisheiði and Nesjavellir power plants, Iceland. GRC Trans. 37, 785–789.
Gunnarsson-Robin, J., Stefánsson, A., Ono, S., Torssander, P., 2017. Sulfur isotopes in Icelandic thermal fluids. J. Volcanol. Geotherm. Res. http://dx.doi.org/10.1016/j.jvolgeores.2017.01.021.
Guy, C., Schott, J., 1989. Multisite surface reaction versus transport control during the hydrolysis of a complex oxide. Chem. Geol. 78, 181–204.
Gysi, A.P., Stefánsson, A., 2011. CO_2-water-basalt interaction: numerical simulation of low temperature CO_2 sequestration into basalts. Geochimica et Cosmochimica Acta 75, 4728–4751.
Holland, T.J.B., Powell, R., 2011. An improved and extended internally consistent thermodynamic dataset for phases of petrological interest: involving a new equation of state for solids. J. Metamorph. Geol. 29, 333–383.
Júlíusson, B.M., Gunnarsson, I., Matthiasdottir, K.V., Markusson, S.H., Bjarnason, B., Sveinsson, O.G., Gislason, T., Thorsteinsson, H.H., 2015. Tackling the challenge of H2S emissions. In: Proceedings of the World Geothermal Congress 2015. Melbourne, Australia.
Johnson, J.W., Oelkers, E.H., Helgeson, H.C., 1992. SUPCRT92: a software package for calculating the standard molal thermodynamic properties of minerals gases, aqueous species, and reactions from 1 to 5000 bar and 0–1000 °C. Comput. Geosci. 18, 899–947.
Kaasalainen, H., Stefánsson, A., 2011. Sulfur speciation in natural hydrothermal waters, Iceland. Geochim. Cosmochim. Acta 75, 2777–2791.
Koch, M.S., Erskine, J.M., 2001. Sulfide as a phytotoxin to the tropical seagrass Thalassia testudinum: interactions with light: salinity and temperature. J. Exp. Mar. Biol. Ecol. 266, 81–95.
Kristmannsdóttir, H., 1979. Alteration of basaltic rocks by hydrothermal-activity at 100–300 °C. Dev. Sedimentol. 27, 359–367.
LDEO Columbia University − Earth Institute (2016) http://www.ldeo.columbia.edu/news-events/first-iceland-power-plant-turns-carbon-emissions-stone.
Likens, G.E., Wright, R.F., Galloway, J.N., Butler, T.J., 1979. Acid rain. Sci. Am. 241.
Mamrosh, D., McIntush, K., Beitler, C., Markússon, S., Einarsson, K., 2012. Screening of H_2S abatement options for geothermal power noncondensable gas at Bjarnarflag. GRC Trans. 36, 1217–1226.
Meyer, B., 1976. Elemental sulfur. Chem. Rev. 76, 367–388.
Monastero, F.C., 2002. An overview of Industry-Military Cooperation in the development of power operations at the Coso Geothermal Field in Southern California. Geotherm. Resour. Council Bull. 31, 188–195.
Nagl, G., 2009. Coso Geothermal Field −15 Years of Successful H_2S Emission Abatement. Merichem Chemicals and Refinery Services, LLC.
Noiriel, C., Luquot, L., Madé, B., Raimbault, L., Gouze, P., van der Lee, J., 2009. Changes in reactive surface area during limestone dissolution: an experimental and modelling study. Chem. Geol. 265, 160–170.
Oelkers, E.H., Gislason, S.R., 2001. The mechanism, rates and consequences of basaltic glass dissolution: I. An experimental study of the dissolution rates of basaltic glass as a function of aqueous Al, Si and oxalic acid concentration at 25 °C and pH = 3 and 11. Geochim. Cosmochim. Acta 65, 3671–3681.
Owen, L., Michels, D., 1984. Geochemical Engineering Reference Manual. U.S. Departement of Energy.
Přikryl, J., Jha, D., Stefánsson, A., Stipp, S.L.S., 2017. Mineral dissolution in porous media: an experimental and modeling study on kinetics, porosity and surface area evolution. Appl. Geochem. http://dx.doi.org/10.1016/j.apgeochem.2017.05.004.
Padilla, E.K., 2007. Preliminary Study on Emission Abatement and Use of Gas from Geothermal Power Plants in El Salvador. Report 18. pp. 417–446.
Parkhurst, D.L., Appelo, C.A.J., 2013. Description of Input and Examples for PHREEQC Version 3—A Computer Program for Speciation, Batch-reaction, One-dimensional Transport, and Inverse Geochemical Calculations. US Geological Survey Techniques and Methods, Book 6, pp. 497.
Parkhurst, D.L., Wissmeier, L., 2015. PhreeqcRM: a reaction module for transport simulators based on the geochemical model PHREEQC. Adv. Water Resour. 83, 176–189.
Pertot, C., Sabatelli, F., Messia, M., Marco, D., 2013. Assessment of geothermal power plants impact on air quality −Effect of H_2S abatement with AMIS ® in the Larderello-Travale-Radicondoli geothermal area (Tuscany). Proc. Eur. Geother. Congr. 2007.
Phillips, S.L., Hale, F.V., Silvester, L.F., Siegel, M.D., 1988. Thermodynamic tables for nuclear waste isolation. Aqueous Solutions Database. Report LBL-22860, NUREG/CR-4864, SAND87-0323, vol. 1 Lawrence Berkeley Lab., Berkeley, CA, USA.
Rodríguez, E., Harvey, W.S., Ásbjörnsson, E.J., 2014. Review of H2S abatement methods in geothermal plants. In: Proceedings 38th Workshop on Geothermal Reservoir Engineering. Report SGP-TR-202. Stanford, California, USA.
Rodríguez, E., 2013. Review of H2S Abatement in Geothermal Plants and Laboratory Scale Design of Tray Plate Distillation Tower. Master Thesis. Reykjavík University.
Sanopoulos, D., Karabelas, A., 1997. H_2S abatement in geothermal plants: evaluation of process alternatives. Energy Sources 19, 63–77.
Scott, S., Gunnarsson, I., Arnórsson, S., Stefánsson, A., 2014. Gas chemistry, boiling and phase segregation in a geothermal system Hellisheidi, Iceland. Geochimica et Cosmochimica Acta 124, 170–189.
Selene, C.H., Chou, J., 2003. Hydrogen sulfide: human health aspects. Concise International Chemical Assessment Document 53. World Health Organization.
Stefánsson, A., Arnórsson, S., 2002. Gas pressures and redox reactions in geothermal fluids in Iceland. Chem. Geol. 190, 251–271.
Stefánsson, A., Arnórsson, S., Gunnarsson, I., Kaasalainen, H., Gunnlaugsson, E., 2011. The geochemistry and sequestration of H2S into the geothermal system at Hellisheidi: Iceland. J. Volcanol. Geotherm. Res. 202, 179–188.
Stefánsson, A., Keller, N.S., Gunnarsson-Robin, J., Ono, S., 2015. Multiple sulfur isotope systematics of Icelandic geothermal fluids and the source and reactions of sulfur in volcanic geothermal systems at divergent plate boundaries. Geochimica et Cosmochimica Acta 165, 307–323.
Stephens, F.B., Hill, J.H., Phelps Jr., P., 1980. State-of-the-art Hydrogen Sulfide Control for Geothermal Energy Systems: 1979. California Univ., Lawrence Livermore Lab., Livermore (USA).
Takahashi, K., Kuragaki, M., 2000. Yanaizu-Nishiyama geothermal power station H2S abatement system. In: Proceedings of the World Geothermal Congress 2000. Kyushu-Tohoku, Japan. pp. 719–724.
Tester, J.W., Worley, W.G., Robinson, B.A., Grigsby, C.O., Feerer, J.L., 1994. Correlating quartz dissolution kinetics in pure water from 25 to 625 °C. Geochimica et Cosmochimica Acta 58, 2407–2420.
Thompson, R.C., 1992. Structural stratigraphy and intrusive rocks at The Geysers geothermal field. Monogr. Geysers Geother. Field 17, 59–63.
Torio-Henríquez, E., 2007. Petrography and mineral alteration in Berlin geothermal field. In: Proceedings of the 32nd Workshop on Geothermal Reservoir Engineering. Stanford University, Stanford, California, January 22–24, SGP-TR-183.
World Environment Center, 1994. Technical Assessment on H2S Gas Abatement Systems at California Energy's Coso Geothermal Power Plants. U.S. Agency for International Development.
World Health Organization, 2000. Air Quality Guidelines for Europe, European Series No. 91.

Appendix III

Appendix III

Towards green energy: Co-mineralization of carbon and sulfur in geothermal reservoirs

Chiara Marieni[1,2], Jan Přikryl[1], Edda Sif Aradóttir[2], Ingvi Gunnarsson[2] and Andri Stefánsson[1]

[1]Institute of Earth Sciences, University of Iceland, Sturlugata 7, 101 Reykjavik, Iceland

[2]Reykjavík Energy, Bæjarháls 1, 110 Reykjavík, Iceland

International Journal of Greenhouse Gas Control

(submitted)

Highlights:

- CO_2 and H_2S mineralization within geothermal reservoir is geochemically feasible.
- Carbonates and sulfides form within basaltic to silicic reservoirs in few days.
- This abatement method can be scaled up worldwide and over at least 50 years.
- The re-injection of CO_2 and H_2S is five time cheaper the H_2S-only abatement systems.

Keywords: Geothermal energy; CO_2 and H_2S emissions; Sustainability

Abstract

Geothermal fluid utilization is considered one of the green energy sources. Yet, mitigation strategies must be applied to reduce the associated pollutants like carbon dioxide (CO_2) and toxic hydrogen sulfide (H_2S) emissions. One suggested method is the re-injection of the two gases back into the geothermal reservoir wherein carbon and sulfur are expected to mineralize naturally for a long-term underground storage. However, CO_2 and H_2S mineralization rates for natural systems are not well defined. To address the feasibility of such sequestration, experiments were conducted at 250°C for several reservoir rock types, ranging from basaltic to silicic. Analysis of solution composition and secondary mineralogy confirmed the precipitation of Fe-Ca carbonates and Fe sulfide for all the rocks within days. The measured mineralization rates indicate that ~0.2-0.5 t of CO_2, and ~0.03-0.05 t of H_2S can be sequestrated annually per cubic meter of rock, depending on reservoir lithology and surface area. Calculations show that a total rock sequestration capacity of ~0.03 km^3 would be sufficient to store the annual world CO_2 and H_2S geothermal emissions. These findings indicate efficient abatement of CO_2 and H_2S at field conditions, confirming the strategy applicability for at least the typical 50 years-lifetime of geothermal power plants.

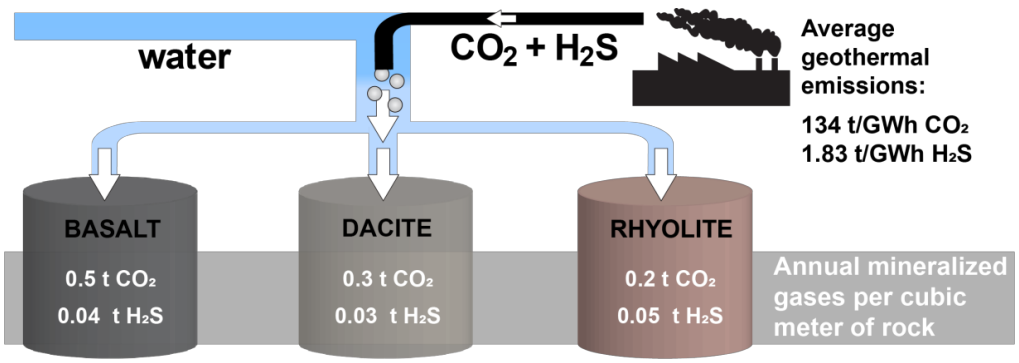

1 Introduction

The increasing level of carbon dioxide (CO_2) in the atmosphere is considered to cause climate change (IPCC, 2014). The fraction of anthropogenic CO_2 in the atmosphere amounts to ~30% (~900 Gt) (Hofmann et al., 2009), with geothermal exploitations contributing only ~9 Mt/yr through more enhanced natural discharges (Bertani, 2016; Fridriksson et al., 2016). However, besides CO_2, geothermal activity emits hydrogen sulfide (H_2S), which is toxic and life-threatening when above 100 ppm (ATSDR, 2016), and commonly contains pollutant elements such as arsenic, boron, and mercury (Barbier, 2002). If present at high concentrations in the geothermal fluids, these chemicals represent a major environmental concern once released to the environment at surface (e.g., Hansell and Oppenheimer, 2010; Kristmannsdóttir and Ármannsson, 2003). One developing method to reduce the geothermal CO_2 and H_2S emissions is the re-injection of the gases together with condensed steam and/or waste water back into the reservoir where natural fluid-rock interactions are considered to lead to mineralization of secondary carbonates and sulfides, respectively (Aradóttir et al., 2015). This option offers the

advantages of avoiding major modifications on the power plants, costly CO_2 and H_2S separation steps, and generation of waste by-products while harvesting the heat energy.

A number of laboratory and field investigations have focused on the CO_2 sequestration potential of mafic rocks, demonstrating its potential and the associated environmental and societal benefits (e.g., Galeczka et al., 2014; Gysi and Stefánsson, 2012; Matter et al., 2016; Matter et al., 2007; McGrail et al., 2016; Rosenbauer et al., 2012; Schaef et al., 2009; Shibuya et al., 2013). The results highlight the feasibility of long-term underground storage of greenhouse gas in a solid state. On the other hand, very few studies have considered the H_2S abatement through geological storage (e.g., Bachu and Gunter, 2005), and even less through mineralization at geothermal conditions (Přikryl et al., 2018; Stefánsson et al., 2011). Technical difficulties encountered during re-injection tests in the field, such as gas breakthrough and well casing corrosion, have led to the development of other abatement technologies (Sanopoulos and Karabelas, 1997). For instance, a more conventional and usually expensive approach commonly in use to reduce H_2S emissions from geothermal power plants is oxidation to form elemental sulfur or sulfuric acid (Rappold and Lackner, 2010; Rodríguez et al., 2014). However, the recent successful H_2S re-injection into the basaltic reservoir at the Hellisheiði power plant, SW Iceland, has put this option under the spotlight (Gunnarsson et al., 2015). Nonetheless, considerable uncertainties remain relating to the co-mineralization potential, especially the effects of H_2S mineralization on the CO_2 sequestration, chemical variability of host-rocks, and reservoir capacity. To address these issues, we investigate the geochemical applicability of re-injection of CO_2 and H_2S into geothermal reservoirs by conducting experiments on a suite of typical host-rocks and the potentials of such sequestration method for geothermal systems worldwide.

2 Materials and Methods

2.1 Solid material

Three volcanic glasses were used to account for the compositional variability of the main common rock types associated with geothermal systems worldwide: basaltic glass (BG) (Stapafell Mountain, SW Iceland); dacitic glass (DG) (Hekla volcano, S Iceland); and rhyolitic glass (RG) (Askja caldera, NE Iceland) (Oelkers and Gislason, 2001; Wolff-Boenisch et al., 2004). The solid material was ground, and then sieved to obtain a 45–125 μm size fraction, which was then used in the experiments. The material was cleaned ultrasonically in deionized water and acetone to obtain grains with smooth surfaces and no fine particles (<10 μm) (Fig. 1).

The surface morphology, before and after the experiments, and the secondary mineralogical composition of the solid products were analysed using scanning electron microscopy (LEO Supra™ 25 FE-SEM) and standard energy-dispersive spectrometry (EDS). All chemical analysis was performed using an acceleration voltage of 20 kV, a beam current of 200 pA, and a beam diameter of 1-2 μm. Natural and synthetic minerals and glasses were used as standards to check for potential drift.

The bulk chemical composition and the physical characterisation of all the glasses pre-experiment are summarised in Table 1.

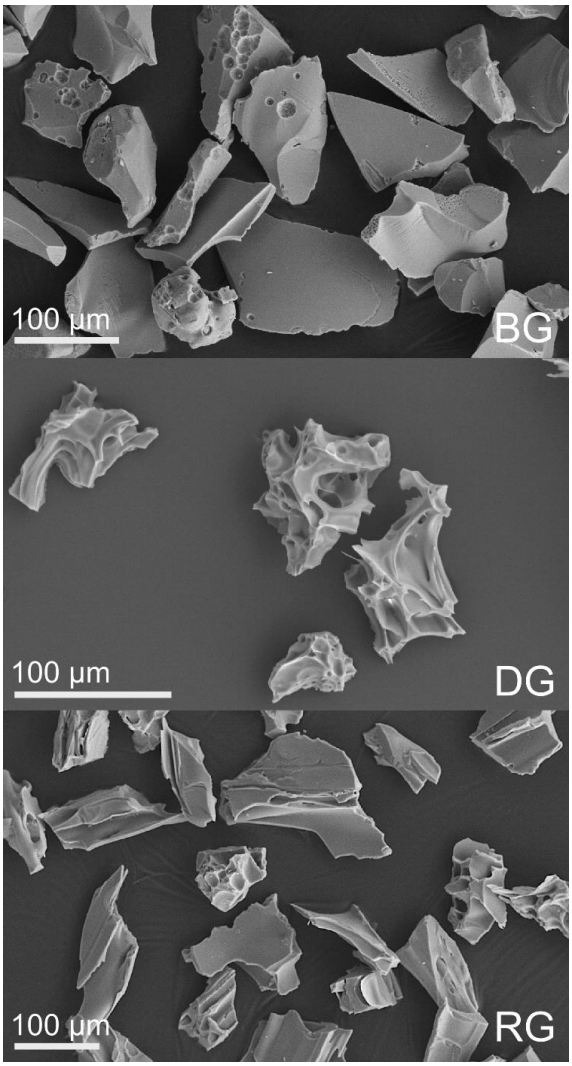

Figure 1. *Scanning electron microscope (SEM) images of pre-experiment solid grains of basaltic (BG), dacitic (DG) and rhyolitic (RG) glass.*

ID	BG-Stapafell	RG-Askja 1875	DG-Dacite
	A-BG1	B-RG1	C-DG1
Rock density (g/cm^3)	2.851 [1]	2.452 [2]	2.512 [2]
A_{BET} (cm^2/g)	23000 [3]	14100 2	12100 [2]
Ageo (cm^2/g)	250 [3]	312 [2]	305 [2]
Roughness factor	92	45	40
wt. %	[3]	[2]	[2]
SiO_2	48.12	69.28	66.01
TiO_2	1.564	0.9	0.42
Al_2O_3	14.62	12.42	14.65
Fe_2O_3	1.11	2.48	2.14
FeO	9.82	2.09	3.81
MnO	0.191	0.1	0.18
MgO	9.08	0.97	0.39
CaO	11.84	2.81	3.21
Na_2O	1.97	3.74	4.72
K_2O	0.29	2.21	2.07
P_2O_5	0.195	0.19	0.1
TOT	98.8	98.89	98.67

[1] *Galeczka et al., 2014*

[2] *Wolff-Boenisch et al., 2004-a*

[3] *Oelkers and Gislason, 2001*

Table 1. *Glass densities, together with BET specific surface areas (A_{BET}), geometric surface areas (A_{geo}), roughness factor (A_{BET}/A_{geo}) and chemical compositions.*

2.2 Solution preparation and analysis

The initial experimental solution contained ~15.5 and ~2 mmol/l of dissolved inorganic CO_2 ($CO_2 = [CO_2]+[HCO_3^-]+[CO_3^{2-}]$) and H_2S, respectively, and had pH ~7 (Table 2). They were made from HCl (Sigma–Aldrich® 37%), Na_2CO_3 (Sigma–Aldrich®), and Na_2S (Sigma–Aldrich®) in N_2-deoxygenated deionized water (Millipore™). A fresh solution was made every two to three days to avoid oxidation of H_2S. For all experiments, the inlet solution was undersaturated with respect to sulfide and carbonate minerals.

Samples of inlet and outlet solutions were collected to determine their chemical composition. Samples for major dissolved elements (Si, Ti, Na, K, Mg, Ca, Fe, Al, Cl) determination were first filtered through 0.2 μm, then acidified to 1% HNO_3 (Suprapur®), and analyzed using ICP-OES. Samples for SO_4 analysis were treated with 2% Zn-acetate (1 ml to 100 ml sample) in order to precipitate all the residual H_2S as ZnS(s), which was filtered off prior to measuring SO_4 using IC. Determination of pH, CO_2, and H_2S was carried out on un-treated samples using a combination of a pH electrode and a pH meter, modified alkalinity titration, and precipitation titration using Hg-acetate, respectively (Arnórsson et al., 2006; Stefánsson et al., 2007). The analytical precision at the 95% confidence level based on repeated analysis of an internal standard was ~1-10% for different elements. Based on duplicated determination, the analytical precision of CO_2 and H_2S concentrations was <3%, and pH was ±0.05 pH units.

#	Rock	Experimental duration	Rock mass	pH/25°C	CO_2 [a]	H_2S
		days	g		mM	mM
A-BG1	Basaltic glass	8	37	7.12	15.4	2.15
B-RG1	Rhyolitic glass	7	21	7.13	15.8	1.71
C-DG1	Dacitic glass	7	12	7.09	15.8	2.42

[a] CO_2 = total dissolved carbon

Table 2. *Summary of the initial experimental conditions.*

2.3 Experimental setup

The re-injection of CO_2 and H_2S into geothermal reservoirs and subsequent mineralization was studied using flow-through column experiments at 250 °C and 55 bar to reproduce typical geothermal conditions. A schematic illustration of the pressurized reactor system is shown in Fig. 2. All wetted parts of the experimental apparatus were made of inert material, including PEEK, titanium and Inconel. The CO_2-H_2S-rich solutions were pumped into the 29 cm-long reactor at flow rates of 0.5 ml/min using a HPLC pump (Chromotech®), and the pressure was controlled at the end of the line using a back pressure regulator (Coretest). The reactor was heated to the target temperature (±5°C) using a heating mantle and a temperature controlling system. The outlet fluid was cooled to room temperature with the help of a cooling jacket placed between the reactor and the back pressure regulator. Samples of the outlet solutions were collected at the low-pressure end of the back-pressure regulator. Samples of the inlet solutions were collected directly from the inlet solution bottle. The initial experimental conditions are summarized in Table 2.

The solid sample post experiments were carefully collected pushing the rock slurry out of the reactor from top to bottom, with the help of a cylindrical bar and spatula. On the base of the total reactor length, four sections of ~7 cm of length were separately stored to study the dissolution-precipitation products as a function of time and space. The material was then dried at 50 °C, and part of it mounted on a sample holder and gold-coated for SEM-EDS analysis.

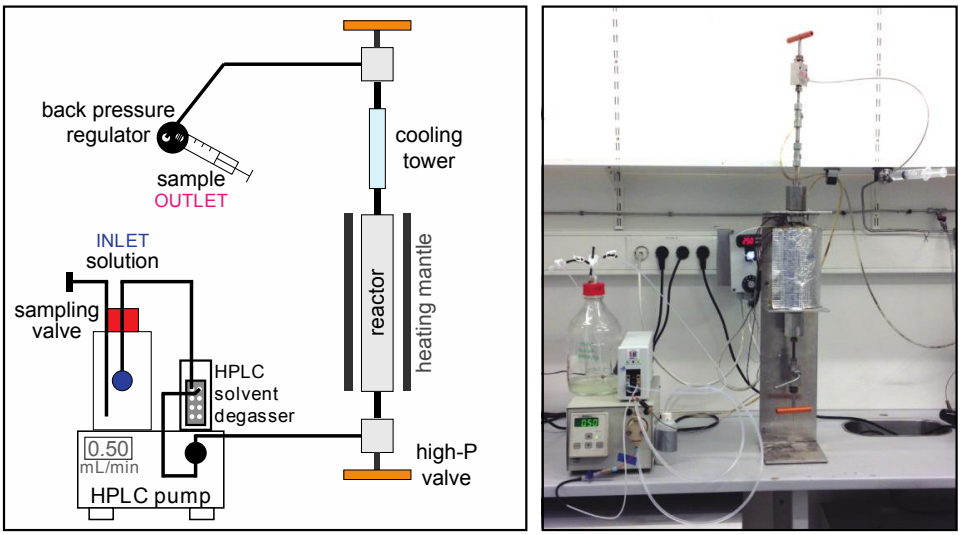

Figure 2. *Schematic representation of the experimental setup used for the flow-through column experiments.*

2.4 Sequestration rates

The steady-state experimental mineralization rates $\boldsymbol{r_i}$ (log mol/m^2/s) were calculated for H_2S and CO_2 following:

$$r_i = \frac{Q \times \Delta_i}{A \times M} \quad (1)$$

where Q stands for flow rate, Δ_i represents the concentration difference of CO_2 or H_2S between inlet and outlet solutions, A is the initial specific surface area, and M is the initial mass of ground particles inside the reactor. In this study, both BET specific surface areas (A_{BET}), and computed geometric surface areas (A_{geo}) were considered.

To scale up the obtained laboratory mineralization rates to field conditions, the equivalent steady-state sequestration rates (sr_i) of CO_2 and H_2S for natural systems were calculated from the relationship:

$$sr_i = r_i * A_{field} * \rho \quad (2)$$

where r_i is the experiment mineralization rate of CO_2 or H_2S either normalized to geometric surface area, A_{field} is the rock surface area of natural geothermal systems (m^2/g), and ρ is the respective rock density (g/m^3). Field sequestration rates were normalized only to geometric surface area because were found to be more consistent than normalized rates to BET, which are usually considered to overestimate the true reactive surface area between fluids and rocks (e.g., Anbeek 1992; Brantley and Chen, 1995; Brantley and Mellott, 2000; Gislason and Oelkers, 2003; Lüttge and Arvidson, 2008; Přikryl et al., 2017; Wolff-Boenisch et al., 2004).

3 Results

3.1 Solution chemistry

The results of the chemical composition of the experimental solutions are given in Table 3. For all rock types, the pH increased from neutral in the inlet solutions to more alkaline in the outlet solutions. In the case of BG, the first measured outlet pH was 4.5 due to the presence of non-deoxygenated distilled water within the reactor, initially used to compact the powder. This water triggered an initial acidification of the inlet solution, but in less than 4 hours the outlet pH was re-established at 7. On this base, no distilled water was used for the other experimental runs. For basaltic (BG) and intermediate (DG) rocks the outlet pH increased with experimental duration to >8, whereas for silicic rocks (RG) the pH was relatively stable between 7.3 and 7.9 throughout the experiments (Fig. 3). The accompanied decrease of CO_2 and H_2S was estimated from the difference between the inlet and outlet solution concentrations (Fig. 3). The CO_2 and H_2S concentration difference between the inlet and outlet reached 52 and 36% for basalt (BG), 17% and 12% for intermediate rock (DG), and 15% and 40% for acidic rock (RG), respectively.

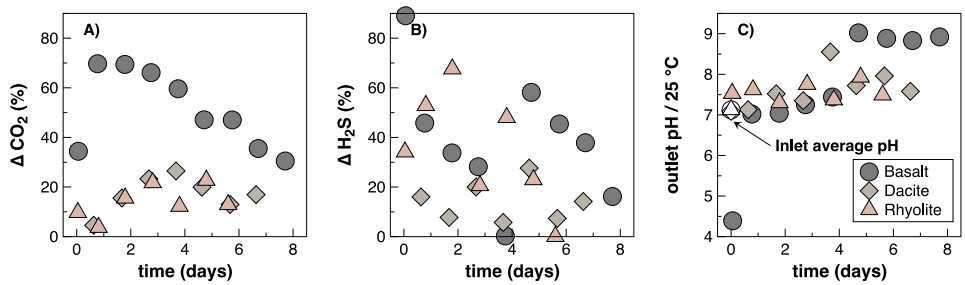

Figure 3. *CO_2 (A) and H_2S (B) sequestration capabilities into geothermal reservoirs based on the inlet and outlet experimental solution composition ($\Delta\% = c_{inlet}$-c_{outlet}/c_{inlet}*100), and pH (C) values of the outlet solutions.*

ID	Runtime	Flow rate	Inlet solution						Outlet solution											
			pH/25°C	H_2S	CO_2	Cl	Na	SO_4	pH/25°C	H_2S	CO_2	Cl	SiO_2	Al	Ca	Fe	Mg	K	Na	SO_4
	hours	ml/min		mM	mM	mM	mM	mM		mM	mM	mM	mM	mM	mM	mM	mM	mM	mM	mM
A-BG1-1	1.5	0.50	7.03	2.28	14.52	20.98	32.08	0.01	4.39	0.25	9.52	20.76	13.83	0.04	0.32	0.0039	0.0118	0.43	21.41	0.04
A-BG1-2	18.5	0.52	7.21	2.49	15.59	20.75	32.20	0.01	7.02	1.35	4.72	21.90	9.24	0.15	0.13	0.0001	0.0004	0.75	24.70	0.03
A-BG1-3	42.7	0.50	7.14	2.37	15.46	20.94	32.20	0.02	7.04	1.57	4.73	21.28	6.69	0.16	0.19	<0.0001	<0.0002	0.74	23.87	0.03
A-BG1-4	66.0	0.52	7.03	2.20	14.01	20.93	32.43	0.02	7.25	1.58	4.75	21.36	5.30	0.15	0.19	<0.0001	<0.0002	0.37	23.89	0.02
A-BG1-5	90.0	0.50	7.14	1.81	15.57	21.30	32.48	0.01	7.44	1.81	6.29	21.44	5.09	0.19	0.09	<0.0001	<0.0002	0.14	25.35	0.02
A-BG1-6	113.0	0.52	7.11	2.49	14.21	21.60	32.43	0.02	9.02	1.04	7.52	21.17	5.35	0.27	0.02	<0.0001	<0.0002	0.09	28.65	0.03
A-BG1-7	138.0	0.50	7.00	2.29	15.53	21.26	32.39	0.02	8.89	1.25	8.22	21.25	4.90	0.25	0.01	<0.0001	<0.0002	0.07	30.30	0.03
A-BG1-8	161.0	0.50	7.19	2.00	16.22	21.44	32.51	0.02	8.83	1.24	10.46	21.38	4.51	0.27	0.01	<0.0001	<0.0002	0.06	31.34	0.03
A-BG1-9	185.0	0.49	7.25	1.36	15.20	21.37	32.53	0.02	8.92	1.14	10.56	21.35	4.06	0.31	0.01	<0.0001	<0.0002	0.05	31.72	0.08
2σ [a]						0.04	0.05	0.03				0.04	0.03	0.04	0.03	0.0500	0.0800	0.04	0.05	0.03
B-RG1-1	15.0	0.48	7.09	2.05	15.20	21.19	32.58	0.03	7.53	1.35	13.72	20.95	11.71	0.21	0.01	0.0002	0.0007	0.96	32.22	0.02
B-RG1-2	40.0	0.52	7.02	1.76	15.09	21.61	33.23	0.02	7.62	0.83	14.52	20.88	13.09	0.14	0.005	<0.0001	<0.0002	1.11	32.00	0.02
B-RG1-3	64.0	0.52	7.16	1.92	14.76	21.42	32.74	0.02	7.30	0.62	12.46	20.91	14.78	0.12	0.004	<0.0001	<0.0002	1.26	30.25	0.05
B-RG1-4	88.0	0.50	7.10	2.04	16.46	21.40	33.18	0.02	7.75	1.62	12.88	21.11	13.59	0.10	0.01	<0.0001	<0.0002	1.26	31.22	0.03
B-RG1-5	111.0	0.50	7.11	1.77	14.62	21.18	33.07	0.02	7.37	0.92	12.84	20.87	12.91	0.11	0.01	<0.0001	<0.0002	1.11	30.76	0.03
B-RG1-6	136.0	0.50	7.05	1.35	16.25	21.34	32.93	0.02	7.93	1.04	12.56	21.14	10.90	0.16	0.01	0.0002	<0.0002	1.05	31.39	0.03
B-RG1-7	159.0	0.50	7.37	0.53	14.20	21.03	32.97	0.02	7.49	0.53	12.36	20.83	12.96	0.13	0.00	<0.0001	<0.0002	1.01	30.87	0.04
2σ [a]						0.06	0.09	0.03				0.06	0.03	0.05	0.05	0.0700	0.0800	0.03	0.09	0.03
C-DG1-1	1.0	0.50	6.68	2.51	17.35	21.89	33.43	0.01	7.13	2.11	16.55	22.31	4.40	0.63	<0.001	0.0015	<0.0002	1.50	33.34	0.05
C-DG1-2	19.5	0.50	7.15	2.46	16.31	21.89	32.84	0.01	7.52	2.27	13.76	22.55	11.25	0.08	<0.001	0.0290	0.0055	1.30	35.02	0.02
C-DG1-3	43.0	0.50	6.95	2.21	15.68	21.53	32.93	0.02	7.35	1.77	12.02	22.63	10.28	0.09	<0.001	<0.0001	<0.0002	1.17	32.99	0.03
C-DG1-4	67.5	0.50	7.08	2.45	16.59	21.92	33.34	0.02	8.55	2.31	12.19									
C-DG1-5	91.3	0.50	7.08	2.23	15.52	21.68	33.22	0.02	7.72	1.61	12.43	25.03	8.52	0.10	<0.001	<0.0001	<0.0002	0.72	39.84	0.03
C-DG1-6	115.0	0.50	7.00	2.52	12.53	21.75	33.71	0.02	7.96	2.33	10.91	23.32	12.23	0.04	0.01	<0.0001	<0.0002	0.77	34.39	0.04
C-DG1-7	134.5	0.50	7.29	2.54	16.03	21.67	33.36	0.02	7.58	2.18	13.32	22.76	8.21	0.13	<0.001	<0.0001	<0.0002	0.39	35.24	0.03
C-DG1-8	163.0	0.50	7.48	2.70	16.96	19.40	33.29	0.01	7.93	2.51	16.19	20.09	5.65	0.36	<0.001	<0.0001	<0.0002	0.21	35.79	0.02
2σ [a]						0.03	0.08	0.03				0.04	0.01	0.03	0.05	0.0400	0.0400	0.02	0.06	0.03

[a] Analytical uncertainity based on repeated analysis of reference sample GYG13 (for ICP data) and internal standard (for IC SO_4 data)

Table 3. *Chemical composition of the experimental outlet solutions.*

3.2 Secondary mineralogy

The secondary minerals identified within the alteration assemblages included carbonates, sulfides, feldspars and epidote (Fig. 4). In all the host rocks, the only secondary mineral containing sulfur was pyrite, which exhibits euhedral crystals of ~1-3 μm. No anhydrite ($CaSO_4$) or other sulfate minerals were observed. Iron-enriched solid solution of siderite ($Fe_{\leq 0.05}$) and calcite ($Ca_{\geq 0.95}$) formed preferentially in the basaltic rocks (BG), whereas calcite end-member solid solution prevailed within silicic rocks (RG) and intermediate rocks (DG). Iron-enriched solid solution of carbonates was present as tabular crystals up to ~10 μm, and sometimes in the shape of massive conglomerates. Calcite grains ranged in size from ~1 to 20 μm, with sub to euhedral crystal habit. The presence of albite and epidote confirmed the achievement of silicate saturation state during the experimental runs. Albite was visible in all the post-experiment materials, with up to ~20 μm large crystals. Epidote was detected associated with intermediate (DG) and silicic rocks (RG), shaped into ~5-15 μm big, elongated crystals.

The distribution of secondary minerals during the fluid-rock interaction, obtained by point counting through secondary electron microscopy, is shown schematically in Fig. 5 as a function of four spatial stages. Carbonates and sulfide were most abundant at the inlet side of the reaction column, and decreased with distance along the fluid flow. This demonstrate a rapid solution saturation with respect to carbon- and sulfur-bearing minerals during the initial stage of fluid-rock interactions. On the other hand, albite and epidote were mostly located in the outlet side of the reaction column, suggesting a lower initial saturation state. Overall, considering the whole reactor, the suggested order of abundance of the main secondary minerals is carbonates > pyrite > albite > epidote.

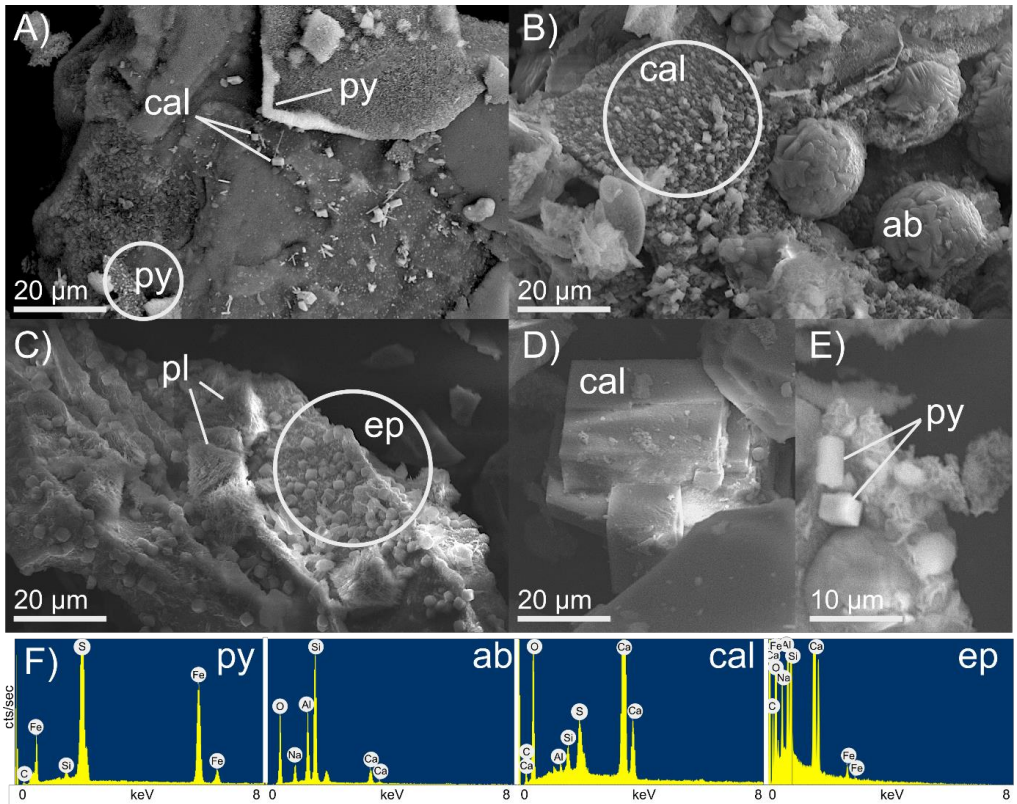

Figure 4. *SEM images of typical secondary phases observed within the post-experiment solid material.* ***A)*** *pyrite (py) precipitation on basaltic glass with minor carbonates;* ***B)*** *secondary calcite (cal) with blocky albite (ab) on the grain of dacitic glass;* ***C)*** *epidote (ep) with plagioclase (pl) on rhyolitic glass;* ***D)*** *example of ~20 µm big crystal of calcite;* ***E)*** *example of ~3 µm big crystals of pyrite; and* ***F)*** *EDS spectra of pyrite, albitic plagioclase, calcite, and epidote.*

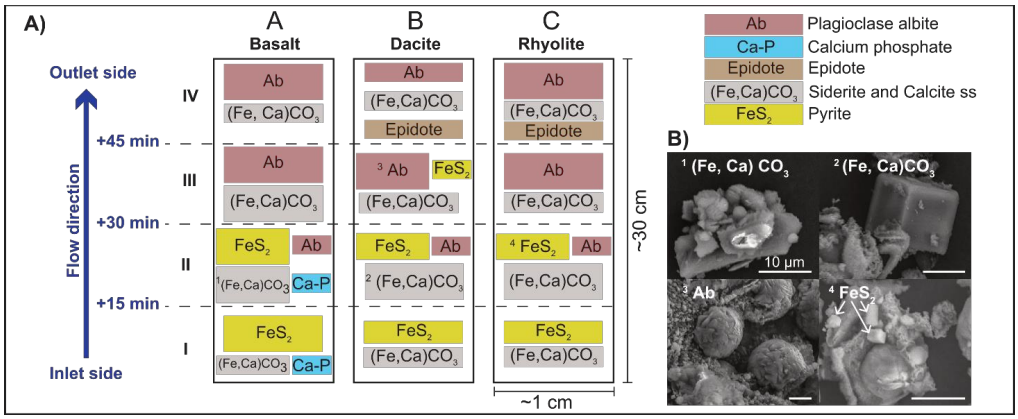

Figure 5. A) *Schematic summary of the mineral formation sequence along the reactor column, for all the experimental runs. Mineral box size is proportional to volumetric abundance amongst secondary phases.* ***B)*** *SEM images showing example of typical secondary minerals formed during the experiments as a function of reaction distance.*

4 Discussion

4.1 CO_2-H_2S mineralization rates

The steady-state CO_2 and H_2S mineralization rates (r_i) were obtained from the experimental results, normalized both to BET and geometric surface area (Eqn. 1). The CO_2 rates were calculated based on the observed carbonate mineral composition ($Ca_{0.95}Fe_{0.05}CO_3$). The results are listed in Table 4. For the CO_2 mineralization, the rock types with fastest rate were basaltic and intermediate rocks, both showing similar potential. For the H_2S mineralization rates, the opposite was observed with the fastest rate for silicic rocks (RG), despite its low content in Fe. The CO_2 and H_2S mineralization rates for volcanic rocks obtained here were observed to be faster than for sedimentary rocks (Benson and Cole, 2008; Gunter et al., 1997). Moreover, the H_2S mineralization rates obtained here are comparable with previous results at similar pH, and temperature, for basaltic conditions (Přikryl et al., 2018). This suggests that carbonate formation does not significantly affect the mineralization rate of sulfide.

Considerable differences were observed between the mineralization rates normalized to BET and geometric surface area. However, given the BET overestimation of true reactive surface area, the rate estimations normalized to geometric surface areas are considered to be more consistent with the dissolution behavior of natural glass, and were used for further calculations at field conditions. It should also be pointed out that the rates obtained here are related to optimal mineralization conditions with freshly ground material, high porosity (~70%), and very extensive particle surface area available for fluid-rock interactions. Geothermal reservoir may instead be characterized by already altered rocks and lower porosity (Aradóttir et al., 2012; Gunnarsson et al., 2011), and reactive surface areas associated to fracture networks (Watanabe and Takahashi, 1995).

The sulfides and carbonates mineralization was observed to occur preferentially on the inlet side of the flow-through column with more complex aluminum silicates forming at the outlet side. This is in agreement with the evolution of the solution composition. The divalent cations are leached from the rocks upon reactions with the CO_2 and H_2S-rich fluids, resulting in the initial carbonate and sulfide mineral saturation and their formation. At this initial stage many common Ca, Mg and Fe containing aluminum silicates are undersaturated and do not form. However, with progressive reactions along the flow-path, the solution pH increases as well as the elemental concentrations in solutions, eventually resulting in aluminum silicate mineral saturation and formation of, for example, albite and epidote. Previous studies have demonstrated how the uptake of divalent cations like Ca^{2+}, Mg^{2+} and Fe^{2+} by such aluminum silicates may reduce the rock capacity of mineralizing CO_2 and H_2S into carbonates and sulfides (e.g., Gysi and Stefánsson, 2012; Hellevang et al. 2017; Přikryl et al., 2018; Stefánsson et al., 2011; Wolff-Boenisch and Galeczka, 2018).

#	Runtime	Experiment mineralization rate - geo		Experiment mineralization rate - BET	
		$CO_{2\ geo}$	$H_2S_{\ geo}$	$CO_{2\ BET}$	$H_2S_{\ BET}$
	days	log $r_{i\ geo}$ (mol/m^2/s)		log $r_{i\ BET}$ (mol/m^2/s)	
Basalt					
A-BG1-outlet1	0.06	-7.3	-7.7	-9.3	-9.7
A-BG1-outlet2	0.77	-7.0	-8.0	-9.0	-9.9
A-BG1-outlet3	1.78	-7.0	-8.1	-9.0	-10.1
A-BG1-outlet4	2.75	-7.1	-8.2	-9.0	-10.2
A-BG1-outlet5	3.75	-7.1	-10.3	-9.0	-12.3
A-BG1-outlet6	4.71	-7.2	-7.9	-9.2	-9.8
A-BG1-outlet7	5.75	-7.2	-8.0	-9.1	-10.0
A-BG1-outlet8	6.71	-7.3	-8.2	-9.2	-10.1
A-BG1-outlet9	7.71	-7.4	-8.7	-9.4	-10.7
*As-s (from outlet 5)**		-7.2 ± 0.1	-8.2 ± 0.4	-9.2 ± 0.1	-10.2 ± 0.4
Rhyolite					
B-RG1-outlet1	0.63	-7.7	-8.1	-9.4	-9.7
B-RG1-outlet2	1.67	-8.1	-7.9	-9.8	-9.6
B-RG1-outlet3	2.67	-7.5	-7.8	-9.2	-9.4
B-RG1-outlet4	3.67	-7.3	-8.3	-9.0	-9.9
B-RG1-outlet5	4.63	-7.6	-8.0	-9.3	-9.6
B-RG1-outlet6	5.67	-7.3	-8.4	-8.0	-10.1
B-RG1-outlet7	6.63	-7.6	-11.3	-9.3	-13.0
*As-s (without outlet 7)**		-7.5 ± 0.2	-8.0 ± 0.2	-9.2 ± 0.2	-9.7 ± 0.2
Dacite					
C-DG1-outlet1	0.04	-7.7	-8.0	-9.3	-9.6
C-DG1-outlet2	0.81	-7.2	-8.4	-8.8	-10.0
C-DG1-outlet3	1.79	-7.1	-8.0	-8.7	-9.6
C-DG1-outlet4	2.81	-7.0	-8.5	-8.6	-10.1
C-DG1-outlet5	3.8	-7.2	-7.9	-8.8	-9.5
C-DG1-outlet6	4.79	-7.4	-8.4	-9.0	-10.0
C-DG1-outlet7	5.6	-7.2	-8.1	-8.8	-9.7
C-DG1-outlet8	6.79	-7.8	-8.4	-9.4	-9.9
*As-s(from outlet 6)**		-7.4 ± 0.3	-8.2 ± 0.2	-9.0 ± 0.3	-9.8 ± 0.2

* Average steady-state calculated from Si concentrations

Table 4. *CO_2 and H_2S experiment mineralization rates normalized to flow rate, and both BET specific surface area and geometric surface area. Based on SEM-EDS analysis, the carbonate composition is assumed to be $Ca_{0.95}Fe_{0.05}CO_3$.*

4.2 CO_2-H_2S sequestration rates for natural geothermal systems

One developing method to reduce the geothermal CO_2 and H_2S emissions is the re-injection of the gases into the geothermal reservoir where they are potentially mineralized (Aradóttir et al., 2015). Based on the experimental mineralization rates, the rock geometric surface area of natural geothermal systems and rock density, the field scale

CO_2 and H_2S sequestration rates were estimated (Eqn. 2). The field geometric surface areas ($A_{field,geo}$) have been set to 0.002 m^2/g (Aradóttir et al., 2012) for all the rock types. The scaled up field mineralization rates resulted in the range of ~200 to ~500 $kg/m^3/yr$ for CO_2, and of 30 to ~50 $kg/m^3/yr$ for H_2S (Table 5). Based on the SEM-EDS analysis on the composition of the secondary phases, these rates on CO_2 and H_2S led to an estimated mineralization of ~120-300 $kg/m^3/yr$ of carbonates, and ~50-85 $kg/m^3/yr$ of pyrite, respectively. Further calculations based on the initial rock stoichiometry shows that the annual estimated carbonates approached the maximum stoichiometric mass of secondary minerals that can precipitate per m^3 of rock (Table 5). The fact that each m^3 of rock is depleted in metallic cations around one year suggests that the total sequestration volumes must be bigger than this. However, the annual field scale sequestration rates, extrapolated from laboratory data, propose valuable estimations, which can be used to calculate the sequestration capacity, and to assess the feasibility of CO_2 and H_2S sequestration into natural geothermal systems.

		Field sequestration rate			Field secondary mineral rates		
Rock	**Type**	log $sr_{i\ geo}$	$sr_{i\ geo}$	**Type**	geo	stoichiometry (Fe^{2+})	stoichiometry (Fe_{tot})
		$mol/m^3/s$	$kg/m^3/yr$		$kg/m^3/yr$	kg/m^3	kg/m^3
Basalt	CO_2	-3.5	483	carbonate	302	639	639
	H_2S	-4.4	39	pyrite	64	468	515
Rhyolite	CO_2	-3.9	194	carbonate	121	130	130
	H_2S	-4.3	51	pyrite	85	86	177
Dacite	CO_2	-3.7	270	carbonate	169	153	153
	H_2S	-4.6	30	pyrite	50	160	241

Table 5. *Sequestration rates calculated for field scenarios, together with field secondary mineral formation rates. Based on SEM-EDS analysis, the carbonate composition is assumed to be* $Ca_{0.95}Fe_{0.05}CO_3$*. For comparison, maximum amount of secondary minerals formed through rock stoichiometry are listed as well.*

4.3 CO_2 and H_2S emissions and sequestration capacities worldwide

In this study the CO_2 and H_2S emissions from geothermal power plants worldwide were estimated. The CO_2 and H_2S emission rates were obtained in terms of emissions per energy produced (g/kWh) per country, and then multiplied by the averaged production of geothermal energy per year (GWh/yr) (Bertani, 2016). The CO_2 emissions are on average 134 g/KWh, which is in agreement with the previously proposed 122 g/KWh (Fridriksson et al., 2016) based on a survey involving emissions from only the ~50% installed capacity. The H_2S emissions, proposed here for the first time, are on average 1.83 g/kWh. Both average values were calculated for 97% of the geothermal capacity installed

worldwide (Bertani, 2016). The current world total emissions from geothermal activity, before any abatement system, were estimated to be ~10 Mt of CO_2 per year, and ~0.2 Mt/yr of H_2S, with peaks in Italy, Turkey, U.S., Iceland, Mexico, and New Zealand (Table 6).

Using the field sequestration CO_2 and H_2S mineralization rates ($sr_{i\ geo}$) and the gas emissions (Q_{gas}), the sequestration capacity (SQ_i) were calculated according to

$$SQ_i = Q_{gas\,i}/sr_{i\,geo} \quad (3)$$

The results are listed for each country in Table 6. Based on these estimations, a geothermal field with sequestration capacity of $3x10^{-2}$ km^3 would be sufficient to store the annual world CO_2 and H_2S geothermal emissions, and 1.6 km^3 to store the global CO_2 and H_2S geothermal production over an average power plant lifetime of 50 years. Furthermore, Table 6 summarizes the sequestration capacities for specific geothermal power plants in Mexico, New Zealand, Iceland, and El Salvador. In the case of Wairakei power plant (New Zealand), only $4x10^{-4}$ km^3 of host rock would be needed to sequester through re-injections into andesite all the CO_2 (~78 kt) and H_2S (~0.5 kt) produced in one year, and $2x10^{-2}$ km^3 through all the lifetime of the plant.

The obtained sequestration capacities are based on experimental conditions and do not take into account the variability of natural systems, for example in porosity, permeability, and reactive surface area. Moreover, natural rocks may already be altered to variable degrees. However, the CO_2 and H_2S sequestration into geothermal systems is considered a feasible abatement method in terms of geochemistry and gas emissions as it may rapidly convert the global geothermal emissions into solid minerals, throughout the lifetimes of a geothermal power plants, and within reasonable reservoir volumes (Fig. 6) even when stoichiometric limitation would be accounted for.

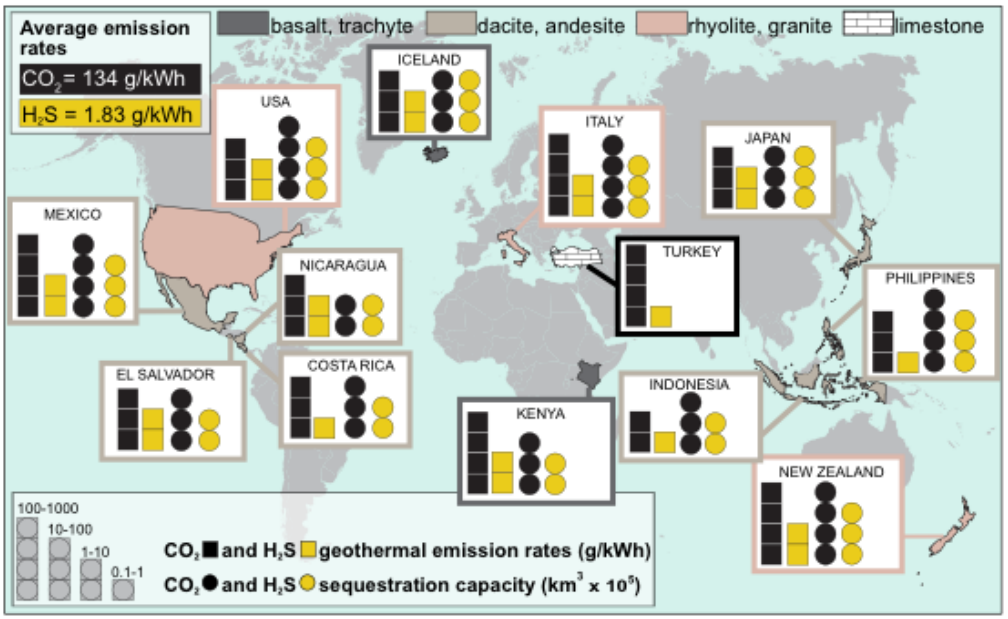

Figure 6. *Worldwide geothermal emission rates of CO_2 and H_2S and sequestration capacities for annual emissions (normalized to geometric surface areas), divided by country, and by generalized rock type associated with geothermal systems – note logarithmic scale.*

Rank (by capacity)[1]	Country	Capacity[1]	Energy[1]	CO_2	H_2S	Geothermal field		Field sequestration capacity	
								SQ $CO_{2\ geo}$	SQ $H_2S_{\ geo}$
		MWe	GWh/yr	t/yr	t/yr	Main lithology	Reference	km^3 (x 10^5)/yr	
1	USA	3450	16600	1510600	15989	sandstone and granite	Adams et al. 2000, Thompson 1992	778	31
2	Philippines	1870	9646	617334	3189	andesite	Williams et al. 2011	228	10
3	Indonesia	1340	9600	47273	1575	andesite	Williams et al. 2011	17	5
4	Mexico	1018	6071	740662	19828	andesite	Williams et al. 2011, Arellano et al. 2005	274	65
	Mexico - Los Azufres			340782	4503	andesite		126	15
5	New Zealand	1005	7000	728000	18512	rhyolite	Krupp and Seward 1987	375	36
	New Zealand - Wairakei			77760	537	rhyolite		40	1
6	Italy	916	5660	1867800	23772	granite	Pertot et al. 2013	962	47
7	Iceland	665	5245	179633	29746	basalt	Alfredsson et al. 2013	37	76
	Iceland - Nesjavellir			18600	11300	basalt		4	29
8	Kenya	636	2868	337290	2608	basalt and trachyte	Omenda and Simiyu 2015	70	7
9	Japan	520	2687	40305	8417	dacite	http://en.openei.org	15	28
10	Turkey	407	3247	3409350	1072	limestone	Haizlip et al. 2013	-	-
11	Costa Rica	207	1511	77281	1337	andesite	Chavarria Rojas 2003, http://en.openei.org	29	4
12	El salvador	204	1442	48119	2699	andesite	Gonzalez Partida et al. 1995, Torio-Henriquez 2007	18	9
	El salvador - Ahuachapan			21620	692	andesite		8	2
13	Nicaragua	159	492	24600	2846	andesite	Porras et al. 2007, http://en.openei.org	9	9
TOTAL		12397	72069	9628247	131590				
TOTAL[1]		12729	73689					2813	328

[1] Bertani 2016

Table 6. *Geothermal emission rates of CO_2 and H_2S by country, together with the field sequestration capacity for 1 year, calculated with A_{geo}. As examples, detailed data of four geothermal power plants across the world are shown (details in Appendix). To calculate these values, the lithologies listed for the country have been associated with the chemically most similar experimental composition: andesite with dacite, and granite with rhyolite. The top 13 countries are listed in decreasing order following their installed geothermal capacity described by Bertani (2016).*

4.4 Economic implications

In the last decades, the CO_2 and H_2S geological sequestration have received increasing attention due to the pressing need to control the environmental aspects and to limit GHG emissions globally. Advantages and disadvantages have been evaluated, and, as all the proposed geoengineering solutions, even this strategy has been found to be lacking in information on two key issues: feasibility and economic impact. Following this, the current experimental findings extended and broadened the strategy applicability into natural geothermal system. From an economical perspective, the low-cost H_2S removal involved with the proposed method of gas re-injection, estimated to be <30 $/t (LDEO Columbia University), could play a key role in the case of geothermal activities characterized by H_2S-rich fluids. New Zealand, Japan, Italy, and Mexico are all examples of countries with H_2S emission rates above the average value of 1.83 g/kWh, generating more than 10 kt of H_2S per year, and spending at least 115 $/t for H_2S reduction (Mamrosh et al., 2012). The *in-situ* simultaneous re-injection of CO_2 and H_2S for geological storage could then act as incentive to drastically decrease the GHG emissions while adopting an economically convenient H_2S abatement system, otherwise very expensive. Also, the coupling of CO_2 and H_2S would optimize the space used by geothermal fields, the number of required facilities, and the capital invested for waste water disposal. Further investigations would however be required to determine CO_2 and H_2S mineralization rates at lower temperatures, permeability and reactive surface area in the reservoirs, and effect of higher gaseous concentrations in the inlet fluids on the reservoir porosity.

4.5 Further implications

From a wider perspective, a number of additional steps are required to assess the sustainability of long-term re-injections, bridging laboratory experiments and field scale projects. Further study on the optimal sequestration in geothermal systems will also have to consider: (1) the clogging of the reservoir due to intensive mineralization close to the fluid re-injection well, (2) the movement of the secondary mineralization front within the reservoir, eventually reaching production wells, and (3) the use of large volumes of valuable groundwater and its implication on the market. However, results suggest that: the porosity close to the re-injection well increases with time due to the vigorous dissolution of the primary rock, and the system does not clog over continuous re-injections modelled for >100 years (Přikryl et al., 2018); the rapid mineralization during field re-injections of CO_2 and H_2S for over 2 years confirms such predictions (Matter et al., 2016); and the use of unlimited supplies of seawater rather than groundwater could be a more feasible and economically convenient option (Gislason and Oelkers, 2014; Snaebjörndottir and Gislason, 2016; Wolff-Boenisch et al., 2011; Wolff-Boenisch and Galeczka, 2018).

More importantly, the current political and economic efforts put into geological storage of gaseous emissions from geothermal activities is not at the level of impacting climate change. However, the implementation of this sequestration strategy to the geothermal energy production provides a greener alternative to energy produced by coal and oil.

5 Conclusions

The present work explored the potential of re-injections of CO_2 and H_2S under geothermal conditions, as a strategy to reduce the anthropogenic emissions into the atmosphere. Flow-through column experiments at 250 °C demonstrate the geochemically possible and rapid sequestration of both gases, even with initial neutral pH, and within rocks of various compositions. The successful mineralization in silicic rocks, such as dacitic and rhyolitic glasses, extends the applicability beyond the Icelandic basalt. However, the faster reactivity of amorphous rocks compared to crystalline material, and the high experimental porosity must be taken into account during the determination of reservoir storage potential. CO_2 and H_2S are mineralized as carbonates and pyrite, respectively, already in the initial stage of fluid-rock interactions. On the other hand, the observation of additional silicate mineralization could be a limiting factor on the long-term, and further detailed investigations are required.

The analysis on CO_2 and H_2S emission rates by country, based on the information available for the main geothermal power plants, estimates fluxes of ~10 Mt of CO_2 per year, and ~0.2 Mt/yr of H_2S, with peaks in Italy, Turkey, U.S., Iceland, Mexico, and New Zealand. The CO_2 rate is consistent with previous studies, whereas the H_2S emission rate is here proposed for the first time. These findings indicate encouraging, yet polluting emissions from power plants that produce energy through renewable sources. The re-injection of gas mixture may help to boost the carbon capture and storage market, exploiting the relatively low cost associated with the capture of CO_2 to also abate the H_2S – the removal of which is otherwise very expensive. The proposed method is five-times cheaper than common H_2S abatement systems. Moreover, this geological sequestration requires relatively small volumes to accommodate the annual CO_2 and H_2S geothermal worldwide emissions, which is very promising for long-term operations.

The worldwide application of this re-injection strategy would lead to the production of enhanced energy from geothermal fluids free from atmosphere-polluting emissions by their permanent mineralization underground, contributing to address one of the major environmental concerns on a global scale.

Supporting Information

Appendix A

Further details about the calculations of CO_2 and H_2S emission rates by country are available in A1 and A2, respectively.

Acknowledgements

We would like to express our thanks to Gylfi Sigurðsson, and Dr. Birgir Jóhannesson for technical assistance. Special thanks to Dr. Kasumi Yasukawa and Dr. Tetsuro Noda (AIST) for sharing her expertise on gaseous emissions from Japanese geothermal power

plants. This research has received funding from the European Union's Horizon 2020 research and innovation program under grant agreement No 764760.

References

Agency for Toxic Substances and Disease Registry (ATSDR), 2016. Toxicological profile for Hydrogen Sulfide / Carbonyl Sulfide, Atlanta, GA: U.S. Department of Health and Human Services, Public Health Service.

Adams, M.C., Moore, J.N., Bjornstad, S., Norman, D.I., 2000. Geologic history of the Coso geothermal system. Transactions-geothermal resources council, 205-210.

Alfredsson, H.A., Oelkers, E.H., Hardarsson, B.S., Franzson, H., Gunnlaugsson, E., Gislason, S.G., 2013. The geology and water chemistry of the Hellisheidi, SW-Iceland carbon storage site. Int. J. Greenhouse Gas Control 12, 399–418.

Anbeek, C., 1992. Surface roughness of minerals and implications for dissolution studies. Geochim. Cosmochim. Acta 56(4), 1461-1469.

Aradóttir, E.S.P., Sonnenthal, E. L., Björnsson, G., Jónsson, H., 2012. Multidimensional reactive transport modeling of CO_2 mineral sequestration in basalts at the Hellisheidi geothermal field, Iceland. Int. J. Greenhouse Gas Control 9, 24–40.

Aradóttir, E.S.P., Gunnarsson, I., Sigfússon, B., Gíslason, S.R., Oelkers, E.H., Stute, M., Matter, J.M., Snaebjörnsdottir, S.Ó., Mesfin, K.G., Alfredsson, H.A., Hall, J., Arnarsson, M.T., Dideriksen, K., Júliusson, B.M., Broecker, W.S., Gunnlaugsson, E., 2015. Towards cleaner geothermal energy: Subsurface sequestration of sour gas emissions from geothermal power plants World Geothermal Congress 2015, Melbourne, Australia.

Arellano, V.M., Torres, M.A., Barragán, R.M., 2005. Thermodynamic evolution of the Los Azufres, Mexico, geothermal reservoir from 1982 to 2002. Geothermics, 34(5), 592-616.

Arnórsson, S., Bjarnason, J.Ö., Giroud, N., Gunnarsson, I., Stefánsson, A., 2006. Sampling and analysis of geothermal fluids. Geofluids 6, 203-216.

Bachu, S., and Gunter, W.D., 2005. Overview of acid-gas injection operations in Western Canada, Greenhouse Gas Control Technologies 7. Elsevier Science Ltd, Oxford, pp. 443-448.

Barbier, E., 2002. Geothermal energy technology and current status: an overview. Renew. Sust. Energy Rev. 6, 3-65.

Benson, S.M., and Cole, D.R., 2008. CO_2 sequestration in deep sedimentary formations. Elements 4(5), 325-331.

Bertani, R., 2016. Geothermal power generation in the world 2010–2014 update report. Geothermics 60, 31-43.

Brantley, S.L., and Chen, Y., 1995. Chemical weathering rates of pyroxenes and amphiboles. In Chemical weathering rates of silicate minerals, edited by A.F. White and S.L. Brantley, Rev. Mineral. 31,119–172.

Brantley, S.L., and Mellott, N.P., 2000. Surface area and porosity of primary silicate minerals. Am. Mineral. 85(11-12), 1767-1783.

Chavarría Rojas, L., 2003. Miravalles geothermal field, Costa Rica: evidence of thermal evolution and a comparison of the mineralogy of an acid well and a neutral well. Rep. 6, 115-142 pp, The United Nations University, Reykjavik, Iceland.

Fridriksson, T., Mateos, A., Audinet, P., Orucu, Y., 2016. Greenhouse gases from geothermal power production. World Bank, Washington, DC. © World Bank. https://openknowledge.worldbank.org/handle/10986/24691 License: CC BY 3.0 IGO.

Galeczka, I., Wolff-Boenisch, D., Oelkers, E.H., Gislason, S.R., 2014. An experimental study of basaltic glass–H_2O–CO_2 interaction at 22 and 50°C: Implications for subsurface storage of CO_2. Geochim. Cosmochim. Acta 126, 123-145.

Gislason, S.R., and Oelkers, E.H., 2003. Mechanism, rates, and consequences of basaltic glass dissolution: II. An experimental study of the dissolution rates of basaltic glass as a function of pH and temperature. Geochim. Cosmochim. Acta 67, 3817–3832.

Gislason, S.R., and Oelkers, E.H., 2014. Carbon storage in basalt. Science 344(6182), 373-374.

Gonzalez Partida, E., Torres Rodriguez, V., Birkle, P., Arellano Gomez, V., Campos Romero, A., 1995. Geology of the Ahuachapan-Chipilapa, El Salvador C.A. geothermal zone. Proceedings of World Geothermal Congress 1995, 683-686.

Gunnarsson, G., Arnaldsson, A., Oddsdóttir, A.L., 2011. Model simulations of the Hengill area: Southwestern Iceland. Transp. Porous Media 90, 3–22. doi 10.1007/s11242-010-9629-1.

Gunnarsson, I., Júlíusson, B.M., Aradóttir, E., Arnarson, M.T., 2015. Pilot Scale Geothermal Gas Separation, Hellisheiði Power Plant, Iceland, World Geothermal Congress 2015, Melbourne, Australia.

Gunter, W.D., Wiwehar, B., and Perkins E.H., 1997. Aquifer disposal of CO_2-rich greenhouse gases: Extension of the time scale of experiment for CO_2-sequestering reactions by geochemical modelling. Miner. Petrol. 59(1-2), 121-140.

Gysi, A.P., Stefánsson, A., 2012. CO_2-water–basalt interaction. Low temperature experiments and implications for CO_2 sequestration into basalts. Geochim. Cosmochim. Acta 81, 129-152.

Haizlip, J.R., Haklidir, F.T., and Garg, S.K., 2013. Comparison of reservoir conditions in high noncondensible gas geothermal systems. In Proceedings, Thirty-Eighth Workshop on Geoth. Reservoir Eng., Stanford University.

Hansell, A., and Oppenheimer, C., 2010. Health Hazards from Volcanic Gases: A Systematic Literature Review. Arch. Environ.Health 59(12), 628-639.

Hellevang, H., Haile, B.G., and Tetteh, A., 2017. Experimental study to better understand factors affecting the CO_2 mineral trapping potential of basalt. Greenhouse Gas Sci. Technol. 7, 143-157, doi:10.1002/ghg.1619.

Hofmann, D.J., Butler, J.H., Tans, P.P., 2009. A new look at atmospheric carbon dioxide. Atmos. Environ. 43, 2084-2086.

IPCC, 2014. Climate Change 2014: Mitigation of Climate Change. Contribution of Working Group III to the Fifth Assessment Report of the Intergovernmental Panel on Climate Change, in: Edenhofer, O., Pichs-Madruga, R., Sokona, Y., Farahani, E., Kadner, S., Seyboth, K., Adler, A., Baum, I., Brunner, S., Eickemeier, P., Kriemann, B., Savolainen, J., Schlömer, S., Stechow, C.v., Zwickel, T., Minx, J.C. (Eds.). Cambridge University Press, Cambridge, United Kingdom and New York, NY, USA, p. 1132.

Kristmannsdóttir, H., Ármannsson, H., 2003. Environmental aspects of geothermal energy utilization. Geothermics 32, 451-461.

Krupp, R.E., and Seward, T.M., 1987. The Rotokawa geothermal system, New Zealand; an active epithermal gold-depositing environment. Econ. Geol. 82(5), 1109-1129.

LDEO Columbia University - Earth Institute. http://www.ldeo.columbia.edu/news-events/first-iceland-power-plant-turns-carbon-emissions-stone (June 9, 2016).

Lüttge, A., and Arvidson, R.S., 2008. The mineral-water interface. In Kinetics of Water-Rock Interaction, edited by S.L. Brantley, J.D. Kubicki and A.F. White, 73-107, Springer New York.

Mamrosh, D., McIntush, K., Beitler, C., Markússon, S., Einarsson, K., 2012. Screening of H_2S abatement options for geothermal power noncondensable gas at Bjarnarflag. GRC Trans 36, 1217-1226.

Matter, J.M., Stute, M., Snæbjörnsdottir, S.Ó., Oelkers, E.H., Gislason, S.R., Aradottir, E.S., Sigfusson, B., Gunnarsson, I., Sigurdardottir, H., Gunnlaugsson, E., Axelsson, G., Alfredsson, H.A., Wolff-Boenisch, D., Mesfin, K., Taya, D.F.d.l.R., Hall, J., Dideriksen, K., Broecker, W.S., 2016. Rapid carbon mineralization for permanent disposal of anthropogenic carbon dioxide emissions. Science 352, 1312-1314.

Matter, J.M., Takahashi, T., Goldberg, D.S., 2007. Experimental evaluation of in situ CO_2-water-rock reactions during CO_2 injection in basaltic rocks: implications for geological CO_2 sequestration. Geochem. Geophys. Geosyst. 8, Q02001, doi:10.1029/2006GC001427.

McGrail, B.P., Schaef, H.T., Spane, F.A., Cliff, J.B., Qafoku, O., Horner, J.A., Thompson, C.J., Owen, A.T., Sullivan, C.E., 2016. Field validation of supercritical CO_2 reactivity with basalts. Environ. Sci. Tech. Let. 4(1), 6-10.

Oelkers, E.H., Gislason, S.R., 2001. The mechanism, rates and consequences of basaltic glass dissolution: I. An experimental study of the dissolution rates of basaltic glass as a

function of aqueous Al, Si and oxalic acid concentration at 25°C and pH = 3 and 11. Geochim. Cosmochim. Acta 65, 3671-3681.

Omenda, P., and Simiyu, S., 2015. Country update report for Kenya 2010–2014. Proceedings of World Geothermal Congress 2015, Melbourne, Australia.

OpenEI, Energy Information and Data. National Renewable Energy Laboratory. U.S. Department of Energy. http://en.openei.org

Pertot, C., Sabatelli, F., Messia, M., Marco, D., 2013. Assessment of geothermal power plants impact on air quality – effect of H2S abatement with AMIS ® in the Larderello-Travale-Radicondoli geothermal area (Tuscany). Proceedings European Geothermal Congress 2007.

Porras, E.A., Tanaka, T., Fujii, H., Itoi, R., 2007. Numerical modeling of the Momotombo geothermal system. Nicaragua, Geothermics, 36(4), 304-329.

Přikryl, J., Jha D., Stefánsson, A., Stipp, S., 2017. Mineral dissolution in porous media: An experimental and modeling study on kinetics, porosity and surface area evolution. Appl. Geochem. 87, 57-70.

Přikryl, J., Marieni, C., Gudbrandsson, S., Aradóttir, E.S., Gunnarsson, I., Stefánsson, A., 2018. H_2S sequestration process and sustainability in geothermal systems. Geothermics 71, 156-166.

Rappold, T.A., Lackner, K.S., 2010. Large scale disposal of waste sulfur: From sulfide fuels to sulfate sequestration. Energy 35, 1368-1380.

Rodríguez, E., Harvey, W.S., Ásbjörnsson, E.J., 2014. Review of H_2S abatement methods in geothermal plants, Proceedings 38th Workshop on Geothermal Reservoir Engineering.

Rosenbauer, R.J., Thomas, B., Bischoff, J.L., Palandri, J., 2012. Carbon sequestration via reaction with basaltic rocks: geochemical modeling and experimental results. Geochim. Cosmochim. Acta 89, 116-133.

Sanopoulos, D., Karabelas, A., 1997. H_2S abatement in geothermal plants: Evaluation of process alternatives. Energy Sources 19, 63-77.

Schaef, H.T., McGrail, B.P., Owen, A.T., 2009. Basalt- CO_2–H_2O interactions and variability in carbonate mineralization rates. Energy Procedia 1, 4899-4906.

Shibuya, T., Yoshizaki, M., Masaki, Y., Suzuki, K., Takai, K., Russell, M.J., 2013. Reactions between basalt and CO_2-rich seawater at 250 and 350°C, 500 bars: Implications for the CO_2 sequestration into the modern oceanic crust and the composition of hydrothermal vent fluid in the CO_2-rich early ocean. Chem. Geol. 359, 1-9.

Snæbjörnsdóttir, S.Ó., and Gislason, S.R., 2016. CO_2 Storage potential of basaltic rocks offshore Iceland. Energy Procedia 86, 371-380, doi:10.1016/j.egypro.2016.01.038.

Stefánsson, A., Arnórsson, S., Gunnarsson, I., Kaasalainen, H., Gunnlaugsson, E., 2011. The geochemistry and sequestration of H_2S into the geothermal system at Hellisheidi, Iceland. J. Volcanol. Geoth. Res. 202, 179-188.

Stefánsson, A., Gunnarsson, I., Giroud, N., 2007. New methods for the direct determination of dissolved inorganic, organic and total carbon in natural waters by Reagent-Free™ Ion Chromatography and inductively coupled plasma atomic emission spectrometry. Anal. Chim. Acta 582(1), 69-74.

Thompson, R.C., 1992. Structural stratigraphy and intrusive rocks at The Geysers geothermal field. Monograph on The Geysers Geothermal Field, 17, 59-63.

Torio-Henríquez, E., 2007. Petrography and mineral alteration in Berlin geothermal field. In Proceedings of the 32nd Workshop on Geothermal Reservoir Engineering, Stanford University, Stanford, California, January 22–24, SGP-TR-183.

Watanabe, K., and Takahashi, H., 1995. Fractal geometry characterization of geothermal reservoir fracture networks. J. Geoph. Res. Solid Earth 100(B1), 521-528.

Williams, C.F., Reed, M.J, Anderson, A.F., 2011. Updating the classification of geothermal resources. Proceedings of Thirty-Sixth Workshop on Geothermal Reservoir Engineering, Standford University, Stanford, California.

Wolff-Boenisch, D., Galeczka, I.M., 2018. Flow-through reactor experiments on basalt-(sea) water-CO_2 reactions at 90 °C and neutral pH. What happens to the basalt pore space under post-injection conditions? International Journal of Greenhouse Gas Control 68, 176-190.

Wolff-Boenisch, D., Gislason, S.R., Oelkers, E.H., Putnis, C.V., 2004. The dissolution rates of natural glasses as a function of their composition at pH 4 and 10.6, and temperatures from 25 to 74°C. Geochim. Cosmochim. Acta 68, 4843-4858.

Wolff-Boenisch, D., Wena, S., Gislason, S.R., Oelkers E.H., 2011. Dissolution of basalts and peridotite in seawater,in the presence of ligands, and CO_2: Implications for mineral sequestration of carbon dioxide. Geochimi. Cosmochim. Acta 75, 5510–5525.

Supporting Information (Appendix A)

Table A1. CO_2 emissions by country, before any abatement system.

Country / Power plants	CO_2 emission energy rate		Average energy		CO_2 emissions	
	g/kWh	Reference	GWh/yr	`Reference	t/yr	Reference
Costa Rica	51	CALCULATED	1511	Bertani 2016	77281	SUM LOCALS
Costa Rica Miravalles	63.6	Moya and Rodriguez 2009	1204	Moya and Rodriguez 2009	76574	CALCULATED
Costa Rica Las Pailas	2.3	Moya and Rodriguez 2009	307	Moya and Rodriguez 2009	706	CALCULATED
El salvador	33	CALCULATED	1442	Bertani 2016	48119	SUM LOCALS, Wall and Matek 2016
El salvador Ahuachapan					21620	Padilla 2007
El salvador Berlin					26499	Padilla 2007
Iceland	34	CALCULATED	5245	Bertani 2016	179633	Juliusson et al. 2015
Indonesia	5	CALCULATED	9600	Bertani 2016	47273	Yuniarto et al. 2015
Italy	330	Fridriksson et al. 2016	5660	Bertani 2016	1867800	CALCULATED
Japan	15	Nakao et al. 2015, FEPC Japan 2012	2687	Bertani 2016	40305	CALCULATED
Kenya	118	CALCULATED	2868	Bertani 2016	337290	SUM LOCALS
Kenya Olkaria I + wellheads	20	Wetang'ula 2011 (0.3% NCG, 95 %CO2), DiPippo 2012	992	Omenda and Simiyu 2015	19840	CALCULATED
Kenya Olkaria II	20	Wetang'ula 2011 (0.3% NCG, 95 %CO2), DiPippo 2012	764	Omenda and Simiyu 2015	15280	CALCULATED
Kenya Olkaria III	270	Bertani and Thain 2002	867	Omenda and Simiyu 2015	234090	CALCULATED
Kenya Olkaria IV	230	Bertani and Thain 2002	296	Omenda and Simiyu 2015	68080	CALCULATED
Kenya Eburru and Oserian			22	Omenda and Simiyu 2015	BINARY	
Mexico	122	Bertani and Thain 2002, Wall and Matek 2016	6071	Bertani 2016	740662	CALCULATED
New Zealand	104	Fridriksson et al. 2016	7000	Bertani 2016	728000	CALCULATED
Nicaragua	50	CALCULATED	492	Bertani 2016	24600	SUM LOCALS
Nicaragua Momotombo	50	Wall and Matek 2016	271	Mayorga 2005	13550	CALCULATED
Nicaragua San Jacinto-Tizate	50	Wall and Matek 2016	221	difference (Bertani - Mayorga)	11050	CALCULATED
Philippines	64	Wall and Matek 2016	9646	Bertani 2016	617344	CALCULATED
Turkey	1050	Fridriksson et al. 2016, Aksoy 2014	3247	Bertani 2016	3409350	CALCULATED
USA	91	Fridriksson et al. 2016	16600	Bertani 2016	1510600	CALCULATED

Table A2. *H_2S emissions by country, before any abatement system. Dry steam and flash plant percentage from Bertani 2016.*

Country/Power plants	H_2S emission energy rate		Average energy		Dry steam and flash plants[1]	H_2S emissions	
	g/kWh	Reference	GWh/yr	Reference	%	t/yr	Reference
Costa rica	0.88	CALCULATED	1511	Bertani (2016)	68	1337	SUM LOCALS
Costa rica Miravalles	1.06	Moya and Rodriguez (2009)	1203	Moya and Rodriguez (2009)		1275	CALCULATED
Costa rica Las Pailas	0.2	Moya and Rodriguez (2009)	307	Moya and Rodriguez (2009)		61	CALCULATED
El Salvador	1.95	AVERAGE LOCAL DATA	1442	Bertani (2016)	96	2699	CALCULATED
El Salvador Berlin	3.1	Padilla (2007)	879	CALCULATED		2725	Padilla (2007)
El Salvador Ahuachapan	0.8	Padilla (2007)	865	CALCULATED		692	Padilla (2007)
Iceland	5.67	CALCULATED	5245	Bertani (2016), Ragnarsson (2015)	98	29746	Juliusson et al. (2015)
Indonesia	0.16	CALCULATED	9600	Bertani (2016)	99	1575	Yuniarto et al. (2015)
Italy	4.20	AVERAGE LOCAL DATA	5660	Bertani (2016)	100	23772	CALCULATED
Italy Larderello-Travale-Radicondoli	4.20	Pertot et al. (2013)	4675	Pertot et al. (2013)		19635	CALCULATED
Japan	3.13	CALCULATED	2687	Bertani (2016)	99	8417	Yasuka (2017) pers. comm.
Japan Akita	0.07	CALCULATED	535	Yasukawa and Sasada (2015)		36	Yasuka (2017) pers. comm.
Japan Matsukawa	8.18	CALCULATED	95	Yasukawa and Sasada (2015)		777	Yasuka (2017) pers. comm.
Japan Yanaizu-Nishiyama	15.3	CALCULATED	399	Kawazoe and Combs (2004)		6100	Yasuka (2017) pers. comm.
Kenya	1.07	AVERAGE LOCAL DATA	2868	Bertani (2016)	85	2608	CALCULATED
Kenya Olkaria	1.07	Wetang'ula (2011)	2868	Bertani (2016)		3069	CALCULATED
Mexico	3.55	AVERAGE LOCAL DATA	6071	Bertani (2016)	92	19828	CALCULATED
Mexico Los Azufres	2.92	Maya and Gutiérrez-Negrín (2007)	1542	Gutiérrez-Negrín et al. (2015)		4503	CALCULATED
Mexico Cerro Prieto	4.2	Hunt (2001)	4127	Gutiérrez-Negrín et al. (2015)		17333	CALCULATED
New Zealand	3.8	AVERAGE LOCAL DATA	7000	Bertani (2016)	69	18512	CALCULATED
New Zealand Ohaaki	6.4	Barbier (1991)	300	Carey et al. (2015)		1920	CALCULATED
New Zealand Rotokawa	4.6	CALCULATED	1270	Carey et al. (2015)		5840	Winick et al. (2016)
New Zealand Wairakei plant	0.5	Barbier (1991)	1074	CALCULATED		537	Bierre and Fullerton (2015), before abatement
Nicaragua	6.50	AVERAGE LOCAL DATA	492	Bertani (2016)	89	2846	CALCULATED
Nicaragua San Jacinto-Tizate	6.50	CALCULATED	221	difference (Bertani - Mayorga)		1436	Aráuz Torres (2014)
Philippines	0.38	AVERAGE LOCAL DATA	9646	Bertani (2016)	87	3189	CALCULATED
Philippines Tongonan	0.38	CALCULATED	4030	Fronda et al. (2015)		1523	Villena et al. 2005
Turkey	0.67	AVERAGE LOCAL DATA	3247	Bertani (2016)	49	1072	CALCULATED
Turkey Denizli-Kizildere	0.29	CALCULATED	710	Mertoglu et al. (2015)		203	Gokcen et al. (2004)
Turkey Aydin-Germencik	1.06	CALCULATED	587	Mertoglu et al. (2015)		623	Haizlip et al. (2013)
USA	1.28	AVERAGE LOCAL DATA	16600	Bertani (2016)	75	15989	CALCULATED
USA Coso	1.03	CALCULATED for 2002	2333	http://www.energy.ca.gov/almanac/renewables_data/geothermal/		2392	Monastero (2002), before abatement
USA Geysers	1.54	CALCULATED	6512	Farison et al. (2010)		10050	Farison et al. (2010), before abatement

References

Aksoy, N. (2014), Power generation from geothermal resources in Turkey, Renewable Energy, 68, 595-601.

Aráuz Torres, M. A. (2014), Modeling H2S dispersion from San Jacinto-Tizate geothermal power plant, Nicaragua, University of Iceland, Reykjavik.

Barbier, E. (1991), Geothermal energy: Its role in the generation of electricity and its environmental impact Rep.

Bertani, R. (2016), Geothermal power generation in the world 2010–2014 update report, Geothermics, 60, 31-43.

Bertani, R., and I. Thain (2002), Geothermal power generating plant CO2 emission survey, IGA News, 49, 1-3.

Bierre, E., and R. Fullerton (2015), Hydrogen sulphide removal from geothermal power station cooling water using a biofilm reactor, Proceedings of World Geothermal Congress 2015, Melbourne, Australia.

Carey, B., M. Dunstall, S. McClintock, B. White, G. Bignall, K. Luketina, B. Robson, S. Zarrouk, and A. Seward (2015), 2015 New Zealand Country Update, Proceedings of World Geothermal Congress 2015, Melbourne, Australia.

Cubillas, P., S. Köhler, M. Prieto, C. Chaïrat, and E. H. Oelkers (2005), Experimental determination of the dissolution rates of calcite, aragonite, and bivalves, Chem. Geol., 216(1–2), 59-77.

DiPippo, R. (2012), Geothermal power plants: principles, applications, case studies and environmental impact, Butterworth-Heinemann.

Farison, J., B. Benn, and B. Berndt (2010), Geysers power plant H2S abatement update, Geoth. Res. Council Trans., 34, 1229-1234.

FEPC - The Federation of Electric Power Companies of Japan (2012), Environmental action plan by the Japanese electric utility industry Rep.

Fridriksson, T., A. Mateos, P. Audinet, and Y. Orucu (2016), Greenhouse gases from geothermal power production, World Bank, Washington, DC. © World Bank. https://openknowledge.worldbank.org/handle/10986/24691 License: CC BY 3.0 IGO.

Fronda, A. D., M. C. Marasigan, and V. S. Lazaro (2015), Geothermal development in the Philippines: The country update, Proceedings of World Geothermal Congress 2015, Melbourne, Australia, 19-25 April 2015.

Gautier, J.-M., E. H. Oelkers, and J. Schott (2001), Are quartz dissolution rates proportional to B.E.T. surface areas?, Geochim. Cosmochim. Acta, 65(7), 1059-1070.

Gokcen, G., H. K. Ozturk, and A. Hepbasli (2004), Overview of Kizildere geothermal power plant in Turkey, Energy conversion and management, 45(1), 83-98.

Gutiérrez-Negrín, L. C., R. Maya-González, and J. L. Quijano-León (2015), Present situation and perspectives of geothermal in Mexico, Proceedings of World Geothermal Congress 2015, Melbourne, Australia.

Guy, C., and J. Schott (1989), Multisite surface reaction versus transport control during the hydrolysis of a complex oxide, Chem. Geol., 78(3), 181-204.

Haizlip, J. R., F. T. Haklidir, and S. K. Garg (2013), Comparison of reservoir conditions in high noncondensible gas geothermal systems, Proceedings of Thirty-Eighth Workshop on Geothermal Reservoir Engineering, Stanford University.

Hunt, T. M. (2001), Five lectures on environmental effects of geothermal utilization, United Nations University.

Júlíusson, B. M., I. Gunnarsson, K. V. Matthiasdottir, S. H. Markusson, B. Bjarnason, O. G. Sveinsson, T. Gislason, and H. H. Thorsteinsson (2015), Tackling the challenge of H2S emissions, Proceedings of World Geothermal Congress 2015, Melbourne, Australia.

Kawazoe, S., and J. Combs (2004), Geothermal Japan, Geothermal Resources Council Bulletin, 33(2), 58-62.

Maya, G. R., and L. Gutiérrez-Negrín (2007), Recursos geotérmicos para generar electricidad en México, Revista Digital Universitaria, 8(12), 12.

Mayorga, A. Z. (2005), Nicaragua country update, Proceedings of World Geothermal Congress 2005, Antalya, Turkey.

Mertoglu, O., S. Simsek, and N. Basarir (2015), Geothermal Country Update Report of Turkey (2010-2015), Proceedings of World Geothermal Congress 2015, Melbourne, Australia.

Monastero, F. C. (2002), An overview of Industry-Military Cooperation in the development of power operations at the Coso Geothermal Field in Southern California, Geoth. Res. Counc. Bull, 31, 188-195.

Moya, P., and E. M. Rodríguez (2009), The contribution of geothermal exploitation at the Miravalles geothermal field toward the reduction of global warming, Proceedings of Short course on surface exploration for geothermal resources, Auachapan and Santa Tecla, El Salvador, 17-30 October 2009.

Nakao, Y., H. Kaieda, Y. Mugikura, T. Iwatsubo, M. Iuchi, and Y. Watanabe (2015), Development of hybrid geothermal power plants combined with other thermal energy sources, Development, 19, 25.

OpenEI, Energy Information and Data. National Renewable Energy Laboratory. U.S. Department of Energy. http://en.openei.org

Padilla, E. K. (2007), Preliminary study on emission abatement and use of gas from geothermal power plants in El Salvador, Report, 18, 417-446.

Ragnarsson, Á. (2015), Geothermal development in Iceland 2010-2014, Proceedings of World Geothermal Congress 2015, Melbourne, Australia.

Takahashi, K., and M. Kuragaki (2000), Yanaizu-Nishiyama geothermal power station H2S abatement system, Proceedings of World Geothermal Congress 2000, Kyushu - Tohoku, Japan.

Villena, J. P., E. H. Alcober, R. G. Jabonillo, D. H. Cruz, J. R. S. Peñaranda, D. R. Sanchez, and H. V. Guillen (2005), Evaluation of the results of the Tongonan-1 CO2 Gas Injection Project, Leyte, Philippines, Proceedings of World Geothermal Congress 2005, Antalya, Turkey.

Wall, A., and B. Matek (2016), Geothermal green bond certification: Challenges in investment screen criteria development using global geothermal carbon dioxide emissions rates, Proceedings of 41st Workshop on Geothermal Reservoir, Stanford University, Stanford, California.

Wetang'ula, G. N. (2011), Olkaria geothermal power plants, Kenya: preliminary evaluation of mercury emission to the atmosphere, J. Environ. Sci. Engin., 5(11).

Winick, J. A., S. Addison, S. Sewell, E. Buscarlet, D. Hernandez, and F. Siega The geochemical response of the Rotokawa reservoir to the first five years of Nga Awa Purua production, Proceedings of 41st Workshop on Geothermal Reservoir Engineering 2016, Stanford University, Stanford, California.

Wolff-Boenisch, D., S. R. Gislason, E. H. Oelkers, and C. V. Putnis (2004), The dissolution rates of natural glasses as a function of their composition at pH 4 and 10.6, and temperatures from 25 to 74°C, Geochim. Cosmochim. Acta, 68(23), 4843-4858.

Yuniarto, T. E. B. Soesilo, and E. Heviati (2015), Geothermal Power Plant Emissions in Indonesia, Proceedings of World Geothermal Congress 2015, Melbourne, Australia.

Appendix IV

Appendix IV

Tracing olivine carbonation and serpentinization in CO_2-rich fluids via magnesium exchange and isotopic fractionation

Jan Přikryl[1], Andri Stefánsson[1], Christopher R. Pearce[2]

[1]Institute of Earth Sciences, University of Iceland, Sturlugata 7, 101 Reykjavik, Iceland

[2]National Oceanography Centre Southampton, University of Southampton Waterfront Campus, European Way, Southampton, SO14 3ZH, UK

Geochimica et Cosmochimica Acta

(submitted)

Highlights:

- The rate of olivine carbonation/serpentinization is predominately controlled by pH
- Magnesium isotopic fractionation can be used to track reaction progress
- Fluid δ^{26}Mg compositions are primarily influenced by secondary mineral formation

Keywords: kinetic model; Mg isotope fractionation; hydrothermal; carbonation; CO_2; serpentinization; tracing reaction progress

Abstract

Chemical exchange between seawater and the oceanic crust is thought to play a significant role in the regulation of the global magnesium (Mg) cycle, yet relatively little is known about the rates and mechanisms of Mg exchange in mafic crustal environments. In this study we experimentally characterize the extent, and nature, of Mg isotope fractionation during the carbonation and serpentinization of olivine (one of the principal minerals found in ultramafic rocks) under hydrothermal conditions. Olivine alteration was found to be incongruent, with fluid composition and the secondary mineralogy varying according to the extent of reaction. In mildly acid water (pH ~6.5), olivine dissolved to form Mg-Fe carbonate solid solutions and minor chrysotile. Upon carbonation and a decrease of CO_2 in the water, the pH increased to >8, with chrysotile and brucite becoming the dominant alteration minerals. The Mg-rich carbonates and chrysotile preferentially incorporated lighter Mg isotopes, whereas brucite preferentially incorporated heavier Mg isotopes. This resulted in a ~0.5‰ increase of the δ^{26}Mg composition of the fluid relative to olivine during the initial carbonation and serpentinization reactions, followed by a decrease in δ^{26}Mg upon the formation of brucite. Our experimental and modeling results therefore demonstrate that the δ^{26}Mg composition of fluids involved in olivine alteration reflect the type and quantity of secondary Mg minerals formed, which in turn depend on the pH and CO_2 concentration of the water. Comparison of these results with natural ground- and thermal waters from basaltic terrains indicate that the δ^{26}Mg composition of natural waters are likely to also be controlled by mafic rock leaching and incorporation of isotopically light Mg into carbonates and Mg-Si minerals such as chrysotile. Together, these findings improve our understanding of Mg isotope systematics during water-rock interaction, and suggest that δ^{26}Mg may be a useful tool for tracing reactions that are critical to geological CO_2 sequestration.

1 Introduction

The oceanic crust of the Earth (together with hydrosphere and continental crust) contain <0.1% of the total Mg in the bulk Earth, however, show the largest Mg isotopic variation (e.g. Galy et al., 2003; Foster et al., 2010; Huang, 2013; Teng, 2017). This highlights their significance for understanding Mg isotopic balance of the bulk Earth and global Mg cycling. The oceanic crust mainly consists of ultramafic and mafic rocks, with olivine among the major primary minerals (e.g. McDonough and Sun, 1995). Alteration of olivine near and at the Earth's surface is fast compared to many other igneous minerals (e.g., Palandri and Kharaka, 2004). The process involves the dissolution of olivine followed by precipitation of secondary minerals like carbonates, chrysotile, talc, brucite and serpentine (e.g., Janecky and Seyfried, 1986; Berndt et al., 1996). The serpentinization of mafic rocks results in the generation of H_2 by water reduction through oxidation of ferrous iron (Fe^{II}) dissolved from the primary rocks like olivine. The H_2 formed may further lead to formation of inorganic hydrocarbons from reduction of inorganic carbon like CO_2 (e.g., McCollom and Seewald, 2001; Etiope and Sherwood Lollar, 2013). Moreover, the sequestration process into mafic and ultramafic rocks has received growing interest as a potential method for CO_2 storage and reducing atmospheric CO_2 concentration, as such rock types are a primary source of Mg, Fe and Ca needed for carbonate formation (e.g., McGrail et al., 2006; Gíslason et al., 2010; Matter et al., 2016).

Previous studies on the carbonation and serpentinization of mafic and ultramafic rocks have focused on characterizing water-rock interaction with seawater and meteoric water at various pressures and temperatures (e.g., James et al., 2003; Giammar et al., 2005; Béarat et al., 2006; Seyfried et al., 2007; Andreani et al., 2009; McCollom and Bach, 2009; King et al., 2010; Jones et al., 2010; Stefánsson, 2010; Daval et al., 2011; Hövelmann et al., 2011; Gysi and Stefánsson, 2011, 2012a; Klein and Garrido, 2011; Marcaillou et al., 2011; Marieni et al. 2013; Lafay et al., 2012; Neubeck et al., 2014). Such alteration has been observed to result in the formation of various carbonate minerals at elevated CO_2 concentrations and pH <7, whereas at low CO_2 concentrations the water pH become more alkaline, resulting in the formation of clays, serpentine and chrysotile. Many of the alteration minerals contain the same major elements (e.g. Mg and Si), meaning that quantifying the rate of carbonization and serpentinization reactions and the processes influencing such reactions may be difficult. Such an understanding is important to quantify carbonization associated with CO_2 mineral sequestration and quantifying variations in the Mg isotope (δ^{26}Mg) composition of the fluids may be useful in this regard.

Ultramafic and mafic oceanic rocks and mantle xenoliths show a relatively small δ^{26}Mg range of -0.35 to -0.18‰ (e.g., Wiechert and Halliday, 2007; Teng et al., 2007, 2010, 2015; Liu et al., 2017). In contrast, continental basalts display more negative δ^{26}Mg values of -0.60 to -0.35‰ as a result of incongruent partial melting of an isotopically light carbonated mantle (e.g., Huang et al., 2015), while altered oceanic basalts show significant δ^{26}Mg variations ranging from -2.76 to +0.21‰, suggesting significant Mg isotope fractionation upon water-rock interaction (Huang, 2013). The lowest δ^{26}Mg ratios in these altered basalts are typically associated with carbonation reactions, while the higher values are generally associated with serpenitinization reactions. The fluids associated with these alteration reactions also have varying δ^{26}Mg compositions, with seawater having a uniform composition of -0.83±0.09‰ (e.g. Ling et al. 2011), while thermal and non-thermal groundwaters range between -0.96 and +0.64‰ (Pogge von Strandmann et al. 2008). Carbonate minerals formed in the altered rocks are typically enriched in ^{24}Mg relative to original silicate phases (Beinlich et al., 2014; Wimpenny et al. 2014). The variations observed in fluid δ^{26}Mg may result from Mg isotope fractionation upon water-rock interaction with different fractionation factors for different secondary minerals (Wimpenny et al., 2014; Voigt et al., 2016; Liu et al., 2017). Once they have been properly quantified, such differences may be used to trace the degree of water-rock interaction, including the carbonation and serpenitization of mafic and ultramafic rocks.

In this study, we conducted reaction path experiments and geochemical and isotope modeling of olivine alteration in CO_2-rich hydrothermal fluids as a function of reaction time and CO_2 concentration. The reaction process was traced through time by solution chemistry, alteration mineralogy and Mg isotope systematics in order to define the major factors controlling water-olivine (mafic rock) alteration. Particular focus was made on understanding the extent of δ^{26}Mg fractionation during mineralization, and its potential for use as a mechanism of tracing CO_2 sequestration in mafic and ultramafic rocks.

2 Experimental methods

2.1 Material and Experimental design

The olivine used in the experiments was collected from Almklovdalen peridotite massif, Western Gneiss Region, Norway (Brueckner et al., 2010). The source dunite samples contained over 90% olivine, which was handpicked, crushed in a jaw crusher and agate mortar and pestle then dry sieved. The 45-125 μm size fraction was used in all of the experiments. The grains were unzoned, and have a composition determined by EMPA (n = 23) of $Mg_{1.81\text{-}1.88}Fe_{0.13\text{-}0.15}Si_{0.97\text{-}1.01}O_4$. The sum of other elements was ≤0.36 wt%. Hereafter, the olivine composition is referred to as 93% forsterite (Fo_{93}). Prior to the experiments it was cleaned using deionized water, acetone and magnet, followed by drying at 40°C. The specific geometric surface area (A_{geo}) was determined according to the method of Tester et al. (1994) to be 226.3 cm^2/g.

The batch (closed-system) experiments of olivine alteration in CO_2-rich aqueous solutions were carried out at 5-21 mmol/kg initial total dissolved inorganic carbon (ΣCO_2) in a Parr stirring reactor made of titanium (Fig. 1). Prior to each experiment the 600 ml reactor was filled with ~53 g Fo_{93} and ~400 g of degassed CO_2-rich fluid under N_2 atmosphere, giving an initial fluid/rock ratio of ~8. The reactor was heated to 150°C with the pressure controlled by the solution vapor saturation pressure. The solutions were prepared from deionized water, NaCl (ACS, Sigma-Aldrich), $NaHCO_3$ (ACS, Sigma-Aldrich) and 37% HCl (pro. anal. Merck). The starting conditions of the experiments are summarized in Table 1.

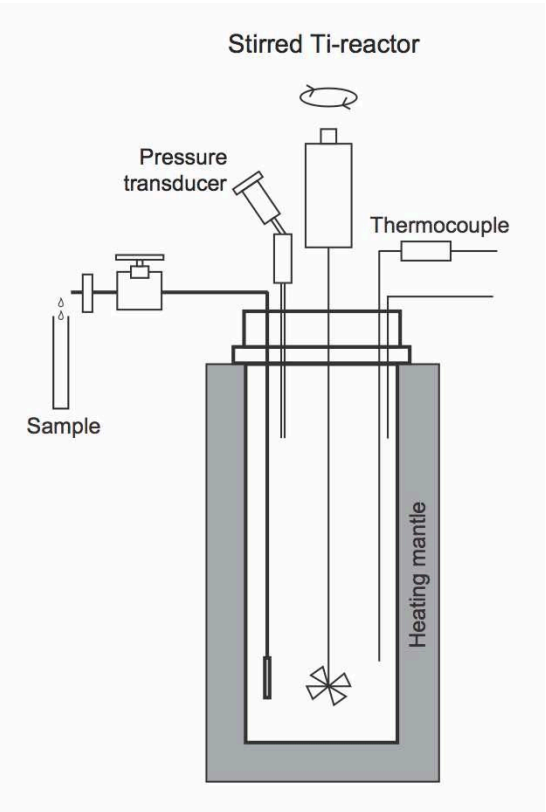

Figure 1. *A schematic picture of the experimental setup.*

Exp. #	Sample #	t (°C)	Duration (days)	pH_T [a]	$\sum CO_2$ (mmol/kg) [a]	r/w ratio[b]
e	1e-9e	150	25.3	6.48	20.9	0.13
f	1f-8f	150	12.7	6.59	5.17	0.134
g	1g-8g	150	6.8	6.96	6.36	0.137
h	1h-8h	150	28.8	6.63	5.72	0.151
k	1k-5k	150	6.8	6.82	13.7	0.133

[a] The inital $\sum CO_2$ and pH corresponds to the values measured in the first sample of each experimental run.
[b] The inital experimental rock to water ratio.

Table 1*. Summary of the experimental conditions.*

2.2 Sampling and analysis

Solution samples were collected regularly throughout the experiments. Samples for pH determination were analyzed immediately using a combination pH electrode (Cole-Parmer) calibrated with commercial buffer solutions. Samples for CO_2 analyses were collected into 0.01-0.1 M NaOH solutions to prevent degassing and analyzed immediately using a modified alkalinity titration (Stefánsson et al., 2007). Samples for Cl concentration determination were filtered through a 0.2 μm filter (cellulose acetate) followed by analysis using ion chromatography (Dionex-2000). Samples for Na, Mg, Si, Fe and isotopic

analyses were also filtered through a 0.2 μm filter, acidified to 1% HNO_3 (Merck Suprapur®) followed by analysis by ion chromatography for Na and Mg (Dionex-1000) and spectrophotometrically for Si and Fe (Dougan and Wilson, 1973; Fishman and Friedman, 1989). The analytical precision based on repeated analysis of an internal standard (GYG13) at the 95% confidence level was 4.4% for Na, 3.0% for Mg, 2.8% for Cl, 6.5% for Fe and 8.7% for Si.

Samples of the reacted solid were collected at the end of each experiment. These were dried at room temperature prior to analysis. The chemical composition of the material was determined using an electron microprobe (JEOL JXA-8200 Superprobe) with an accelerating voltage of 15 kV, a beam current of 15 nA, and a beam size of 5-1 μm. Unfortunately, most of the secondary phases (with the exception of magnesite) were too fine for point analysis even with a beam size of 1 μm, and were too small to be visible on polished samples. The surface morphology of the olivine grains and secondary phases were also studied by scanning electron microscope (SEM) equipped with EDS (HITACHI TM-3000) at an accelerating voltage of 15 kV with a working distance of 6.8 mm. Finally, the samples were analyzed using powder x-ray diffraction (XRD) with scans collected for 9 hours with a Bruker D8 Advanced (CuKα1, 1.5406 Å; 2θ range 3-90; 0.01°/step and 768 s/step). Patterns were compared to standard mineral files compiled in the PDF2 database (ICDD PDF-2 Powder Diffraction File Database) using the software code EVA.

2.3 Magnesium isotope analyses

Solution samples were prepared for Mg isotopic ($\delta^{25}Mg$ and $\delta^{26}Mg$) analysis by evaporating between 0.4 ml and 1.9 ml of solution in order to process ~2μg Mg per sample. Once dry each sample was dissolved in concentrated HNO_3, followed by drying and dissolution in 0.2 ml 0.8M HNO_3. For olivine, 5 mg of fresh sample was digested in HF-HNO_3 at 130 °C. Once dissolved the samples were dried down, dissolved in concentrated HCl, dried again, dissolved in concentrated HNO_3, dried down and then finally dissolved in 0.8M HNO_3. The solution and olivine samples were loaded onto acid-cleaned Teflon columns filled with a AG50W-X12 cation exchange resin to a height of 8.5 cm in 0.8M HNO_3. Magnesium separation followed the technique described by Pogge von Strandmann et al. (2011), with the sample being loaded and washed in 0.8M HNO_3 before the Mg fraction was eluted in 2M HNO_3. All samples were passed through the ion exchange columns twice to ensure complete separation from the other matrix elements, which was verified by ICP-MS analysis prior to isotopic analysis.

Isotopic analyses were performed on a ThermoFisher Scientific 'Neptune' Multi Collector Inductively Coupled Plasma Mass Spectrometer (MC-ICP-MS). Samples were introduced to the Ar Plasma in 2% aqueous HNO_3 using a standard sample induction system (SIS) attached to a PFA Teflon nebuliser. ^{24}Mg, ^{25}Mg, and ^{26}Mg were measured in low-resolution mode, with each analysis consisting of 1 block of 30 measurements per analysis. Solution concentrations of 600 ppb typically gave beam intensities of ~12 V for ^{24}Mg, with total procedural blanks having a negligible contribution of <12 mV. Isotopic compositions were determined via sample-standard bracketing, and are reported as $\delta^{26}Mg$ with respect to the DSM-3 standard (Galy et al., 2003). All sample analyses were run in duplicate, with the mean value and associated 2 standard error (se) reported (Table 4). Total procedural reproducibility was assessed by the analysis of the DSM, BCR, IAPSO and JDol standards during the same measurement session, with the corresponding $\delta^{26}Mg$ values of +0.01±0.02‰, -0.26±0.10‰, -0.83±0.02‰ and -2.32±0.01‰ being identical, or within

error, of those previously reported by Pearce et al. (2012). The long-term reproducibility (2σ) of the δ^{26}Mg analytical protocol at the University of Southampton, determined by repeat analyses of the DSM-3 Mg standard, is 0.07‰.

The δ^{25}Mg and δ^{26}Mg systematics of the dataset show mass dependent behavior. It follows that δ^{25}Mg ratios do not provide additional information of magnesium isotope systematics beyond that of δ^{26}Mg, thus although the δ^{25}Mg data are reported in this study (Table 4) only the δ^{26}Mg results are used in the models and discussion.

3 Numerical simulations

3.1 Geochemical reaction path modeling

Aqueous speciation, mineral saturation state and reaction path simulations were carried out using the PHREEQC geochemical program (Parkhurst and Appelo, 2013). The wateq.dat database used in these simulations was updated for the aqueous species, mineral solubilities and reaction kinetics of interest; the key thermodynamic and kinetic parameters used in the models are listed in Table 2. The general rate expression used to simulate the progress of olivine dissolution, formation of secondary minerals and the associated solution chemistry was

$$r_{\pm,T,i} = \pm\varsigma_i A_i \sum_i \left(k_{T,i} \prod_j a_j^x \right) (1 - \mathrm{SI}_i^n) \qquad (1)$$

where ς is the fraction of the surface area that is reactive having a value between 0 and 1 as in Přikryl et al. (2017), A is the surface area, k_T is the rate constant at given temperature and $\prod_j a_j^x$ as an activity expression for the j-th dissolved aqueous or surface species in solution. The saturation index to the power of n standing for order of reaction, SI, is defined as

$$SI = Q/K \qquad (2)$$

where Q is the activity product of the mineral reaction and K is the respective equilibrium solubility constant.

The surface area of the dissolved phases (olivine) was expressed as decreasing upon dissolution or loss of moles, assuming the grains to be spherical, i.e.

$$A = A^0 \left(\frac{m_t}{m_0}\right)^{2/3} \quad (3)$$

where m is number of moles. The rate expressions for secondary mineral formation represent crystal growth rates of a given mineral surface. However, the initial formation of minerals and mineral surfaces involves nucleation with $A = A_n$ whereas A_n is the total surface area of the nucleuses formed for a given mineral. In this study nucleation was not included into the rate expression as it requires knowledge of many parameters (De Yoreo and Vekilov, 2003; Karthika et al. 2016) undetermined in literature. Instead, the initial surface area of the secondary minerals was assigned with A_n representing 0.1-10% of the initial olivine surface area. The purpose of varying the A_n value was to study the effect of this initial surface area of secondary minerals on the model results. For the mineral formation, the value of ς was taken to be 1.

3.2 Isotope modeling

The variations in δ^{26}Mg were simulated as a part of the reaction path model in a similar manner as described previously (e.g., Stefánsson and Barnes, 2016; Stefánsson et al., 2016; 2017; Gunnarsson-Robin et al., 2017). The isotopic composition of the system (water-rock reaction in the reactor) is defined as;

$$\delta^{26}Mg^{system} = \sum_s x_s \delta^{26} Mg_s = \sum_i x_i \delta^{26} Mg_i \quad (4)$$

where *s* denotes the various sources and their isotope values. As olivine is the only source of Mg in the system, δ^{26}Mg of the system becomes equal to that of olivine ($\delta^{26}Mg^{system} = \delta^{26}Mg_{olivine}$). *i* denotes the i-th aqueous species and mineral being formed, and x_i is the mole fraction defined by;

$$x_i = \frac{n_i}{\sum_i n_i} \quad (5)$$

where *n* is the number of moles of Mg in the i-th aqueous species and/or minerals. Isotopic fractionation due to chemical reactions including formation of secondary minerals can be calculated as a function of reaction progress (Ξ), where

$$n_i = n_i^o + \upsilon_i \Delta \Xi \quad (6)$$

where $n_i^o and\ v_i$ are the initial mole number and stoichiometry coefficient of the i-th aqueous species and minerals.

The isotope values of aqueous species and minerals is subsequently calculated from,

$$\delta^{26}Mg^{system} = x_k\delta^{26}Mg_k + \sum_i x_i\,(\alpha_{i-k}(1000 + \delta^{26}Mg_k) - 1000) \quad (7)$$

$$\delta^{26}Mg_i = \alpha_{i-k}(1000 + \delta^{26}Mg_k) - 1000 \quad (8)$$

where *k* is the key aqueous species or mineral, here taken to be Mg^{2+}. α_{i-j} is the equilibrium isotope fractionation factor between the *i*-th and *k*-th phases defined by;

$$\alpha_{i-k} = \frac{1000 + \alpha^{26}Mg_i}{1000 + \alpha^{26}Mg_k} \quad (9)$$

The values for the fractionation factors between Mg^{2+} and various secondary minerals are listed in Table 2. The minerals included Mg-carbonates (magnesite and Mg-Fe carbonate solid solutions), talc, brucite and chrysotile (which was taken to be equivalent to that of chlorite). The values of the fractionation factors are based on those reported by Pearce et al. (2012), Beinlich et al. (2014), Wimpenny et al. (2014) (Fig. 2). In order to obtain the fractionation factors under the experimental conditions of 150°C, the reported fractionation factors were fitted assuming a linear relationship between $10^3\ln\alpha$ and $1/T^2$ with a zero intercept at infinite temperature ($\alpha \rightarrow 1$ at $1/T^2 \rightarrow 0$) (Fig. 2), similar to Huang et al. (2013).

Reaction	$10^3\ln\alpha$ (150°C)	fit (T in Kelvin)	Source
talc-Mg^{2+}(aq)	0.431	$10^3\ln\alpha = 0.0771\ (10^6/T^2)$	Beinlich et al. (2014), extrapolated
chrysotile-Mg^{2+}(aq)	-0.25	$10^3\ln\alpha = -0.046\ (10^6/T^2)$	Beinlich et al. (2014), extrapolated
brucite-Mg^{2+}(aq)	0.36	$10^3\ln\alpha = 0.064\ (10^6/T^2)$	Wimpenny et al. (2014), extrapolated
magnesite-Mg^{2+}(aq)	-1.19	$10^3\ln\alpha = -0.207\ (10^6/T^2)$	Pearce et al. (2012), Beinlich et al. (2014)

Table 2. *$\delta^{26}Mg$ fractination factors between minerals and Mg^{2+} in aqueous solutions*.

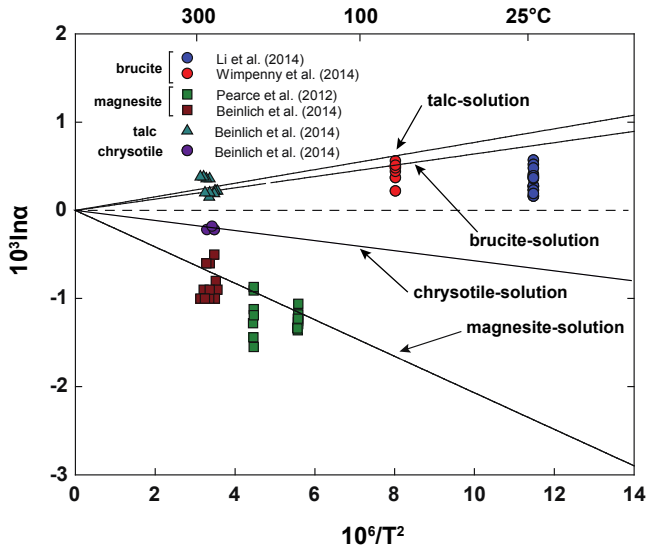

Figure 2. *$\delta^{26}Mg$ fractionation factors between minerals and dissolved Mg^{2+}. The lines represent regressions through the data points assuming $\alpha \rightarrow 1$ when $1/T^2 \rightarrow 0$. The data are based on results reported by Wimpenny et al. (2014), Li et al. (2014), Pearce et al. (2012) and Beinlich et al. (2014) and consistent with values of Rustad et al. (2010) and Schauble (2011).*

4 Results

4.1 Solution composition

Two types of experiments were conducted at 150°C: (1) low CO_2 concentrations of 5.17 - 6.36 mmol/kg (Experiments F, G and H), and (2) elevated CO_2 concentrations of 13.7 - 20.9 mmol/kg (Experiments K and E). The changes in solution chemistry as a function of reaction time are given in Table 3. Initially the pH of the solutions was ~6.5 and increased to between ~6.7 and ~7.5 with reaction time. The aqueous CO_2 concentration decreased as pH increased. The dissolved concentrations of Si and Mg increased rapidly during the first hours, reaching values of Si ~0.4-1.2 and Mg ~0.7-1.1 mmol/kg after ~30 minutes followed by a decrease with experimental duration after ~1-10 days. An increase in Si concentration observed in experiment E from day 2 was significant compared to runs with lower CO_2 concentration. The high CO_2 experiments resulted in greater olivine mass dissolved, and a faster intake of Mg ions by secondary phases from solution relative to the low CO_2 experiments. Very low concentrations (generally less than ~1 µmol/kg) were also initially observed for Fe.

Variations in the $\delta^{26}Mg$ composition of the reacting fluid were determined together with the composition of the reacting olivine in experiment E that showed the greatest change in Mg concentration. The results are given in Table 4. The $\delta^{26}Mg$ ratio measured for olivine was -0.22±0.07‰, no variation between initial and reacted material was observed. This is

similar to the previously observed δ^{26}Mg ratio of unaltered oceanic crust and mantle xenolites of -0.35 to -0.18‰ (e.g., Wiechert and Halliday, 2007; Teng et al., 2007, 2010, 2015; Liu et al., 2017). The δ^{26}Mg ratios of the experimental solutions ranged from -0.27 to +0.35‰, was low initially, increased during the first five days followed by a relatively steady value.

Exp. #	Temp.	time	pH / 22°C	ΣCO$_2$	Si	Mg	Fe$_{tot}$	Na	Cl
	°C	days		mmol/kg	mmol/kg	mmol/kg	µmol/kg	mmol/kg	mmol/kg
1e	150	0.02	6.48	20.9	1.27	1.12	0.64	31.1	27.9
2e	150	0.71	6.90	18.6	0.841	1.33	0.37	30.6	26.7
3e	150	2.60	6.73	17.2	1.15	1.24	2.8	31.0	28.5
4e	150	4.60	6.80	15.8	1.33	1.09	0.61	31.3	28.5
5e	150	6.79	6.87	13.7	1.63	0.783	0.69	31.0	29.0
6e	150	8.63	6.84	13.2	2.06	0.640	0.74	31.4	29.1
7e	150	10.56	6.93	11.3	1.33	0.519	1.3	31.2	29.0
8e	150	21.48	6.91	9.41	1.22	0.338	1.4	30.9	28.4
9e	150	25.31	7.07	8.15	0.982	0.298	1.7	31.3	28.7
1f	150	0.03	6.59	5.17	n.a.	0.822	0.8	10.3	11.0
2f	150	0.71	7.22	4.76	0.494	1.01	1.1	10.7	10.6
3f	150	2.69	7.41	5.28	0.297	0.879	0.44	10.0	10.8
4f	150	4.81	7.29	4.77	0.261	0.860	1.7	10.4	10.7
5f	150	6.69	7.32	4.96	0.228	0.821	1.0	10.4	10.9
6f	150	8.79	7.26	3.97	0.227	0.782	0.91	10.3	11.0
7f	150	10.75	7.31	4.45	0.172	0.669	0.53	10.3	10.9
8f	150	12.67	7.36	4.14	0.184	0.597	0.96	10.4	11.2
1g	150	0.04	6.96	6.36	0.493	0.688	0.75	10.5	10.5
2g	150	0.77	7.29	5.24	0.287	0.783	0.53	10.7	10.5
3g	150	1.90	7.37	5.24	0.244	0.720	0.31	10.4	10.5
4g	150	2.81	7.33	5.19	0.210	0.683	0.34	10.6	10.3
5g	150	3.94	7.44	4.71	0.236	0.610	0.54	10.6	10.5
6g	150	5.00	7.45	4.67	0.142	0.572	0.51	10.7	10.5
7g	150	5.79	7.43	4.44	0.221	0.520	0.88	10.6	10.4
8g	150	6.81	7.41	4.44	0.299	0.475	0.81	10.6	10.3
1h	150	0.04	6.63	5.72	0.773	0.718	0.17	10.7	10.8
2h	150	2.00	6.76	5.64	0.324	0.775	79	10.4	10.9
3h	150	5.06	6.87	5.92	0.910	0.748	33	10.3	10.9
4h	150	9.85	7.16	4.99	1.032	0.613	20	10.3	10.8
5h	150	14.94	6.91	5.36	0.179	0.493	16	10.6	10.7
6h	150	19.83	7.09	5.26	0.216	0.405	17	10.6	10.8
7h	150	23.83	7.07	5.03	0.134	0.374	12	10.4	12.2
8h	150	28.81	7.20	2.61	0.146	0.314	9.3	10.4	10.7
1k	150	0.17	6.82	13.7	0.425	0.977	3.5	28.1	26.0
2k	150	0.90	7.04	12.4	0.443	0.912	3.8	28.3	25.9
3k	150	2.75	7.01	11.9	0.513	0.679	6.2	28.3	26.2
4k	150	4.77	7.13	9.96	0.531	0.441	10	28.0	26.0
5k	150	6.81	7.35	8.64	0.549	0.394	14	28.2	26.1

Table 3. *Experimental solutions composition.*

Sample	δ^{25}Mg ‰		δ^{26}Mg ‰	
/Exp.	Mean	2 s.e.	Mean	2 s.e.
Fo_{93} - Unreacted	-0.121	0.006	-0.224	0.009
Fo_{93} - Altered	-0.108	0.007	-0.221	0.010
e1	-0.070	0.010	-0.136	0.018
e2	-0.154	0.009	-0.266	0.018
e3	0.058	0.008	0.105	0.015
e4	0.150	0.008	0.317	0.016
e5	0.168	0.009	0.354	0.016
e6	0.155	0.007	0.317	0.014
e7	0.149	0.011	0.292	0.019
e8	0.112	0.006	0.255	0.011
e9	0.158	0.007	0.319	0.012

Table 4. *Isotopic composition of forsterite and experimental fluid in the run E. Long-term analytical reproducibility (2σ) is 0.07 ‰.*

4.2 Secondary mineralogy

The identified secondary minerals were magnesite, chrysotile/lizardite, amorphous silica and halite. Halite was considered to form upon quenching of the experimental systems. SEM images of the alteration products, altered olivine surfaces are shown in Figure 3. The unaltered olivine surfaces showed pristine and smooth surfaces with sharp mineral edges. Upon dissolution, conical or funnel-shaped etch pits were observed to form along the mineral edges and within the previously smoothed surfaces. The composition of the chrysotile/lizardite was determined to be $Mg_{2.87}Fe_{0.19}Si_{1.96}O_5(OH)_4$ and the composition of magnesite was $Mg_{(0.92\text{-}0.95)}Fe_{(0.08\text{-}0.05)}CO_3$. No precipitating iron oxides were observed, suggesting that Fe released from the dissolving olivine was mostly incorporated as impurities into the magnesite and/or chrysotile/lizardite solid solutions.

The changes in mineralogy as a function of reaction time at constant initial CO_2 (~6 mmol/kg; Experiments G and H) are shown in Figure 3 (d and e). Small single euhedral crystals of magnesite formed up to 1 μm. Randomly distributed needle shaped formations, up to 0.5 μm in length, are chrysotile/lizardite. No major dissolution features on the olivine surfaces are observed after 7 days (Fig. 3d). After two weeks, no large changes were observed except magnesite crystals grew and became larger, up to 3 μm in size. After 4 weeks of interaction (Fig. 3e), the precipitation pattern of magnesite was characteristic with euhedral crystals up to 5 μm in diameter. A thin layer of coarse alteration coating developed partly over the olivine surfaces, typically as scales sticking out from the surface and no bigger than 0.5 μm; this is an early stage of chrysotile/lizardite nucleation and serpentinization. Dissolution etch pits were also clearly observed on the olivine grain edges after four weeks of interaction.

The effect of changing initial CO_2 concentration (Experiments H and E) on the olivine alteration mineralogy is shown in Figure 3 (e and f). At low CO_2 (~6 mmol/kg; Exp. G, F, H; Fig. 3d, e), magnesite crystals were observed to form along the olivine edges and within surface cleavages whereas small chrysotile/lizardite needles formed randomly over the whole olivine surface. However, for experiments with initially elevated CO_2 (~21 mmol/kg, Exp. E; Fig. 3f), the magnesite crystals grew up to 10 µm in size with some of the olivine grains completely coated with conglomerates of euhedral magnesite crystals after 25 days. Honeycomb structures or mesh texture of chrysotile/lizardite coated some of the olivine surface and formed conglomerates around the magnesite crystals.

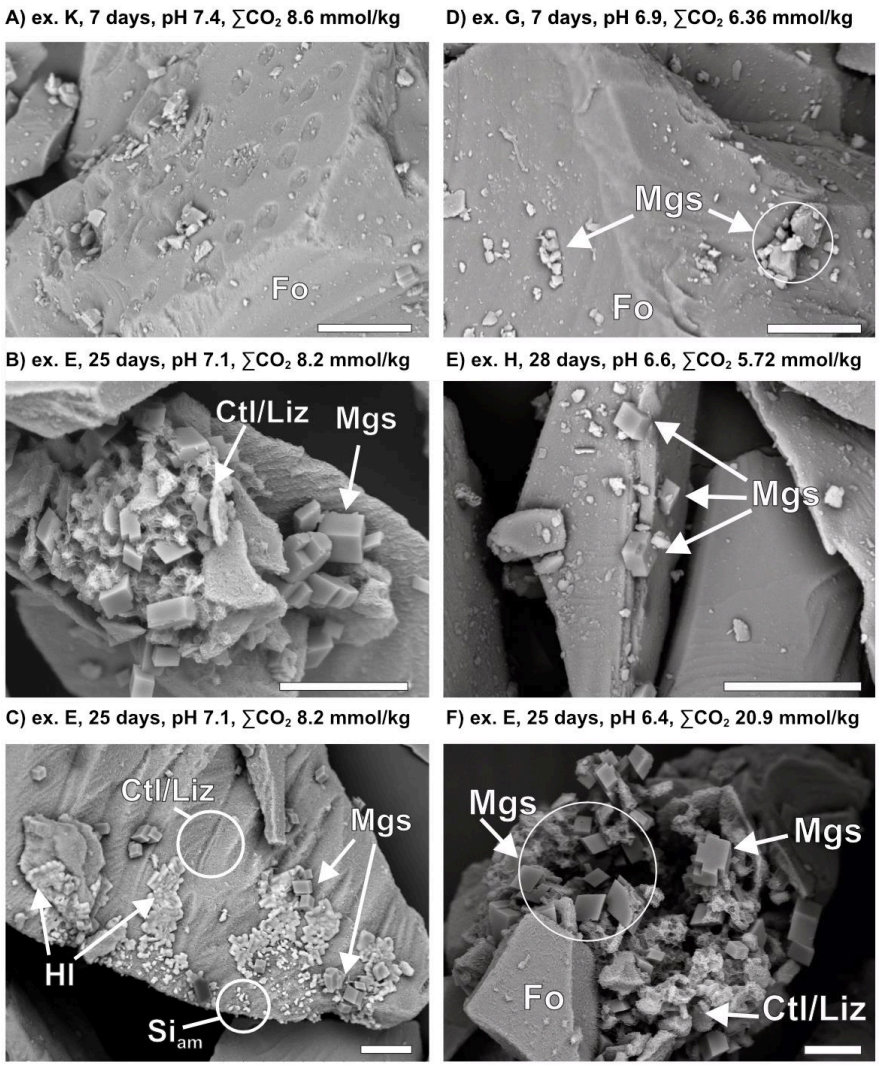

Figure 3. *SEM photomicrographs with typical surface of (A) reacted olivine surface showing the conical or funnel-shaped etch pits, B) euhedral crystals of magnesite and conglomerates of chrysotile microtubes covering Fo_{93} grains, and (C) secondary magnesite and chrysotile together with spherical amorphous silica and halite flakes. Experimental conditions presented are the end of the runs (A, B, C). Magnesite formation as a function of reaction time for solutions with initially similar CO_2 concentrations (D and E), and as a function of initial low and elevated CO_2 concentrations (E and F). At low initial CO_2 concentrations of ~6 mmol/kg euhedral crystals of magnesite were observed to grow with reaction time from 1 to 5 µm in about a 3 weeks (D and E). However, the quantity and size of magnesite crystals was predominantly found to depend on initial CO_2 concentration (E and F); with elevated CO_2 concentration the magnesite grew to ~10 µm. Starting experimental pH and CO_2 conditions are presented (D, E, F). Scale bar is 15 µm on all presented SEM images, mineral abbreviations are: Ctl-chrysotile, Fo-forsterite, Hl-halite, Mgs-magnesite, Si am-amorphous silica.*

5 Discussion

5.1 Olivine alteration

The experimental results are compared with the calculated solution composition and mineralogy in Figures 4 and 5. The experimental solution composition was reasonable well reproduced by the geochemical models (Fig. 4). A declining trend for CO_2 concentration was observed in all experiments and models with time. Similarly pH values increased in both the experiments and models, reflecting the decreasing acid supply in the system. Some discrepancies were observed for Si (Fig. 4c), and are considered to be related to an initial non-stoichiometric leaching of Si from the olivine. For Mg, the modeled concentrations were lower than the experimental data until ~3 days of interaction. Afterwards a close match was observed between experiments and models. It is likely that the difference between model and experimental data reflects an initial overestimation of the extent of secondary mineral precipitation, as the changes in CO_2 concentration showed good agreement between modeled and experimental system (Fig 4).

The secondary mineralogy predicted by the geochemical models showed a clear trend with reaction time and solution pH (Fig. 5). Initially at pH<6.5, chrysotile and Mg-Fe carbonate solid solutions dominated the alteration mineralogy whereas with reaction time and pH increase brucite also became important. In the experiments, brucite was not observed as a part of the alteration product, as the pH of the solutions was not high enough for brucite formation at the end of the experiments. The amount of initial CO_2 (Fig. 5a, b) reflected the total mass of dissolved olivine and of formed secondary minerals. High CO_2 run dissolved ~6 times more olivine than low CO_2 run. This resulted in one order of magnitude difference in precipitating magnesite and talc. However, relative proportions between forming minerals were similar in both scenarios.

The results of the experiments and geochemical modeling demonstrate that the main factors controlling olivine-fluid interaction in CO_2-rich solutions are the extent of the reaction (Ξ) (or reaction time) and pH. Solution pH is in turn controlled by acid supply and the extent of reaction. For olivine alteration where CO_2 is the major acid, two alteration stages were distinguished based on the solution pH (Figs. 4 and 5): (1) stage **I** was characterized by mildly acid to neutral pH values, buffered by dissolved CO_2 and H^+

consumption upon olivine dissolution, and by the formation of Mg-Fe carbonate solid solutions and chrysotile; stage **II** was characterized by progressive olivine alteration, decrease of CO_2 concentration due to carbonate mineral formation and pH increase to >8. Under the alkaline conditions chrysotile, brucite and Mg and Fe containing carbonates were formed. Similar pH effects on the alteration product have been observed during fluid-rock reactions with basaltic glasses (Gysi and Stefánsson, 2012a, 2012b).

The mass of secondary minerals formed was found to largely depend on the reactive surface area of the olivine (Fig. 5c). The best fit corresponded to 30% ($\varsigma = 0.3$) and 80% ($\varsigma = 0.8$) (Eqn. 1) of the total olivine geometric surface at low- and high CO_2 concentration, respectively. In contrast, the effects of the nucleation surface area (A_n) of secondary minerals were found to have a limited effect on the mass of secondary minerals formed. This observation is related to the fact that the secondary minerals were close to equilibrium and that their formation rates were primarily driven by the affinity term ($1\text{-}SI^m$), rather than the surface area of the nuclei and crystals.

The rate limiting reaction controlling elemental transfer is generally thought to be the dissolution rate of the primary mineral. However, as pointed out by Saldi et al. (2012), this may not always be the case, as the precipitation rate of magnesite is 3-5 orders of magnitude lower than the corresponding dissolution rate for olivine. Here, we observed that olivine alteration rate primarily depends on pH. At pH ~6.5, the dissolution rate of olivine was slightly greater than the formation rate of carbonates, demonstrating that the rate limiting factor of carbonation in the system was not the dissolution rate of olivine, but the precipitation rate of the carbonates. With increasing reaction progression, the pH increased to >8. Under these conditions the dissolution rate of olivine became slower than the formation rates of all secondary minerals, demonstrating that the rate limiting factors during water-rock interaction of olivine was its dissolution rate.

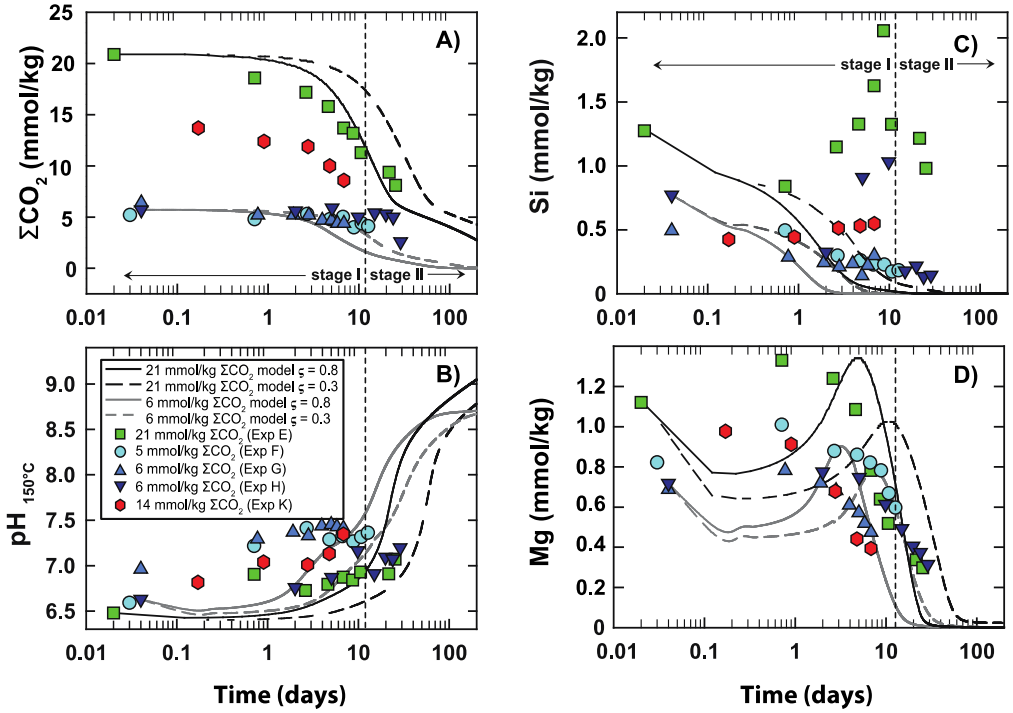

Figure 4. *Measured changes in pH, CO_2, Mg and Si concentrations in the experimental solutions as a function of time and aqueous CO_2 concentration at 150°C. The symbols denote the different CO_2 concentrations used in each experimental run, and the curved lines the results of the geochemical model. Two different models are shown, at low and elevated CO_2 concentrations of 6 and 21 mmol/kg, respectively, with low and high fraction of olivine reactive surface areas 0.3 and 0.8 (ς). The vertical dashed line separates the two stages of olivine alteration inferred by these experiments (see text for details).*

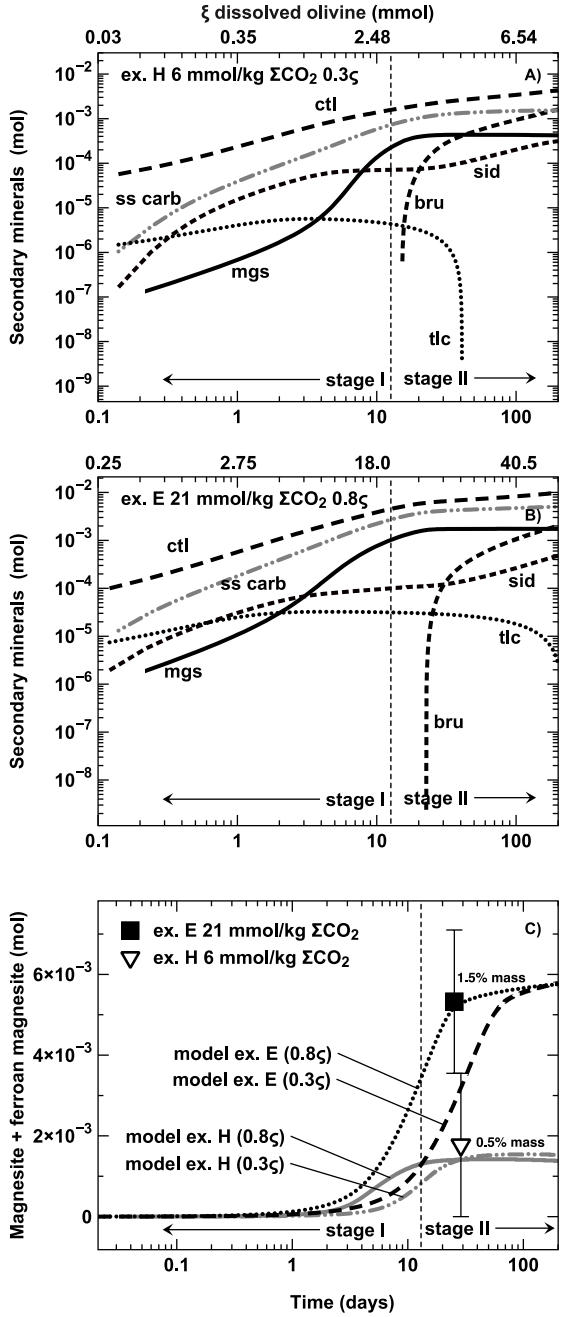

Figure 5. *Mass of secondary minerals precipitated according to the geochemical modeling for low (A) and high (B) initial CO_2 concentration. Experimental magnesite mass precipitated was in agreement with results from the geochemical model (C). Quantification of magnesite is based on XRD analysis, SEM observations versus the geochemical model. ς is the fraction of total reactive surface area applied in the model. Ctl: chrysotle; ss carb: Mg-Fe carbonate solid solutions; mgs: magnesite; sid: siderite; tlc: talc; bru: brucite.*

5.2 Magnesium isotope systematics during olivine carbonation and serpentinization

The only source of Mg in experimental system was the olivine powder, which had a starting δ^{26}Mg ratio of -0.22±0.07‰. The initial alteration of the olivine in CO_2-rich water (stage **I**) was characterized by Mg leaching from the olivine, buffering of the pH at ~6.5 and formation of Mg-Fe carbonates and chrysotile. Assuming equilibrium fractionation between the solution and the Mg-Fe carbonates (α = 0.99975) and chrysotile (α = 0.9988) at 150°C, modeled olivine alteration resulted in the solution becoming enriched in ^{26}Mg and the alteration product enriched in ^{24}Mg. Consequently, the δ^{26}Mg ratio of the solution becomes higher than the system or olivine and the δ^{26}Mg ratio of the alteration product becomes lower. This is indeed what was observed experimentally (Fig. 6), as upon initial leaching the δ^{26}Mg ratio of the solution was similar to that of olivine (between -0.27 and -0.14‰), whereas the δ^{26}Mg composition of the solution increased to between +0.26 and +0.35‰ following the formation of Mg-Fe carbonates and chrysotile.

Upon further alteration of olivine (stage **II**) the CO_2 concentration decreased due to carbonate mineralization and the solution pH increased to >8 with chrysotile and eventually brucite becomes the dominant alteration product. The equilibrium fractionation factor between the solution and brucite (α = 1.0004) and talc (α = 1.0004) resulted in the solution becoming enriched in ^{24}Mg and the alteration product enriched in ^{26}Mg, or the reverse δ^{26}Mg systematics compared to initial olivine alteration.

These results suggest that changes in the δ^{26}Mg composition of the solution may be used to trace the extent of olivine alteration via carbonation and serpentinization reactions: Figure 6 demonstrates that the δ^{26}Mg composition shifts rapidly under close to equilibrium conditions, before stage **II** is reached. This is most likely caused by rapid element transfer during stage **I,** where olivine dissolution and carbonation reactions occur under far-from equilibrium conditions. This indicates that the dominant reaction pathway can be identified with δ^{26}Mg, for instance in an ultramafic CO_2 sequestration system and therefore verify ongoing carbonate formation. The extensive precipitation of Mg-carbonate minerals (presented in studied system as stage **I**) with light δ^{26}Mg composition will be reflected with the solution enriched in δ^{26}Mg.

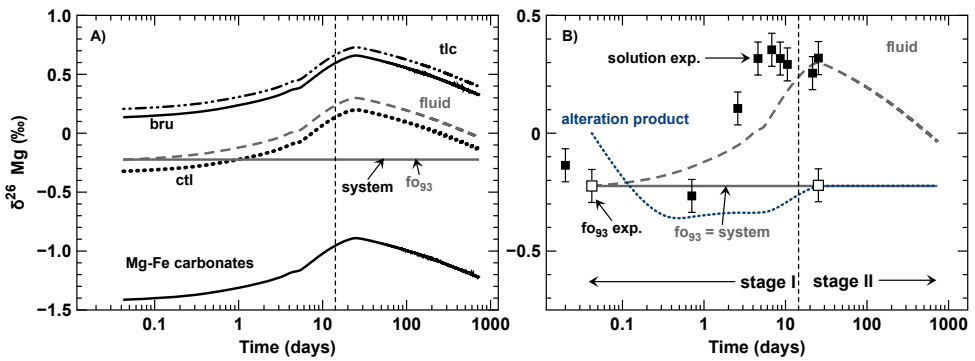

Figure 6. *(A) The result of the δ^{26}Mg isotopic systematics of the secondary minerals obtained from the isotope modeling. (B) Comparison of the measured and calculated δ^{26}Mg isotopic systematics of the water. Also shown are the δ^{26}Mg for the bulk alteration product calculated using the isotope modeling results.*

5.3 Comparison with natural analogues

The results of these experiments and isotopic modeling are compared with naturally altered basalts and ground- and geothermal water in Figure 7. The higher δ^{26}Mg values of the solutions measured in this study (relative to the starting olivine composition) are similar to the elevated values of +0.23 ‰ to +0.85 ‰ observed in the ground- and geothermal waters of the basaltic terrain in Iceland (Pogge von Strandmann et al., 2008). This positive shift in the δ^{26}Mg composition of the fluid is likely to be due to the formation of clay minerals (similar to serpentine minerals) and carbonate minerals that are enriched in ^{24}Mg relative to the olivine and bulk Mg of the basalts. The δ^{26}Mg compositions of altered oceanic basalts in the western Pacific reveal large isotopic fractionation during oceanic crust alteration (Huang, 2013), with the most negative values being associated with the carbonation of the basalts, and less negative values associated with serpentinization. These observations are in good agreement with our isotopic modeling, where the carbonates (and to lesser extend chrysotile) are found to be enriched in the ^{26}Mg isotope relative to olivine and the solution, whereas extensive serpentinization of oceanic crust and formation of brucite and talc may result in the reversed δ^{26}Mg, with these minerals becoming enriched in ^{24}Mg and the resulting solutions enriched in ^{26}Mg.

The hydrothermal carbonation of ultramafic rocks (and by analogy mafic rocks) is thought to be accompanied by significant inter-mineral fraction resulting in the formation of ^{24}Mg enriched magnesite and ^{26}Mg enriched talc (Beinlich et al. 2014). The field results of Beinlich et al. (2014) suggest that Mg isotopes may not be fractionated during serpentinization reactions, as their olivine exhibits and invariant Mg isotope ratio. This study is in agreement that formation of Mg-bearing carbonates during ocean water circulation through mid-ocean ridge flanks at hydrothermal conditions forms a sink for isotopically light Mg. We show, the late stage serpentinization with limited Mg supply from slowly dissolving olivine and slowly forming chrysotile-brucite caused hydrothermal water to be progressively enriched in ^{24}Mg eventually. The isotopic composition of water therefore points out sensitivity to formation and dissolution rates of different minerals at different settings during reaction progress. This is possible to track by application of kinetic Mg isotope fractionation for Mg-rich rock-forming minerals, which were calibrated by laboratory experiments, theoretical calculation and analysis of natural samples.

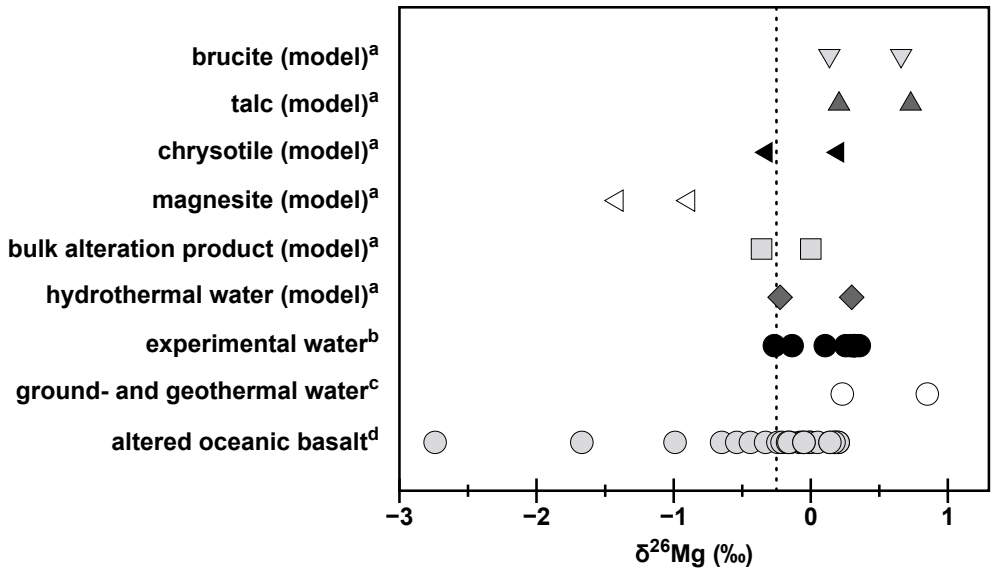

Figure 7. *Comparison of δ^{26}Mg ratios of natural fresh and altered mafic and ultramafic rocks, natural ground- and hydrothermal water and the results obtained here experimentally and using isotope modeling (min-max values): [a] this study, [b] this study, [c] Pogge von Strandmann et al. (2008), [d] Huang (2013). The vertical line represents the average Mg isotopic composition of the mantle, i.e., bulk Earth (Teng, 2017).*

6 Conclusions

Olivine carbonation and serpentinization in CO_2-rich fluids at 150˚C was studied experimentally and using geochemical modeling. The alteration of olivine was found to be incongruent and dependant on reaction time, with two main stages being identified: Stage **I** was characterized by a low pH (buffered at ~6.5), during which olivine dissolved to form Mg-Fe carbonate solid solutions and minor chrysotile. Assuming equilibrium fractionation, the Mg-rich carbonates and chrysotile forming during this interval preferentially incorporated ^{24}Mg, such that the alteration product had lower δ^{26}Mg values and the solution higher δ^{26}Mg relative to the olivine that provided the only source of Mg in the experiments. Stage **II** continued the extensive alteration of olivine, with the carbonation reactions ultimately driving a decrease of CO_2 concentration and associated increase in pH (to >8), under which chrysotile and brucite became the dominant alteration minerals. As a result, the alteration product becomes progressively enriched in ^{26}Mg relative to the solution that eventually may display lower δ^{26}Mg ratios than for the olivine source.

It follows that changes in the δ^{26}Mg composition of the fluid phase and alteration products formed during olivine alteration primarily reflects the type and quantity of secondary Mg minerals formed, and thus in turn depend on pH and extent of reaction. Comparison of the experimental and isotope modeling results with ground- and geothermal water of basaltic terrains indicate that δ^{26}Mg systematics of the natural waters are controlled by mafic rock leaching and incorporation of ^{24}Mg into carbonates and Mg-Si minerals like chrysotile and

possibly clays. The results also demonstrate that isotope fractionation upon geochemical processes like water-rock interaction may exceed differences observed among various sources, highlighting the effects and importance of chemical reactions on the isotope characteristics of reactive elements like magnesium.

Tracking Mg isotope exchange mechanism and rates relevant to hydrothermal olivine alteration in oceanic crust showed formation of Mg-bearing carbonates at mid-ocean ridge flanks indeed forms a sink for isotopically light Mg. Dissolution and precipitation of different minerals varied with reaction extent and so the isotopic composition of water. This is possible to follow with Mg isotope fractionation for Mg-rich rock-forming minerals. Moreover, Mg isotopic signatures indicate application as a tracer during CO_2 sequestration.

Associated content

Appendix 1 is thermodynamic and kinetic dataset used for the kinetic reaction path simulations.

Acknowledgements

We would like to thank Juan D. Rodriguez-Blanco and Matthijs A. Smit for help with XRD and EMPA measurements. This research was made possible by a Marie Curie grant from the European Commission in the framework of the MINSC ITN (Initial Training Research network), Project number 290040.

References

Andreani, M., Luquot, L., Gouze, P., Godard, M., Hoisé, E. and Gibert, B. (2009) Experimental study of carbon sequestration reactions controlled by the percolation of CO_2 -rich brine through peridotites. Env. Sci. Technol. **43**, 1226–1231.

Béarat, H., McKelvy, M.J., Chizmeshya, A.V.G., Gormley, D., Nunez, R., Carpenter, R.W., Squires, K. and Wolf, G.H. (2006) Carbon sequestration via aqueous olivine mineral carbonation: Role of passivating layer formation. Env. Sci. Technol. **40**, 4802–4808.

Beinlich, A., Mavromatis, V., Austrheim, H. and Oelkers, E. H. (2014) Inter-mineral Mg isotope fractionation during hydrothermal ultramafic rock alteration–Implications for the global Mg-cycle. Earth Planet Sc. Lett. **392**, 166-176.

Berndt, M.E., Allen, D.E. and Seyfried, W.E. (1996) Reduction of CO_2 during serpentinization of olivine at 300 C and 500 bar. Geology **24**, 351–354.

Brueckner, H.K., Carswell, D.A., Griffin, W.L., Medaris, L.G., Van Roermund, H.L.M. and Cuthbert, S.J. (2010) The mantle and crustal evolution of two garnet peridotite suites

from the Western Gneiss Region, Norwegian Caledonides: An isotopic investigation. Lithos **117**, 1–19.

Carroll, S., Mroczek, E., Alai, M. and Ebert, M. (1998) Amorphous silica precipitation (60 to 120°C): Comparison of laboratory and field rates. Geochim. Cosmochim. Acta **62**, 1379–1396.

Daval, D., Sissmann, O., Menguy, N., Saldi, G.D., Guyot, F., Martinez, I., Corvisier, J., Garcia, B., Machouk, I., Knauss, K.G. and Hellmann, R. (2011) Influence of amorphous silica layer formation on the dissolution rate of olivine at 90°C and elevated pCO_2. Chem. Geol. **284**, 193–209.

Dougan, W.K. and Wilson, A.L. (1973) Absorbtiometric determination of iron with TPTZ. Water Treat. Exam. **22**, 110.

Etiope, G. and Sherwood Lollar, B. (2013) Abiotic methane on Earth. Rev. Geophys. **51**, 276-299.

Fishman M. J. and Friedman L. C. (1989) Techniques of Water Resources Investigations of the United States Geological Survey. Chapter A1: Methods for determination of inorganic substances in water and fluvial sediments, 3rd ed., Book 5, Laboratory analysis. United States Government Printing Office.

Foster, G.L., Pogge von Strandmann, P.A. and Rae, J.W.B. (2010) Boron and magnesium isotopic composition of seawater. Geochem. Geophys. **11**(8).

Galy, A., Yoffe, O., Janney, P.E., Williams, R.W., Cloquet, C., Alard, O., Halicz, L., Wadhwa, M., Hutcheon, I.D., Ramon, E. and Carignan, J. (2003) Magnesium isotope heterogeneity of the isotopic standard SRM980 and new reference materials for magnesium-isotope-ratio measurements. J. Anal. At. Spectrom. **18**, 1352–1356.

Giammar, D.E., Bruant, R.G. and Peters, C.A. (2005) Forsterite dissolution and magnesite precipitation at conditions relevant for deep saline aquifer storage and sequestration of carbon dioxide. Chem. Geol. **217**, 257–276.

Gíslason, S.R., Wolff-Boenisch, D., Stefánsson, A., Oelkers, E.H., Gunnlaugsson, E., Sigurdardóttir, H., Sigfússon, B., Broecker, W.S., Matter, J.M. and Stute, M. (2010) Mineral sequestration of carbon dioxide in basalt: A pre-injection overview of the CarbFix project. Int. J. Greenh. Gas Control **4**, 537–545.

Gunnarsson, I., and Arnórsson, S. (2005) Precipitation of poorly crystalline antigorite under hydrothermal conditions. Geochim. Cosmochim. Acta **69**, 2813-2828.

Gunnarsson-Robin, J., Stefánsson, A., Ono, S. and Torssander, P. (2017) Sulfur isotopes in Icelandic thermal fluids. J. Volcanol. Geotherm. Res. **346**, 161-179.

Gysi, A.P. and Stefánsson, A. (2011) CO_2–water–basalt interaction. Numerical simulation of low temperature CO_2 sequestration into basalts. Geochim. Cosmochim. Acta **75**, 4728–4751.

Gysi, A.P. and Stefánsson, A. (2012a) Experiments and geochemical modeling of CO_2 sequestration during hydrothermal basalt alteration. Chem. Geol. **306-307**, 10–28.

Gysi, A.P. and Stefánsson, A. (2012b) Mineralogical aspects of CO_2 sequestration during hydrothermal basalt alteration — An experimental study at 75 to 250°C and elevated pCO_2. Chem. Geol. **306-307**, 146–159.

Holland, T.J.B. and Powell, R. (2011) An improved and extended internally consistent thermodynamic dataset for phases of petrological interest, involving a new equation of state for solids. J. Metamorph. Geol. **29**, 333–383.

Hövelmann, J., Austrheim, H., Beinlich, A. and Anne Munz, I. (2011) Experimental study of the carbonation of partially serpentinized and weathered peridotites. Geochim. Cosmochim. Acta 75, 6760–6779.

Huang, F., Chen, L., Wu, Z. and Wang, W. (2013) First-principles calculations of equilibrium Mg isotope fractionations between garnet, clinopyroxene, orthopyroxene, and olivine: implications for Mg isotope thermometry. Earth Planet. Sci. Lett. **367**, 61-70.

Huang, J., Li, S.G., Xiao, Y., Ke, S., Li, W.Y. and Tian, Y. (2015) Origin of low $\delta^{26}Mg$ Cenozoic basalts from South China Block and their geodynamic implications. Geochim. Cosmochim. Acta **164**, 298-317.

Huang, K-J. (2013) The behavior of magnesium isotopes during low temperature water–rock interactions. PhD dissertation. China University of Geosciences, Wuhan, China.

James, R.H., Allen, D.E. and Seyfried, W.E. (2003) An experimental study of alteration of oceanic crust and terrigenous sediments at moderate temperatures (51 to 350 °C): Insights as to chemical processes in near-shore ridge-flank hydrothermal systems. Geochim. Cosmochim. Acta **67**, 681–691.

Janecky, D.R. and Seyfried, W.E. (1986) Hydrothermal serpentinization of peridotite within the oceanic crust: Experimental investigations of mineralogy and major element chemistry. Geochim. Cosmochim. Acta **50**, 1357–1378.

Jones, L.C., Rosenbauer, R., Goldsmith, J.I. and Oze, C. (2010) Carbonate control of H_2 and CH_4 production in serpentinization systems at elevated P-Ts. Geophys. Res. Lett. **37**.

Klein, F. and Garrido, C.J. (2011) Thermodynamic constraints on mineral carbonation of serpentinized peridotite. Lithos **126**, 147–160.

King, H.E., Plümper, O. and Putnis, A. (2010) Effect of secondary phase formation on the carbonation of olivine. Env. Sci. Technol. 44, 6503–6509.

Lafay, R., Montes-Hernandez, G., Janots, E., Chiriac, R., Findling, N. and Toche, F. (2012) Mineral replacement rate of olivine by chrysotile and brucite under high alkaline conditions. J. Cryst. Growth **347**, 62–72.

Li, W., Beard, B. L., Li, C. and Johnson, C. M. (2014) Magnesium isotope fractionation between brucite [$Mg(OH)_2$] and Mg aqueous species: implications for silicate weathering and biogeochemical processes. Earth Planet. Sci. Lett **394**, 82-93.

Ling, M.X., Sedaghatpour, F., Teng, F.Z., Hays, P.D., Strauss, J. and Sun, W. (2011) Homogeneous magnesium isotopic composition of seawater: an excellent geostandard for Mg isotope analysis. Rapid Comm. Mass Spectrom. **25**, 2828-2836.

Liu, P.P., Teng, F.Z., Dick, H.J., Zhou, M.F. and Chung, S.L. (2017). Magnesium isotopic composition of the oceanic mantle and oceanic Mg cycling. Geochim. Cosmochim. Acta **206**, 151-165.

Marcaillou, C., Muñoz, M., Vidal, O., Parra, T. and Harfouche, M. (2011) Mineralogical evidence for H_2 degassing during serpentinization at 300°C/300bar. Earth Planet. Sci. Lett. **303**, 281–290.

Marieni, C., Henstock T. J. and Teagle, D.A (2013) Geological storage of CO_2 within the oceanic crust by gravitational trapping. Geophys. Res. Lett. **40**, 6219-6224.

Matter, J.M., Stute, M., Snæbjörnsdottir, S.Ó., Oelkers, E.H., Gislason, S.R., Aradottir, E.S., Sigfusson, B., Gunnarsson, I., Sigurdardottir, H., Gunnlaugsson, E. and Axelsson, G. (2016) Rapid carbon mineralization for permanent disposal of anthropogenic carbon dioxide emissions. Science **352**, 1312-1314.

Neubeck, A., Duc, N.T., Hellevang, H., Oze, C., Bastviken, D., Bacsik, Z. and Holm, N.G. (2014) Olivine alteration and H_2 production in carbonate-rich, low temperature aqueous environments. Planet. Space Sci. **96**, 51–61.

McCollom, T.M. and Bach, W. (2009) Thermodynamic constraints on hydrogen generation during serpentinization of ultramafic rocks. Geochim. Cosmochim. Acta **73**, 856–875.

McCollom, T.M. and Seewald, J.S. (2001) A reassessment of the potential for reduction of dissolved CO_2 to hydrocarbons during serpentinization of olivine. Geochim. Cosmochim. Acta **65**, 3769–3778.

McDonough, W.F. and Sun, S. S. (1995) The composition of the Earth. Chem. Geol. **120**, 223–253.

McGrail, B.P., Schaef, H.T., Ho, A.M., Chien, Y.-J., Dooley, J.J. and Davidson, C.L., 2006. Potential for carbon dioxide sequestration in flood basalts. J. Geophys. Res. **111**.

Palandri, J. L. and Kharaka, Y. K. (2004) A Compilation of Rate Parameters of Water-mineral Interaction Kinetics for Application to Geochemical Modeling (No. Open-File-2004-1068). Geological Survey, Menlo Park CA.

Palmer, D.A. and Wesolowski, D.J. (1997) Potentiometric measurements of the first hydrolysis quotient of magnesium (II) to 250°C and 5 molal ionic strength (NaCl). J. Solution Chem. **26**, 217–232.

Parkhurst, D.L. and Appelo, C.A.J. (2013) Description of Input and Examples for PHREEQC version 3—A computer program for speciation, batch-reaction, one-dimensional transport, and inverse geochemical calculations. U.S. Geological Survey Techniques and Methods, book 6, 497 pp.

Pearce, C. R., Saldi, G. D., Schott, J. and Oelkers, E. H. (2012) Isotopic fractionation during congruent dissolution, precipitation and at equilibrium: evidence from Mg isotopes. Geochim. Cosmochim. Acta **92**, 170-183.

Pogge von Strandmann, P.A.E., Burton, K.W., James, R.H., van Calsteren, P., Gíslason, S.R. and Sigfússon, B. (2008) The influence of weathering processes on riverine magnesium isotopes in a basaltic terrain. Earth Planet. Sci. Lett. **276**, 187–197.

Pogge von Strandmann, P.A.E., Elliott, T., Marschall, H.R., Coath, C., Lai, Y.J., Jeffcoate, A.B. and Ionov, D.A. (2011) Variations of Li and Mg isotope ratios in bulk chondrites and mantle xenoliths. Geochim. Cosmochim. Acta **75**, 5247–5268.

Přikryl, J., Jha, D., Stefánsson, A. and Stipp, S. L. S. (2017) Mineral dissolution in porous media: An experimental and modeling study on kinetics, porosity and surface area evolution. Appl. Geochem. **87**, 57-70,

Rimstidt, J.D., Brantley, S.L. and Olsen, A.A. (2012) Systematic review of forsterite dissolution rate data. Geochim. Cosmochim. Acta **99**, 159-178.

Saldi, G.D., Schott, J., Pokrovsky, O.S., Gautier, Q. and Oelkers, E.H. (2012) An experimental study of magnesite precipitation rates at neutral to alkaline conditions and 100–200°C as a function of pH, aqueous solution composition and chemical affinity. Geochim. Cosmochim. Acta **83**, 93–109.

Seyfried, W.E., Foustoukos, D.I. and Fu, Q. (2007) Redox evolution and mass transfer during serpentinization: An experimental and theoretical study at 200°C, 500bar with implications for ultramafic-hosted hydrothermal systems at Mid-Ocean Ridges. Geochim. Cosmochim. Acta **71**, 3872–3886.

Stefánsson, A. (2001) Dissolution of primary minerals of basalt in natural waters: I. Calculation of mineral solubilities from 0 C to 350°C. Chem. Geol. **172**, 225–250.

Stefánsson, A. (2010) Low-temperature alteration of basalts–the effects of temperature, acids and extent of reaction on mineralization and water chemistry. Jökull **60**, 165–184.

Stefánsson, A. and Barnes, J. D. (2016) Chlorine isotope geochemistry of Icelandic thermal fluids: Implications for geothermal system behavior at divergent plate boundaries. Earth Planet. Sci. Lett. **449**, 69-78.

Stefánsson, A., Bénézeth, P. and Schott, J. (2013) Carbonic acid ionization and the stability of sodium bicarbonate and carbonate ion pairs to 200°C – A potentiometric and spectrophotometric study. Geochim. Cosmochim. Acta **120**, 600–611.

Stefánsson, A., Bénézeth, P., Schott, J. (2014) Potentiometric and spectrophotometric study of the stability of magnesium carbonate and bicarbonate ion pairs to 150°C and aqueous inorganic carbon speciation and magnesite solubility. Geochim. Cosmochim. Acta **138**, 21–31.

Stefánsson, A., Gunnarsson, I. and Giroud, N. (2007) New methods for the direct determination of dissolved inorganic, organic and total carbon in natural waters by

Reagent-Free™ Ion Chromatography and inductively coupled plasma atomic emission spectrometry. Anal. Chimica. Acta **582**, 69-74.

Stefánsson, A., Hilton, D.R., Sveinbjörnsdóttir, Á.E., Torssander, P., Heinemeier, J., Barnes, J.D., Ono, S., Halldórsson, S.A., Fiebig, J. and Arnórsson, S. (2017) Isotope systematics of Icelandic thermal fluids. J Volc. Geotherm. Res. **337**, 146-164.

Stefánsson, A., Sveinbjörnsdóttir, Á.E., Heinemeier, J., Arnórsson, S., Kjartansdóttir, R. and Kristmannsdóttir, H. (2016) Mantle CO_2 degassing through the Icelandic crust: Evidence from carbon isotopes in groundwater. Geochim. Cosmochim. Acta **191**, 300-319.

Teng, F.Z., Li, W.Y., Rudnick, R.L. and Gardner, L.R. (2010) Contrasting lithium and magnesium isotope fractionation during continental weathering. Earth Planet. Sc. Lett. **300**, 63-71.

Teng, F.Z., Wadhwa, M. and Helz, R.T. (2007) Investigation of magnesium isotope fractionation during basalt differentiation: implications for a chondritic composition of the terrestrial mantle. Earth Planet. Sc. Lett. **261**, 84-92.

Teng, F.Z., Li, W.Y., Ke, S., Yang, W., Liu, S.A., Sedaghatpour, F., Wang, S.J., Huang, K.J., Hu, Y., Ling, M.X. and Xiao, Y. (2015) Magnesium isotopic compositions of international geological reference materials. Geostand. Geoanal. Res. **39**, 329-339.

Teng, F. Z. (2017). Magnesium isotope geochemistry. Rev. Mineral. Geochem., **82**, 219-287.

Tester, J.W., Worley, W.G., Robinson, B.A., Grigsby, C.O. and Feerer, J.L. (1994) Correlating quartz dissolution kinetics in pure water from 25 to 625°C. Geochim. Cosmochim. Acta **58**, 2407–2420.

Voigt, M., Pearce, C. R. and Oelkers, H. E. (2016) Experimental study of the Mg and Sr isotopic evolution of seawater interacting with basalt between 150 and 300 °C. Geophysical Research Abstracts 18, EGU.

Wiechert, U. and Halliday, A.N. (2007) Non-chondritic magnesium and the origins of the inner terrestrial planets. Earth Planet. Sc. Lett. **256**, 360-371.

Wimpenny, J., Colla, C. A., Yin, Q. Z., Rustad, J. R. and Casey, W. H. (2014) Investigating the behaviour of Mg isotopes during the formation of clay minerals. Geochim. Cosmochim. Acta **128**, 178-194.

Associated content (Appendix 1)

Phase	Symbol	Reaction	log $K_{150°C}$	log $k_{i150°C}$ (mol/m^2/sec)	$r_{i\pm} = A_{geo}\, k\, (1\text{-}SI_i^m)$
Aqueous Species and surface reactions					
HCO_3^-		$CO_2 + H_2O = H^+ + HCO_3^-$	-6.74 [a]		
CO_3^{-2}		$HCO_3^- = H^+ + CO_3^{2-}$	-10.30 [a]		
$NaHCO_3$(aq)		$Na^+ + HCO_3^- = NaHCO_3$(aq)	0.42 [a]		
$NaCO_3^-$		$Na^+ + CO_3^{2-} = NaCO_3^-$	1.94 [a]		
$MgHCO_3^+$		$Mg^{2+} + HCO_3^- = MgHCO_3^+$	1.76 [b]		
$MgCO_3$(aq)		$Mg^{2+} + CO_3^{2-} = MgCO_3$(aq)	3.70 [b]		
$MgOH^+$		$Mg^{2+} + H_2O = MgOH^+ + H^+$	-8.06 [c]		
Mineral					
Olivine	fo_{93}	$Mg_{1.86}Fe_{0.14}SiO_4(s) + 4H^+ = 1.86Mg^{2+} + 0.14Fe^{2+} + H_4SiO_4$(aq)	16.89 [d]	-4.12-0.256pH [e]	$A_{geo}\, k$ (1-SI)
Magnesite	mgs	$MgCO_3(s) + H^+ = Mg^{2+} + HCO_3^-$	-0.33 [f]	-10 [g]	k (1-SI^2)
Siderite	sid	$FeCO_3(s) + H^+ = Fe^{2+} + HCO_3^-$	-2.53 [f]	-10 [g]	k (1-SI^2)
$Mg_{0.25}Fe_{0.75}CO_3$	carb-ss	$Mg_{0.25}Fe_{0.75}CO_3(s) + H^+ = 0.75Fe^{2+} + 0.25Mg^{2+} + HCO_3^-$	-2.22 [f]	-10 [g]	k (1-SI^2)
$Mg_{0.5}Fe_{0.5}CO_3$	carb-ss	$Mg_{0.5}Fe_{0.5}CO_3(s) + H^+ = 0.5Fe^{2+} + 0.5Mg^{2+} + HCO_3^-$	-1.73 [f]	-10 [g]	k (1-SI^2)
$Mg_{0.75}Fe_{0.25}CO_3$	carb-ss	$Mg_{0.75}Fe_{0.25}CO_3(s) + H^+ = 0.25Fe^{2+} + 0.75Mg^{2+} + HCO_3^-$	-1.12 [f]	-10 [g]	k (1-SI^2)
Chrysotile	ctl	$Mg_3Si_2O_5(OH)_4(s) + 6H^+ = 3Mg^{2+} + 2H_4SiO_4$(aq) + H_2O	20.11 [h]	-8.20(k_n), -9.78(k_b) [i]	$(k_n + k_b\, a_{H^+}^{-0.23})$(1-SI)
Talc	tlc	$Mg_3Si_4O_{10}(OH)_2(s) + 4H_2O + 6H^+ = 3Mg^{2+} + 4H_4SiO_4$(aq)	13.42 [h]	-9.83 [i]	k(1-SI)
Brucite	bru	$Mg(OH)_2(s) = Mg^{2+} + 2OH^-$	-12.35 [j]	-1.68(k_a), -6.07(k_n) [i]	$(k_a\, a_{H^+}^{0.5} + k_n)$(1-SI)
Amorphous silica	am-Si	$SiO_2(s) + 2H_2O = H_4SiO_4$(aq)	-1.98 [f]	-9.43 [k]	k(1-SI)

[a] Stefánsson et al. (2013)
[b] Stefánsson et al. (2014)
[c] Palmer and Wesolowski (1997)
[d] Stefánsson (2001)
[e] Rimsdit et al. (2012)
[f] Gysi and Stefánsson (2011)
[g] Saldi et al. (2012)
[h] Gunnarsson et al. (2005)
[i] Palandri and Kharaka (2004)
[j] Holland and Powell (2011)
[k] Carroll et al. (1998)

Appendix 1. *Thermodynamic and kinetic database used for the kinetic reaction path simulations*.

Appendix V

Appendix V

CO_2 mineralization by olivine at hydrothermal conditions

Jan Přikryl, Andri Stefánsson

Institute of Earth Sciences, University of Iceland, Sturlugata 7, 101 Reykjavik, Iceland

Mineralogical Magazine, 2014

Keywords: CO_2; olivine; reaction modelling; water-rock interaction

Mineralogical Magazine, November 2014, Vol. 78(6), pp. 1473–1477

OPEN ACCESS

CO_2 mineralization by olivine at hydrothermal conditions

JAN PŘIKRYL* AND ANDRI STEFÁNSSON

Institute of Earth Sciences, University of Iceland, Sturlugata 7, 101 Reykjavík, Iceland

[*Received 1 May 2014; Accepted 8 December 2014; Associate Editor: T. Rinder*]

ABSTRACT

The interaction of CO_2-rich water with olivine was studied using geochemical reaction modelling in order to gain insight into the effects of temperature, acid supply (CO_2) and extent of reaction on the secondary mineralogy, water chemistry and mass transfer. Olivine (Fo93) was dissolved at 150 and 250ºC and pCO_2 of 2 and 20 bar in a closed system and an open system with secondary minerals allowed to precipitate. The progressive water–rock interaction resulted in increased solution pH, with gradual carbonate formation starting at pH 5 and various Mg-OH and Mg-Si minerals becoming dominant at pH>8. The major factor determining olivine alteration is the pH of the water. In turn, the pH value is determined by acid supply, reaction progress and temperature.

KEYWORDS: CO_2, olivine, reaction modelling, water–rock interaction.

Introduction

CARBONATE mineral scaling is commonly associated with geothermal fluid utilization, both in the reservoir as well as in production and re-injection wells and surface pipelines (Gunnlaugsson 2012; Gunnlaugsson *et al*., 2014). Understanding the CO_2–water–rock interaction at geothermal conditions is therefore important in terms of geothermal utilization. Olivine is a major constituent of mafic rocks and commonly associated with geothermal systems. Moreover, it contains a limited number of main elements (Mg, Fe^{2+}, Si and O) and may serve as a suitable system to demonstrate and test geochemical reaction modelling with observations from experiments.

A number of studies have focused on CO_2–water–rock interaction by geochemical modelling and laboratory experiments. Under geothermal conditions these include, for example, forsterite dissolution and magnesite formation (Giammar *et al*., 2005) and CO_2–water–basalt interaction (Gysi and Stefánsson, 2011, 2012*a*,*b*,*c*; Galeczka *et al*., 2014). Most of these studies have implemented relatively simple models though some recent work has tried to include a fully kinetic approach (Hellevang *et al*., 2013).

The aim of the present study was to examine the interaction of CO_2-rich water with olivine under hydrothermal conditions using geochemical reaction modelling, in particular, to investigate the effects of acid supply, reaction progress (ξ) on the overall reaction path and the rate of mass transfer.

Model calculations

Reaction-path simulations were carried out at 150–250ºC in order to study the effects of temperature, CO_2 supply, extent of reaction, and time on the CO_2–water–olivine alteration process (geochemical system with CO_2-H_2O-MgO-FeO-SiO_2 chemical components). The calculations were carried out using the *PHREEQC* geochemical program, version 2.18,

* E-mail: jap5@hi.is
DOI: 10.1180/minmag.2014.078.6.14

This paper is published as part of a special issue in *Mineralogical Magazine*, Vol. **78(6)**, 2014 entitled 'Mineral–fluid interactions: scaling, surface reactivity and natural systems'.

(Parkhurst and Appelo, 1999) and the Wateq database with updates listed below. The reaction-path calculations were carried out on the interaction between forsterite (Fo93) and solutions of variable CO_2 concentration. The initial solution contained 10 to 200 mmol kg^{-1} of dissolved CO_2 (pCO_2 = ~2 and ~20 bar), the solutions were titrated stepwise with 1.378 mol of olivine (200 mg olivine) and the reaction progress was followed. Two types of calculations were used: closed (limited CO_2) and open (unlimited CO_2) systems. In the present study, the moles of progressively dissolved olivine per kilogram of solution were taken to represent the reaction progress (ξ) of the system. In the calculation, secondary mineral precipitation reactions were assumed to be controlled by instantaneous equilibration upon saturation in solution. The secondary minerals considered include goethite (FeOOH), talc ($Mg_3Si_4O_{10}(OH)_2$), chrysotile ($Mg_3Si_2O_5(OH)_4$), antigorite ($Mg_{48}Si_{34}O_{85}(OH)_{62}$), chlorite-Al free ($Mg_6Si_4O_{10}(OH)_8$), anthophyllite ($Mg_7Si_8O_{22}(OH)_2$), brucite ($Mg(OH)_2$), magnesite ($MgCO_3$), siderite ($FeCO_3$) and Fe-Mg carbonates ($Mg_{0.25}Fe_{0.75}CO_3$, $Mg_{0.5}Fe_{0.5}CO_3$, $Mg_{0.75}Fe_{0.25}CO_3$). These mineral solubilities and the appropriate CO_2-aqueous speciation dataset were updated in the present work using recent literature data (Palmer and Wesolowski, 1997; Holland and Powell, 2011; Gysi and Stefánsson, 2011; Stefánsson *et al*., 2013; 2014). The mass exchanges in the system were assumed to be controlled by the rate of olivine dissolution, the rate expression taken from Rimstidt *et al*. (2012).

CO_2–olivine interaction

Initially the solution pH was between 3.8 and 4.2 at 150ºC, depending on pCO_2. Upon progressive CO_2–water–rock interaction, the pH increased due to consumption of H^+ upon olivine dissolution. At first, the pH was buffered at ~6 by the ionization of carbonic acid and formation of talc, carbonates and either chlorite or chrysotile. Such mildly acid to neutral conditions are characterized either by high initial acid supply and low to moderate extent of the reaction or a low acid supply and low extent of reaction. When most of the CO_2 has been mineralized, the pH rises rapidly to >8 and is buffered by the coexistence of brucite, carbonates and either chlorite or

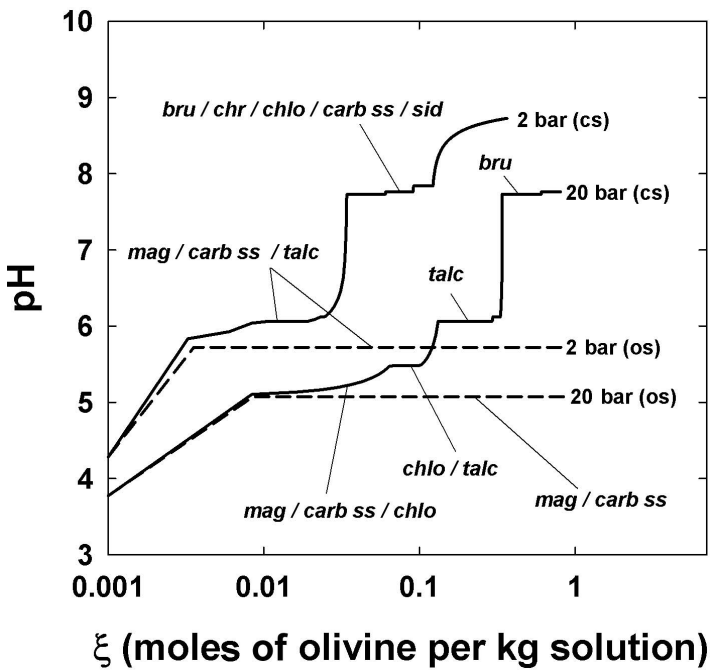

FIG. 1. Changes in pH upon reaction progress (ξ) at pCO_2 = 2–20 bar for open (os) and closed systems (cs) at 150ºC. Indication of the minerals when pH is buffered is included on the diagram also. Mineral abbreviations: bru – brucite, carb – carbonates, chlo – chlorite, chr – chrysotile, mag – magnesite, sid – siderite.

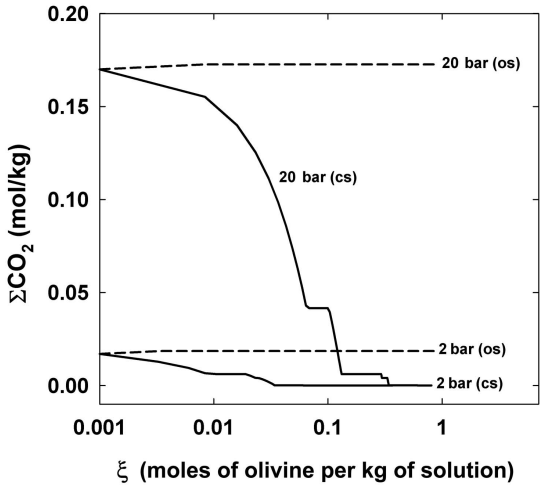

FIG. 2. The concentration of ΣCO_2 (sum of CO_2 aqueous speciation) in solution as a function of reaction progress (ξ) at 150ºC for open (os) and closed (cs) systems.

chrysotile (Figs 1, 2 and 3). This results in decreased mobility and concentrations of Mg and Si in solution. Consequently, the carbonates were found to become increasingly more Fe rich upon reaction progress and increased pH (Fig. 3). Insignificant amounts of olivine are needed at low initial CO_2 concentration to increase the pH to alkaline conditions. With increasing initial CO_2 concentration, more olivine dissolution is needed to increase the pH of the water.

For open systems with unlimited CO_2 supply the pH is buffered at 5−5.7, depending on pCO_2 (Fig. 1), upon dissolution of a limited amount of olivine and consequent precipitation of talc and a solid solution of Mg-Fe carbonates (Figs 1, 3). With increasing reaction progress, pH remains fixed at such comparatively low values by mineral-solution equilibria due to the continuous supply of CO_2 which triggers further dissolution of olivine accompanied by precipitation of talc

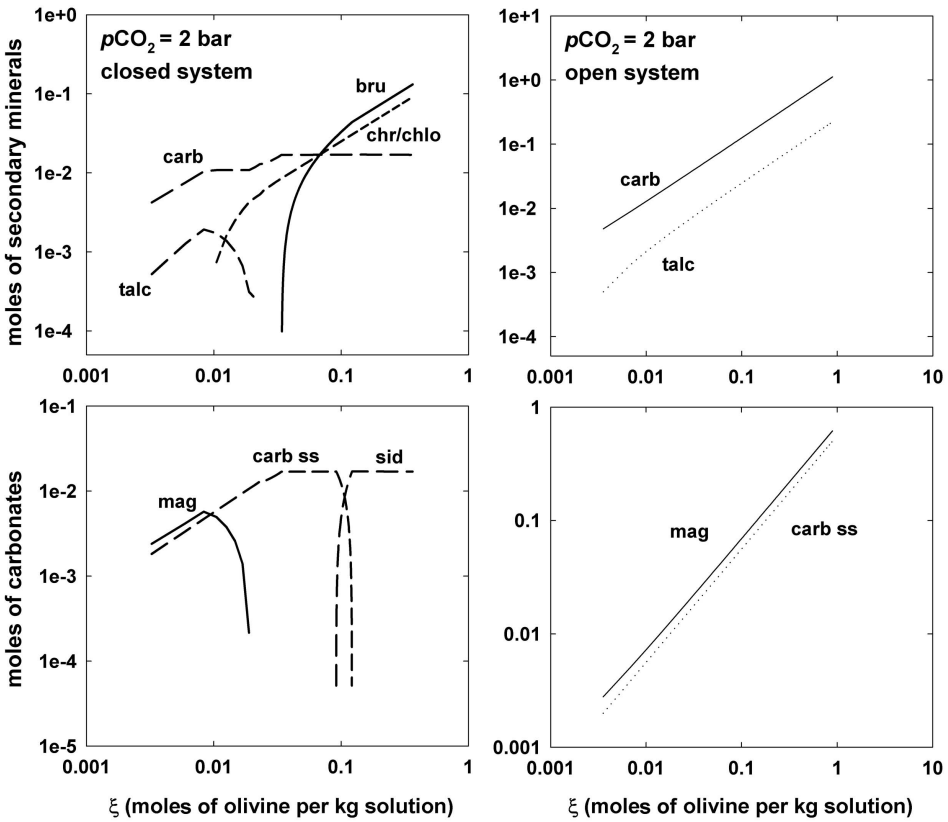

FIG. 3. The moles of secondary minerals formed as a function of reaction progress at pCO_2 = 2 bar and for open (os) and closed (cs) systems at 150ºC. Mineral abbreviations: bru − brucite, carb − carbonates, carb ss − carbonate solid solutions, mag − magnesite, sid − siderite.

and carbonates as indicated schematically by the reaction:

$$Mg_{1.86}Fe_{0.14}SiO_4+1.26CO_2+0.25H_2O = 0.25Mg_3Si_4O_{10}(OH)_2+1.26\ Mg_{0.88}Fe_{0.11}CO_3$$

In other words, a steady state is attained, with constant composition of both the aqueous solution and the carbonate solid solution as well as a constant ratio between the masses of precipitating secondary minerals.

Based on this, one can conclude that the very fine variations in pH at a particular temperature constitute the dominant parameter in determining secondary-mineral composition. In turn, pH is controlled by acid supply, partial pressure and extent of reaction.

The rate of olivine dissolution and overall mass transfer is also related to the pH of the solution as well as the temperature (Figs 1, 4). The dissolution rate of olivine decreases with increasing pH. It follows that progressive CO_2–water–olivine interaction result in decreased olivine dissolution rate and the overall mass transfer within the system. On the other hand, increased temperature increases the dissolution rate and the overall mass movement of the system. However, temperature does not have a significant influence on the overall reaction path with carbonates predominant at pH<7 and Mg-Si and Mg-OH minerals at pH>8.

The variety of conditions presented and their effect on olivine alteration represent theoretical scenarios, reaction paths, for natural fluid–rock interactions at geothermal conditions.

Conclusions

The interaction of CO_2-rich water with olivine under hydrothermal conditions (150 and 250ºC) was studied using geochemical modelling. In particular, the effects of acid supply and reaction progress on the overall reaction path as well as rate of mass exchanges within the system under consideration were investigated. The progressive water–rock interaction resulted in increased solution pH, with carbonate formation starting at pH 5 and various Mg-OH and Mg-Si minerals becoming predominant under alkaline conditions. As a result, the carbonates were Mg-rich at mildly acid conditions but became increasingly Fe-rich with increasing pH. The major factor determining olivine alteration is the pH of the water. In turn, the pH value is determined by acid supply, reaction progress and temperature.

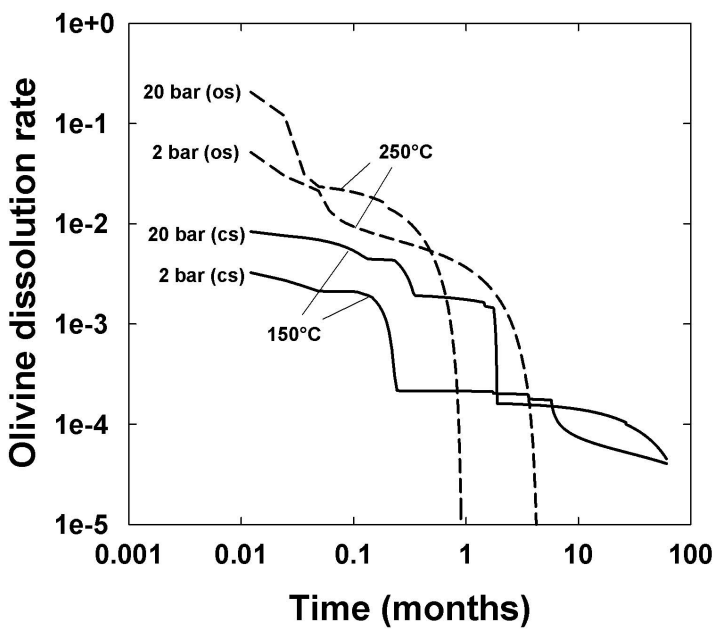

FIG. 4. The dissolution rate of olivine (Rimstidt *et al*., 2012) as a function of reaction progress in time at 150ºC and 250ºC and pCO_2 = 2 and 20 bar for open (os) and closed systems (cs). As observed, mass movement is influenced by pH as well as temperature. In turn, the pH is affected by the reaction progress and initial CO_2 concentration.

Acknowledgements

The authors thank H. Hellevang, L. Marini, S. Jelavic and guest editor T. Rinder for comments and suggestions that improved the quality of the manuscript. This research was made possible by a Marie Curie grant from the European Commission in the framework of the MINSC ITN (Initial Training Research network), Project number 290040 and by the Science Institute, University of Iceland.

References

Galeczka, I., Wolff-Boenisch, D., Oelkers, E.H. and Gíslason, S.R. (2014) An experimental study of basaltic glass−H_2O−CO_2 interaction at 22−50ºC: Implications for subsurface storage of CO_2. *Geochimica et Cosmochimica Acta*, **126**, 123−145.

Giammar, D.E., Bruant, R.G., Jr and Peters, C.A. (2005) Forsterite dissolution magnesite precipitation at conditions relevant for deep saline aquifer storage sequestration of carbon dioxide. *Chemical Geology*, **217**, 257−276.

Gunnlaugsson, E. (2012) *Scaling in geothermal installation in Iceland*. Short Course on Geothermal Development and Geothermal Wells, organized by UNU-GTP and LaGeo, in Santa Tecla, El Salvador, 6 pp.

Gunnlaugsson, E., Ármannsson, H., Thorhallsson, S. and Steingrímsson, B. (2014) *Problems in geothermal operation − scaling and corrosion*. Short Course VI on Utilization of Low- and Medium-Enthalpy Geothermal Resources and Financial Aspects of Utilization, organized by UNU-GTP and LaGeo, in Santa Tecla, El Salvador, 18 pp.

Gysi, A.P. and Stefánsson, A. (2011) CO_2−water–basalt interaction. Numerical simulation of low temperature CO_2 sequestration into basalts. *Geochimica et Cosmochimica Acta*, **75**, 4728−4751.

Gysi, A.P. and Stefánsson, A. (2012*a*) Mineralogical aspects of CO_2 sequestration during hydrothermal basalt alteration − An experimental study at 75 to 250ºC elevated pCO_2. *Chemical Geology*, **306**, 146−159.

Gysi, A.P. and Stefánsson, A. (2012*b*) Experiments and geochemical modeling of CO_2 sequestration during hydrothermal basalt alteration. *Chemical Geology*, **306 (307)**, 10−28.

Gysi, A.P. and Stefánsson, A. (2012c) CO_2–water–basalt interaction. Low temperature experiments and implications for CO_2 sequestration into basalts. *Geochimica et Cosmochimica Acta*, **81**, 129−152.

Hellevang, H., Pham, V.T. and Aagaard, P. (2013) Kinetic modelling of CO_2−water−rock interactions. *International Journal of Greenhouse Gas Control*, **15**, 3−15.

Holland, T.J.B. and Powell, R. (2011) An improved extended internally consistent thermodynamic dataset for phases of petrological interest, involving a new equation of state for solids. *Journal of Metamorphic Geology*, **29**, 333−383.

Palmer, D.A. and Wesolowski, D.J. (1997) Potentiometric measurements of the first hydrolysis quotient of magnesium (II) to 250ºC and 5 molal ionic strength (NaCl). *Journal of Solution Chemistry*, **26**, 217−232.

Parkhurst, D.L. and Appelo, C.A.J. (1999) User's guide to PHREEQC (Version 2) − A computer program for speciation, batch-reaction, one-dimensional transport inverse geochemical calculations. US Geological Survey Water Resources Investigations Report 99-4259. U.S. Geological Survey, Denver, Colorado, USA, 312 pp.

Rimstidt, J.D., Brantley, S.L. and Olsen, A.A. (2012) Systematic review of forsterite dissolution rate data. *Geochimica et Cosmochimica Acta*, **99**, 159−178.

Stefánsson, A., Bénézeth, P. and Schott, J. (2013) Carbonic acid ionization the stability of sodium bicarbonate carbonate ion pairs to 200ºC − A potentiometric spectrophotometric study. *Geochimica et Cosmochimica Acta*, **120**, 600−611.

Stefánsson, A., Bénézeth, P. and Schott, J. (2014) Potentiometric spectrophotometric study of the stability of magnesium carbonate bicarbonate ion pairs to 150ºC aqueous inorganic carbon speciation magnesite solubility. *Geochimica et Cosmochimica Acta*, **138**, 21−31.